Magnetotransport in Low Dimensional Semiconductor Structures

Gil-Ho Kim

Clare College
University of Cambridge

Dissertation submitted for the degree of
Doctor of Philosophy

Except where stated otherwise, this thesis contains my own original work which was not done in collaboration with others.

This thesis is not substantially the same as any that I have already submitted, or am in the process of submitting, for any degree at this or another University. It is less than 60,000 words long.

G. H. Kim 17/03/1998

To my mother, wife Mi-Ok, and children Han-Ul and Hyo-Eun.

Acknowledgments

This dissertation is the result of research performed in the Semiconductor Physics group at the Cavendish Laboratory, between October 1993 and September 1997. I am grateful to the Semiconductor Physics group for providing excellent research facilities: low temperature measuring equipment, MBE machines, clean room, computers, and support.

Firstly, I would like to thank my supervisor, Dave Ritchie, for suggesting this research project and for his support and encouragement. I am also grateful to James Nicholls for his help throughout the project and for many useful discussions. I must also thank Mike Pepper for building a research group with the excellent facilities available.

I would like to thank Alex Churchill, who gave me initial lessons on experimental techniques, and Michelle Simmons and Dave Ritchie for supplying the material used throughout this thesis. Thanks must also go to Chris Ford for the writing of both *CryoMeas* and *LabAssistant* and for maintaining the Archimedes system and network manager that he has developed, all of which have greatly simplified the collection/analysis of experimental data. The Unix system, run by Angus North, has also proved invaluable.

Although the work presented here is my own original work, it could not have been undertaken without the technical assistance and advice of others. I have learned much in various disciplines from Chi-Te Liang, Crispin Barnes, Alex Hamilton, Shye Shapira, Nick Appleyard, and Mark Field. I am greatly appreciative to Guada Lian, Stuart Brown, and Jun Yuan for

the TEM, STM, STEM, and AFM images included in this dissertation. Numerous discussions with Atush Kurobe, Ben Simons, Sergey Kravchenko, Frank Stern, and Eugene Kogan have been exceedingly useful. Thanks must also go to Harry Clark for teaching fabrication techniques, Alan Beckett for helping run the fridge systems, and Pete Flaxman for providing a regular helium supply. I very much acknowledge the critical proof-reading of the thesis by Ian Millard, Chi-Te Liang, Julian Shilton, and James Nicholls. Thanks to Chi-Te, Thomas, Julian, Harvey, Angus, Ruth, Marcus, Patrick, Kai, Saiful, Ian, Ahrash, Nick, and Martin for their friendliness, and Tina Jost for being ever so cheerful and helpful.

The financial assistance for this work was partially provided by Clare College (the Arkinson fund and the Skillman fund) and the Semiconductor Physics group. I am appreciative to Elizabeth Freeman, my College tutor, who has assisted greatly in helping me to obtain financial support.

Summary

This dissertation describes low-temperature electronic transport measurements on semiconductor structures of restricted dimensionality. The experiments fall into two sets. The first concerns anisotropic magnetotransport measurements and electron focusing in a varying external magnetic field. These are performed using MBE-grown high mobility two-dimensional electron gases formed on (311)B GaAs substrates. The second is a study of magnetic field induced insulator-quantum Hall liquid transitions performed on GaAs-AlGaAs heterostructures in which a number of InAs monolayers are inserted in the centre of a GaAs quantum well. The sample structures were characterised by STM, TEM, STEM, and AFM.

Interest in electron transport on high-index GaAs surfaces is increasing, especially since the advent of patterned substrate regrowth. An anisotropic mobility in orthogonal directions seems to be universal for electron gases grown on (311)B-oriented GaAs substrates. The anisotropy depends on the two-dimensional electron gas carrier density, but mobilities are always higher in the $[\bar{2}33]$ direction. The interface roughness scattering is a possible cause of the mobility anisotropy. The electron focusing results demonstrate that the effective mass and Fermi surface are isotropic even through the mobility is anisotropic. An explanation is propose based on interface roughness scattering.

In the second part, a magnetically induced direct transition from an insulating state at zero magnetic field to quantum Hall effect states with Hall resistance $\rho_{xy} = h/2e^2$ and $\rho_{xy} = h/e^2$ and back to an insulating state at higher field is observed. The phase boundaries are plotted as a function of disorder and magnetic field using two methods, firstly the temperature independent ρ_{xx} points and secondly the maxima in σ_{xx}. This experimental phase diagram is related to the disorder induced collapse of spin splitting in the lowest Landau level obtained from activation energy studies.

Contents

Chapter 1

Gated Two-Dimensional Electron Gas

1.1 Introduction

In this chapter the formation of a two-dimensional electron gas (2DEG) in a GaAs-AlGaAs heterostructure is introduced. The increased confinement has interesting and important effects upon the electrical transport properties of these layers. The technique of modulation doping is described and the use of a Schottky gate to control the 2DEG carrier density is discussed.

1.2 Modulation doped heterostructures

A heterojuction is formed at the boundary between two different semiconductor materials. Due to the difference in their band gaps, to reach electrostatic equilibrium the conduction and valence bands are distorted and a layer of electrons may form at the heterojunction interface. This accumulation layer is very thin, ($\sim$ 100 Å), such that the electron's motion in the direction perpendicular to the interface is quantized. A similar degree of confinement may also be provided by a quantum well formed from a layer ($\sim$ 100 Å) of

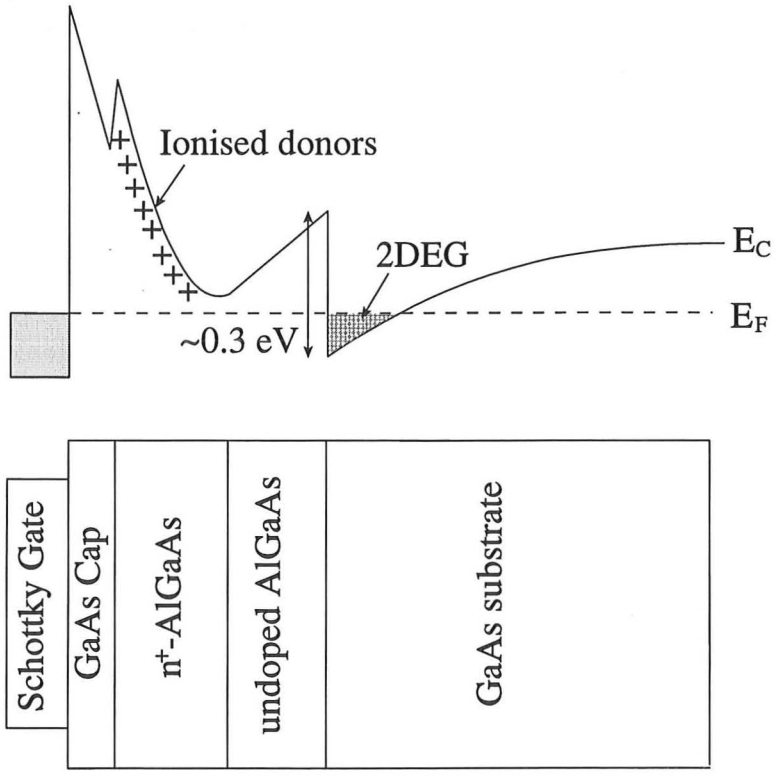

Figure 1.1: The conduction band structure of a GaAs-AlGaAs heterostructure, showing the formation of a triangular potential well at the interface.

GaAs sandwiched between two AlGaAs layers. As the electrons may only move freely in the plane the accumulation layer is therefore called a *two-dimensional electron gas.* A commonly used heterostructure employed to investigate two-dimensional transport is composed of the two semiconductors GaAs and $Al_xGa_{1-x}As$. The lattice constant for the unit cell of GaAs is 5.6533 Å and that of the compound AlAs (x = 1) is 5.6605 Å[1]. Therefore, the lattice mismatch between GaAs and AlAs is only 0.14%, and even less (0.04%) between GaAs and the typical $Al_xGa_{1-x}As$ compound used with a mole fraction x of 0.3.

In order to induce free electrons in the conduction band minimum the sample is doped with shallow donor impurities, with the impurities placed in the $Al_xGa_{1-x}As$ electrons fall over the potential barrier into the GaAs,

leaving behind positively charged impurity centres. This 'space charge' gives rise to an electric field, which bends the band edges of the two materials, in a similar way to the p-n junction in a semiconductor diode. The result of this is an internal electric field across the surface of the GaAs and the creation of a triangular potential well at the interface, as shown in figure 1.1. Through the technique of modulation doping [2, 3] extremely high 2DEG mobilities can be obtained. This method involves the addition of an undoped AlGaAs 'spacer' layer between the doped AlGaAs and the GaAs interface. As the 2DEG electrons in such structures are separated by (typically) several hundred Angstroms from the dopants impurity scattering is reduced. Thus the carrier mobility is limited by ionised impurity scattering at low temperatures. Whilst silicon is often used to dope $Al_xGa_{1-x}As$ as n-type material, beryllium can also be used to dope this semiconductor as p-type. In this thesis all the devices used are based on the modulation doped GaAs-AlGaAs heterostructures.

The heterostructures are grown by molecular beam epitaxy (MBE) in ultra high vacuum (UHV) conditions, with background pressures of order $\sim 1 \times 10^{-11}$ mbar. This is necessary in order to reduce contamination by unwanted impurities. Using MBE it is possible to control the semiconducting material deposited monolayer by monolayer enabling precise growth of the required structure. The quality of the crystal grown is very sensitive to the substrate temperature and the best temperatures for the growth of InAs, AlAs, and GaAs are 530°C, 580°C, and 630°C respectively. The devices for this work were grown by the Semiconductor Physics group at the Cavendish Laboratory.

1.3 Schottky barrier gate

The standard method for gating GaAs-AlGaAs heterostructures entails covering the surface with an evaporated metal. The metal-GaAs interface acts

as a Schottky barrier which isolates the charges on the gate from charges in the 2DEG. Therefore the Schottky gate can be used to control the carrier density in the 2DEG. By applying a negative bias to the metal gate the height of the gate barrier is increased and the potential well at the GaAs-AlGaAs interface is reduced in energy. Eventually, the bound state in the potential minima is raised above the Fermi energy, depleting the well of free carriers. Conversely, by applying a positive bias to the gate, one may capacitively induce carriers into the 2DEG.

The carrier density in a GaAs-AlGaAs heterostructure, at low temperature, can also be enhanced by shining an red light emitting diode (LED) onto the device. This has the effect of exciting electrons out of trapping (DX) donor states [4] in the $Al_xGa_{1-x}As$, into the 2DEG. After illumination, below temperatures of $\sim$ 100 K, electrons in the 2DEG are unable to return to the DX centres. This effect is called persistent photoconductivity (PPC) effect [5].

1.4 Conclusions

In this chapter a brief introduction into the GaAs-AlGaAs heterojunction system has been given. The concepts of modulation doping and control of the 2DEG carrier density by a Schottky gate have been described.

Bibliography

[1] S. M. Sze, *Semiconductor Device Physics and Technology* (John Wiley & Sons, New York) (1985).

[2] H. L. Stormer, R. Dingle, A. C. Gossard, W. Weigmann, and M. D. Sturge, Solid State Commun. **29**, 705 (1979).

[3] H. L. Stormer, Surf. Sci. **132**, 519 (1983).

[4] D. V. Lang and R. A. Logan, *Physics of Semiconductors* (Inst. Phys. Conf. Ser. 43) 433 (1979)

[5] M. Nathan, Solid-State Electron. **29**, 167 (1986).

Chapter 2

Conduction Theory

2.1 Introduction

In this chapter we present a brief theoretical survey of electron transport in a low-dimensional system at low temperatures. In section 2.2 the Drude model and Einstein relation for electron transport is introduced. Section 2.3 discusses length scales associated with different aspects of electron motion. Section 2.4 describes the metallic conductivity with weak localisation and electron-electron interactions whilst section 2.5 discusses transport in the strongly localised regime. Finally, section 2.6 describes the fundamental properties of a 2DEG subject to a magnetic field: density of states, Shubnikov-de Haas oscillations, integer quantum Hall effect, and spin splitting.

2.2 Drude theory and Einstein relation

In the classical analysis of electron transport in the presence of an electric field E, electrons accelerate in the direction of the field and together with a random thermal velocity, they have a total average velocity v_d. This drift velocity is related to E by $v_d = Ee\tau/m^*$, where τ is the mean time interval

between momentum-relaxing collisions, and m^* is the electron effective mass ($m^* = 0.067m_e$ in GaAs) which may be considerably smaller than the free electron mass m_e. The current density j is then given by

$$j = n_s e v_d = \frac{n_s e^2 \tau E}{m^*}, \tag{2.1}$$

where n_s is the carrier density, and e is the charge on an electron. Thus this earliest, and simplest model of the Drude conductivity σ_D in the absence of a magnetic field is given by

$$\sigma_D = \frac{j}{E} = \frac{n_s e^2 \tau}{m^*} = \frac{e^2}{h} k_F l, \tag{2.2}$$

where k_F is the Fermi wave vector and l is the mean free path. Equation 2.2 applies to materials whose electron distribution obeys Fermi-Dirac statistics. At zero temperature, electron states are filled up to the Fermi energy E_F. All electrons acquire the same equal drift velocity induced by the applied electric field and the Fermi surface shifts in k-space in the direction of the field. For the free-electron model, the average distance travelled between successive collisions is $l = v_F \tau$, where v_F is proportional to the Fermi wavevector k_F. Experimental studies estimate l to be approximately 1 μm for typical 2DEG in GaAs-AlGaAs heterostructures. The mobility μ is a measure of the quality of a 2DEG and since $v_d = \mu E$ is defined in an electric field, it is given by;

$$\mu = \frac{e\tau}{m^*} = \frac{\sigma_D}{n_s e}. \tag{2.3}$$

Where σ can be obtained by inverting the measured resistivity. Hence it is possible to determine the mobility in the absence of a magnetic field.

In the derivation of the Drude conductivity, equation 2.2, we assumed a homogeneous conducting semiconductor in which the carrier density is uniform throughout. A nonuniform distribution of carriers gives rise to diffusion. With any carrier density gradient there is a net flow of carriers,

which acts to restore equilibrium. Therefore, in an inhomogenous semiconductor, the diffusion current must exactly balance the drift current and the conductivity is determined by the Einsten relation:

$$\sigma = e^2 \rho(E_F) D, \tag{2.4}$$

where $\rho(E_F) = m^*/2\pi\hbar^2$ is the density of occupied electron states per unit volume and the diffusion constant $D = v_F l/2$ for a two-dimensional system. The Einstein conductivity can also be applied to a 2DEG in a magnetic field in which the Fermi-energy oscillates through localised states.

2.3 Length scales

The length scales of the transport and scattering mechanisms determine the nature of the transport for the physical properties of low dimensional structures. In this section some of these lengths are introduced. The first important length scale, contained within the Drude theory, is the mean free path of elastic collisions $l = v_F \tau$. We can consider a sample of length L and width W with different elastic mean free path lengths l [1]:

(i) Diffusion regime L, W > l: Conduction is diffusive with impurity scattering dominant.

(ii) Quasi-ballistic regime L > l > W: In this regime, boundary scattering and impurity scattering are of equal importance.

(iii) Ballistic regime L, W < l: The dimensions of the sample are less than the mean free path and electrons move through the channel without scattering.

At finite temperatures, inelastic scattering processes (phonon scattering or electron-electron scattering) destroy phase-memory. We may define this period through the phase coherence length, which is the mean distance an electron diffuses before the phase is lost,

$$l_\phi = \sqrt{D\tau_\phi}, \tag{2.5}$$

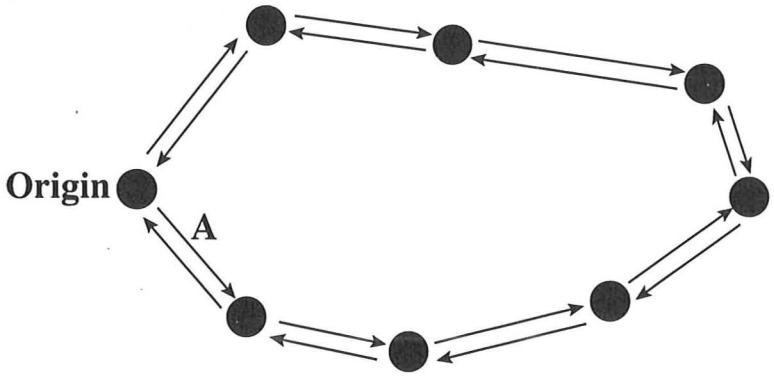

Figure 2.1: A schematic diagram showing the clockwise and counterclockwise trajectories of an electron undergoing a series of elastic scattering events.

where τ_ϕ is the phase relaxation time. If the sample length L is smaller than the phase coherence length l_ϕ, the electron interference pattern can be observed as universal conductance fluctuations.

Upon applying a perpendicular magnetic field the electron undergoes classical cyclotron orbits of radius l_c, the cyclotron length:

$$l_c = \frac{v_F}{\omega_c} = \frac{\hbar}{eB}\sqrt{2\pi n}, \tag{2.6}$$

where $\omega_c = eB/m^*$ is the cyclotron frequency. This length is particularly important in quasi-ballistic, narrow channels.

Finally, in a magnetic field the spatial extent of an electron's wavefunction is given as

$$l_B = \sqrt{\frac{\hbar}{eB}}, \tag{2.7}$$

where l_B is called the magnetic length.

2.4 Metallic conduction

2.4.1 Weak localisation

Let us consider a two dimensional system with randomly distributed scattering centres with an average separation of the mean free path l. In accordance with classical theory, the electron motion will be diffusive. The probability that an electron at point $r = 0$ and time $t = 0$ will be at point r' and at time t' is $P(r', t') \sim e^{r'/\sqrt{Dt'}}/\sqrt{Dt'}$. Using the Einstein relation, the diffusivity can be related to the conductivity by equation 2.4, however this a purely classical result and any sense of the wave nature of the electron is ignored. One can introduce a quantum interference correction to the classical Drude conductivity to account for long range quantum mechanical correlations. The quantum interference effect is the probability for back scattering in a disordered system only such that the electron retains its phase information after many elastic scattering events. This is seen at low temperatures and is called weak localisation.

Consider the clockwise and counterclockwise scattering paths in figure 2.1 each with their associated wavefunctions $\Psi_1 = Ae^{i\phi_1}$ and $\Psi_2 = Ae^{i\phi_2}$, respectively. The probability of electrons returning to the origin is

$$P(0) = \mid \Psi_1(0) + \Psi_2(0) \mid^2 = 2A^2 + 2A^2 cos(\phi_1 - \phi_2). \tag{2.8}$$

If the phases between the two paths are random, the second interference term on the right hand side will average to zero leaving the classical probability, $2A^2$. If the two paths have the same phase, $(\phi_1 = \phi_2)$, then $P(0) = 4A^2$ this is twice the classical probability of returning to the origin. In the limit where there are no mechanisms for phase-breaking, all of the electrons will be localised in standing waves corresponding to these time-reversed paths and the conductivity will be zero. Therefore the weak localisation contribution to the conductivity will depend on the average number of time-reversed paths in a phase-coherent area.

The application of a perpendicular magnetic field breaks time-reversal symmetry and the clockwise and counterclockwise time reversed paths no longer accumulate the same phase. For example, consider the Aharonov-Bohm experiment in which electron partial waves traverse the arms of a loop in either a clockwise or counterclockwise sense. If the electron retains its phase information the two waves will interfere at the point at which the two paths reconnect. Applying a magnetic flux through the loop induces a phase shift of $\Delta\phi = (e/h) \oint \mathbf{A} \cdot d\mathbf{l}$ between the two possible paths, where $\mathbf{A}$ is the vector potential such that $\mathbf{B} = \nabla \times \mathbf{A}$ and $d\mathbf{l}$ is an infinitesimal element of the path length. The weak localisation contribution to the conductivity will be the sum over all paths of these oscillations. At large enough fields, the oscillations will have a random phase and thus add incoherently while, at small field, all except the longest paths will add coherently. Weak localisation leads to positive magnetoconductance, i.e. the application of magnetic field increases the conductivity.

A further correction to the conductivity is caused by spin-orbit scattering. In this effect, a positive magnetoresistance occurs at very low magnetic fields as the electron spin rotates in the opposite direction along the closed loop, therefore the nominal constructive interference can be changed to destructive. This is known as 'antilocalisation'. The spin-orbit scattering time is believed to be independent of temperature.

2.4.2 Electron-electron interactions

The weak localisation correction to the conductivity is due to a single-electron quantum interference effect, and is therefore applicable for non-interacting particles. The Coulomb interactions between conduction electrons result in an additional quantum correction through electron-electron interactions.

The electron-electron interaction and weak localisation effects are diffi-

cult to separate experimentally as they both have a logarithmic temperature dependence. However, one may use a perpendicular magnetic field as their magnetic field dependences are different [2, 3].

2.5 Transport in insulators

Mott [4, 5] proposed that a crystalline array of monovalent atoms at temperature $T = 0$ K should show a sharp transition from insulator to metal, if the interatomic distance b decreases to a certain critical value (effective Bohr radius a_B^*). If b is sufficiently large (electron concentration is low), such that the electronic wavefunctions have negligible overlap the material should be an insulator with each wavefunction strongly localised around single ions. However, if b is small (electron concentration is large), the material should be a metal with overlapping electronic wavefunctions. The transition between the two regimes is known as the Mott transition. Another proposal for metal-insulator transition, by Anderson [6] presented the idea that the single-electron wave functions become localised due to disorder. Therefore, the system will become insulating at $T = 0$ K as the disorder is increased. A comprehensive survey of work upon the nature of the metal-insulator transition in disordered systems is reviewed in references [7, 8, 9]. The following sections contain a brief review of this work.

2.5.1 Localised and extended states

In real systems, it is unrealistic to claim that there is a complete absence of disorder in the material. Anderson [6] considered a system of equally spaced periodic potential wells [figure 2.2(a)] in which disorder was introduced by randomly varying the depth of the wells [figure 2.2(b)]. The random potential is large compared to the bandwidth of the electron energies, so therefore the electronic states of the system are localised. The situation is such that

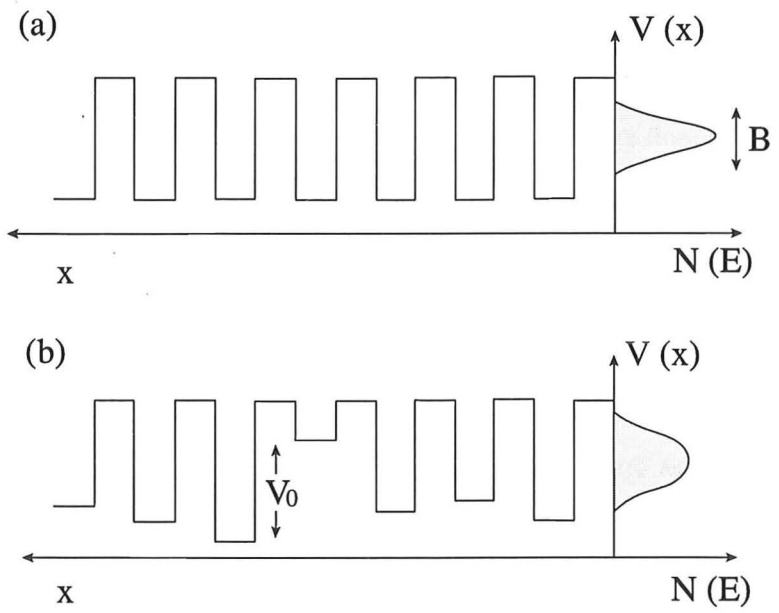

Figure 2.2: Anderson transition in a disordered system. (a) 1D periodic potential and corresponding density of localised states. (b) 1D periodic potential with random well depths in the Anderson model.

the solutions to Schrödingers equation are no longer Bloch waves (extended states) obeying, $\psi(\mathbf{r}) = e^{i\mathbf{k}\cdot\mathbf{r}}u(\mathbf{r})$. If the random potential is small compared to the electron's energy bandwidth, the extended states are separated in energy from the localised states by a mobility edge. Hence the metal-insulator transition occurs as the Fermi energy moves through the mobility edge from the localised to the extended states.

2.5.2 Hopping conduction

Miller and Abrahams [10] first introduced the concept of electron hopping conduction with an equivalent random resistor network on which a resistance R_{ij} connects each pair of donors i and j. The values of R_{ij} can be evaluated from the experimental hopping current. For a weak electric field an electron is promoted between the two donors i and j by a phonon and the resistance

R_{ij} is proportional to the current strength. At low temperatures, R_{ij} can be written as a product of two factors: the first depending exponentially on r_{ij} (inter-site distance) and the second dependent on the donor site energy E_{ij}:

$$R_{ij} = R_{ij}^{0} \exp\left(\frac{2r_{ij}}{a_B^*} + \frac{E_{ij}}{k_B T}\right), \tag{2.9}$$

where a_B^* is effective Bohr radius. The first term describes tunnelling between the sites whilst the second term gives the probability of activation between sites. The values of R_{ij}^{0} and E_{ij} in the above equation are as follows:

$$R_{ij}^{0} = \frac{k_B T}{e^2 \gamma_{ij}^{0}}, \tag{2.10}$$

with

$$\gamma_{ij}^{0} = \frac{D_f^2 \Delta_i^j}{\pi d s^5 \hbar^4} \left(\frac{e^2}{6\pi\varepsilon_0\varepsilon_r a_B^*}\right)^2 \frac{r_{ij}^2}{a_B^{*2}} \left[1 + \left(\frac{\Delta_i^j a_B^*}{2\hbar s}\right)^2\right]^{-4}, \tag{2.11}$$

where D_f is a constant describing the deformation potential, Δ_i^j the potential energy difference between sites i and j, d is the density of lattice spacing, and s is the speed of sound. There is a gap;

$$E_{ij} = \frac{1}{2}(\mid E_i - E_j \mid + \mid E_i - \mu \mid + \mid E_j - \mu \mid), \tag{2.12}$$

where E_i and E_j are the energies of sites i and j, respectively and μ is the chemical potential.

At relatively high temperatures the tunnelling term in equation 2.9 is comparatively small so the temperature dependence of the conductivity as obtained from equation 2.9 follows a simple experimental activation law,

$$\sigma \propto \exp\left(-\frac{W}{k_B T}\right), \tag{2.13}$$

where W is some average energy difference between adjacent states (the activation energy).

At the temperature is lowered, the second term in the exponent of equation 2.9 becomes comparable with the first. In this case, where electrons can be thermally excited from one localised state to another,the net conductivity is obtained by maximising the efficiency of the individual hopping process from one localised state to another. As these need not necessarily be adjacent sites this process is known as variable-range hopping. The distribution of states and the optimisation process intimately involve the dimensionality d of the system, and the general result of 'Mott law' [8] is

$$\sigma = \sigma_0 \exp\left[-\left(\frac{T_0}{T}\right)^{1/(d+1)}\right], \tag{2.14}$$

where T_0 also depends on the dimension. This result has been experimentally verified in one, two and three dimensions.

When long-range electron-electron interactions are dominant, the density of states should continuously reduce to zero at the Fermi level, the so called Coulomb gap. The following calculations have been proposed by Efros and Shklovskii [11]. In a system in its ground state, at zero temperature, the Fermi level separates fully occupied and completely empty states. If the site i (energy E_i) is occupied by an electron and site j (energy E_j) is vacant, moving the electron from site i to site j, requires a change in the Coulomb energy of $e^2/4\pi\varepsilon_0\varepsilon_r r_{ij}$. Therefore, the total energy of the excitation is $E_i^j = E_j - E_i - e^2/4\pi\varepsilon_0\varepsilon_r r_{ij}$. A hopping event from filled to unfilled sites should increase the energy of the system and the inequality $E_i^j > 0$ must be satisfied. Therefore, for two dimensions, the single-particle density of states tends to zero at the Fermi energy:

$$\rho(E) = \frac{2 \mid E - \mu \mid (4\pi\varepsilon_0\varepsilon_r)^2}{\pi e^2}. \tag{2.15}$$

As a result, the hopping formula becomes

$$\sigma \propto \exp\left[-\left(\frac{T_0}{T}\right)^{1/2}\right], \tag{2.16}$$

where $T_0 = \beta e^2/4\pi\varepsilon_0\varepsilon_r a_B^*$ ($\beta \approx 6$ in a 2D system).

2.6 Transport in quantizing magnetic field

2.6.1 Density of states

With no applied magnetic field the energy of 2D electrons occupying a single subband is given by

$$E(k) = \frac{\hbar^2 k^2}{2m^*}. \tag{2.17}$$

The free electron density of states, $\rho(E_F)$ per unit area, is independent of energy as shown by the broken line in figure 2.3(a) and is given by

$$\rho(E) = g_s g_v \frac{m^*}{2\pi\hbar^2}, \tag{2.18}$$

where g_s and g_v are the spin and valley degeneracies, respectively. For GaAs, the values of the spin and valley degeneracies are 2 and 1.

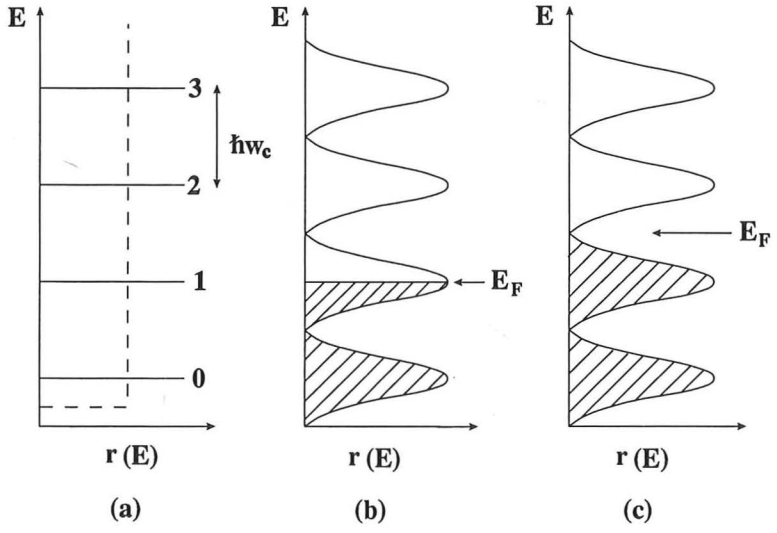

Figure 2.3: The energy levels (Landau levels) of a 2DEG in a perpendicular magnetic field. (a) $B = 0$ (dashed line), $B \neq 0$ (Solid line), ideal system, $E_n = (n + \frac{1}{2})\hbar\omega_c$. (b) and (c) $B \neq 0$, disordered system showing the broadening of the Landau levels into the gaps between the ideal Landau level energies.

In the following, we illustrate the properties of the 2DEG density of states when a strong magnetic field is applied perpendicular to the plane. Classically, with the field applied normal to the layer, the path of an electron travelling with speed v is bent into a circle of radius r, as given by the Lorentz force $m^*v^2/r = Bev$. The electrons travel these orbits with an angular frequency $\omega_c = v/r = Be/m^*$. When treated fully using quantum mechanics, this motion appears to be simple harmonic, and the electron energies are modified from the continuous band of states in zero magnetic field into highly degenerate quantized levels called Landau levels, as shown in figure 2.3. The energies of these levels are

$$E_n = (n + \frac{1}{2})\hbar\omega_c, \; n = 1, \; 2, \; 3, \cdots \tag{2.19}$$

where n is the Landau level index. This analysis has not included the interaction of the magnetic field with the electron spin which will be discussed in subsection 2.6.5.

In real samples, the Landau levels are broadened due to disorder from imperfections and impurities which give rise to variations in the electrostatic potential energy in different parts of the crystal. If the scattering time is τ, the uncertainty principle leads to a broadening by an amount $\delta E \sim \hbar\tau$. The quantisation due to the magnetic field is only important if the energy separation of the Landau levels, $\hbar\omega_c$, is larger than this broadening, and in order to achieve this large magnetic fields and very low temperatures are required.

2.6.2 The Shubnikov-de Haas effect

The electrical properties of the sample depend very strongly upon how the Landau levels are occupied, and hence upon the position of the Fermi level. This is shown in figures 2.3(b) and (c), in which the effects of broadening have been included. In figure 2.3(b) one and a half levels are filled, so

the Fermi energy E_F lies in the extended states. The transport looks like that of a metal, with a high longitudinal conductivity σ_{xx}. Conversely, in figure 2.3(c), two levels are filled, and E_F lies in the localised states. In this case the system resembles an insulator. As the magnetic field is increased the Fermi-energy passes through the Landau levels and the conductance oscillates.

These magnetoconductivity oscillations, known as 'Shubnikov-de Haas' (SdH) oscillations, are characteristic of electrons in a magnetic field and are periodic in B^{-1} (see, for example, Ziman [12]). The periodicity of the conductivity oscillations as a function of magnetic field is given by:

$$\Delta(\frac{1}{B}) = \frac{g_s e}{h n_s}, \tag{2.20}$$

where $\Delta(1/B)$ is the reciprocal magnetic field period. In addition to the oscillations in longitudinal resistance, current flowing in the x-direction will set up an electric field in the y-direction when a magnetic field is applied perpendicular to the plane. In order to obtain expressions for the longitudinal σ_{xx} and transverse σ_{xy} conductance, the conductivity σ and resistivity ρ need to be described by tensors.

For a Hall bar shaped sample, the currents and electric fields are related by the expressions:

$$I_x = \sigma_{xx} E_x + \sigma_{xy} E_y \tag{2.21}$$

$$I_y = -\sigma_{xy} E_x + \sigma_{xx} E_y, \tag{2.22}$$

(since $\sigma_{xx} = \sigma_{yy}$ and $\sigma_{xy} = -\sigma_{yx}$).

If, as usual, we only allow current to flow along one direction (x), then $I_y = 0$, and we can say that $E_y/E_x = \sigma_{xy}/\sigma_{xx}$. Therefore we can define the resistivities as

$$\rho_{xx} = \frac{E_x}{I_x} = \frac{\sigma_{xx}}{\sigma_{xx}^2 + \sigma_{xy}^2}, \tag{2.23}$$

$$\rho_{xy} = \frac{E_y}{I_x} = \frac{\sigma_{xy}}{\sigma_{xx}^2 + \sigma_{xy}^2}. \tag{2.24}$$

When $\sigma_{xy} \gg \sigma_{xx}$, we may write $\rho_{xx} \sim \sigma_{xx}/\sigma_{xy}^2$, and $\rho_{xy} \sim 1/\sigma_{xy} = R_H B$, where R_H is the Hall coefficient ($R_H = 1/n_s e$). For SdH oscillations to be observed, the temperature and the degree of disorder in the system must be sufficiently low and the conditions $\hbar\omega_c > k_B T$ and $\omega_c \tau_q > 1$ must be realized, where τ_q is the quantum life-time.

The classical transverse (Hall) conductivity of free and independent electrons is strictly proportional to the electron concentration n_s,

$$\sigma_{xy} = \frac{e n_s}{B}. \tag{2.25}$$

In terms of atomic units,

$$\sigma_{xy} = \nu \frac{e^2}{h}, \tag{2.26}$$

where ν is the filling factor reflecting the number of filled Landau levels. i.e. ν is an integer when the Fermi level lies midway between the Landau levels. According to equation 2.25 and 2.26,

$$\nu = n_s \frac{h}{eB}. \tag{2.27}$$

The quantum life-time is related to the Landau level broadening Γ_q by the relation $\Gamma_q = \hbar/2\tau_q$ and may be extracted from the magnitude of the SdH oscillations. There is a quantitative difference between the transport life-time τ_t and quantum life-time τ_q in a 2DEG system. For short-range scattering potentials [13, 14, 15, 16, 17], these two life-times are identical, for example in Si MOSFETs where the interface roughness scattering dominates. For high mobility heterojunctions [18, 19, 20], long range remote ionized impurity scattering potentials dominate and backward scattering is suppressed. As a result the transport life-time is strongly enhanced above the quantum life-time by a factor of 10 or more. These effects are discussed more fully in chapter 4.

2.6.3 The quantum Hall effect

In apparent contradiction to the classical Hall resistance, which increases proportional to field, in 1980 plateaus in the Hall resistivity were observed at low temperature and high magnetic fields in silicon MOSFETs by von Klitzing, Dorda, and Pepper [21]. On sweeping the magnetic field the Hall voltage becomes independent of field and develops a 'plateau' at the same fields at which the longitudinal resistivity falls to zero. As the resistivity increases again the Hall voltage rapidly changes to the next 'plateau'. The most interesting feature of this behaviours is that the resistivity of the Hall plateaus occur at integer multiples of h/e^2. This phenomenon is called the integer quantum Hall effect (IQHE). In order to measure the Hall resistivity we measure the current I_x and a voltage V_y, whereas the resistivity depends upon E_y and j_x. Therefore we simply multiply both E_y and j_x by the width of the sample to obtain V_y and I_x. The result of this is that the Hall resistivity V_y/I_x, is independent of the sample width, and equal to

$$V_y/I_x = \rho_{xy} = \frac{1}{\nu} \times \frac{h}{e^2} = \frac{1}{\nu} \times 25,812.8\ \Omega, \tag{2.28}$$

within a certain field around each integer value of filling factor ν. A remarkable feature of the experiment is that this resistance value, determined only by the fundamental Planck's constant h and electron charge e, is extremely accurate.

2.6.4 Edge states

In high magnetic field with well defined Landau levels, the delocalised states are separated from each other by regions of localised states [figure 2.3(c)]. In a free unbounded system the Landau level energies are given by equation 2.19, however in a disorder free system with finite boundaries the Landau levels rapidly increases in energy at the sample edges, figure 2.4. In a disordered system, potential bumps modify the Landau level energies

2.6.3 The quantum Hall effect

In apparent contradiction to the classical Hall resistance, which increases proportional to field, in 1980 plateaus in the Hall resistivity were observed at low temperature and high magnetic fields in silicon MOSFETs by von Klitzing, Dorda, and Pepper [21]. On sweeping the magnetic field the Hall voltage becomes independent of field and develops a 'plateau' at the same fields at which the longitudinal resistivity falls to zero. As the resistivity increases again the Hall voltage rapidly changes to the next 'plateau'. The most interesting feature of this behaviours is that the resistivity of the Hall plateaus occur at integer multiples of h/e^2. This phenomenon is called the integer quantum Hall effect (IQHE). In order to measure the Hall resistivity we measure the current I_x and a voltage V_y, whereas the resistivity depends upon E_y and j_x. Therefore we simply multiply both E_y and j_x by the width of the sample to obtain V_y and I_x. The result of this is that the Hall resistivity V_y/I_x, is independent of the sample width, and equal to

$$V_y/I_x = \rho_{xy} = \frac{1}{\nu} \times \frac{h}{e^2} = \frac{1}{\nu} \times 25,812.8\ \Omega, \tag{2.28}$$

within a certain field around each integer value of filling factor ν. A remarkable feature of the experiment is that this resistance value, determined only by the fundamental Planck's constant h and electron charge e, is extremely accurate.

2.6.4 Edge states

In high magnetic field with well defined Landau levels, the delocalised states are separated from each other by regions of localised states [figure 2.3(c)]. In a free unbounded system the Landau level energies are given by equation 2.19, however in a disorder free system with finite boundaries the Landau levels rapidly increases in energy at the sample edges, figure 2.4. In a disordered system, potential bumps modify the Landau level energies

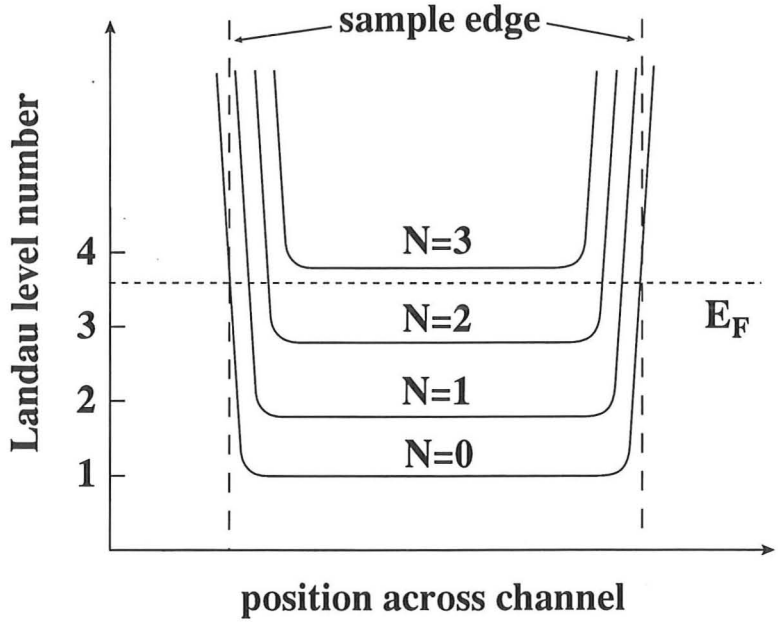

Figure 2.4: Schematic diagram showing the extended state energy levels as a function of position along the sample in 2DEG. The Landau level energies rise sharply near the edges of the sample.

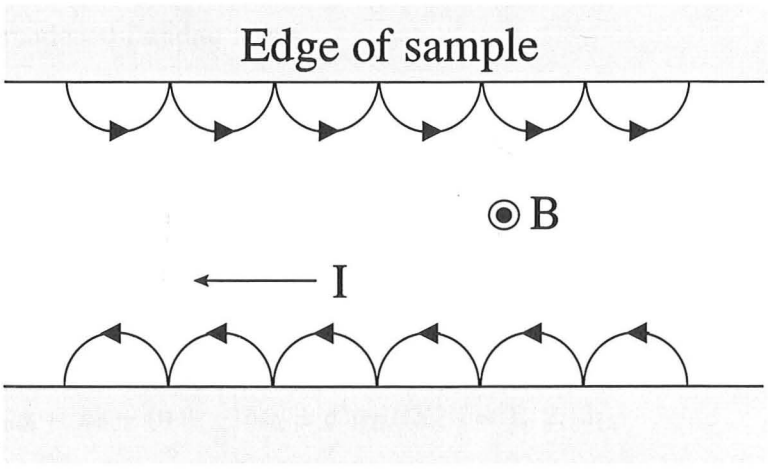

Figure 2.5: Classical picture of edge states in a high magnetic field. When the Fermi level in the bulk lies in the localised states, as depicted, conduction can only occur via the skipping orbits at the edges of the sample.

forming potential islands. When the magnetic length $l_B = \sqrt{\hbar/eB}$ is small compared to the sample width the electrons move around the edge of the device following skipping orbits (figure 2.5). Electrons also follow skipping orbits around the discrete potentials forming islands inside the Hall bar. These 'edge-states' were first suggested theoretically by Büttiker [22] and experimentally verified by Alphenaar [23].

2.6.5 Effect of spin

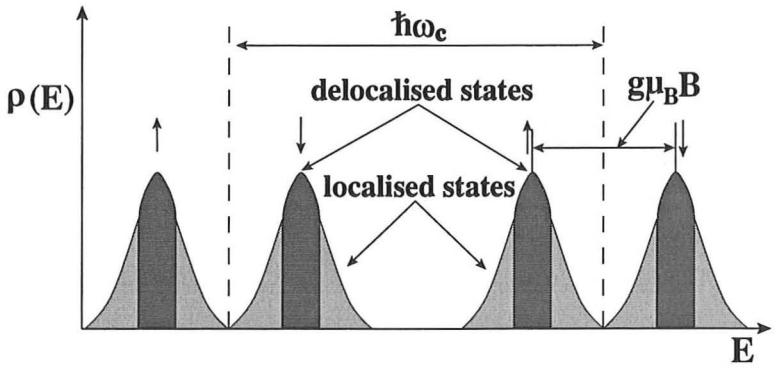

Figure 2.6: A schematic diagram showing the spin-up and spin-down disorder broadened Landau levels.

In the integer quantum Hall effect, odd-numbered Hall plateaus are also observed as the electron spin can be polarised either with or against the magnetic field. Therefore each spin-degenerate Landau level splits into two levels, as shown in figure 2.6. The approximated energy spectrum of a two-dimensional system in the zero disorder limit thus becomes

$$E_{n,k} = E_0 + (n + \frac{1}{2})\hbar\omega_c \pm g^*\mu_B BS,\ n = 1,\ 2,\ 3, \cdots, \tag{2.29}$$

where E_0 is the energy of the system in the absence of a magnetic filed, $\hbar\omega_c$ is the cyclotron energy which is generally larger than the spin-splitting energy, g^* is the enhanced g factor, $\mu_B = e\hbar/2m$ is the Bohr magneton, and $S = \pm 1/2$ is the spin quantum number. As the additional spin dependent term is

generally less than the cyclotron energy, high magnetic fields are required to resolve the two disorder broadened levels. The spin-split energy is divided into two components: (i) the Zeeman energy; (ii) exchange enhancement due to electron-electron interactions [24] and can be described by the following relation:

$$g^*\mu_B B = g\mu_B B + E_{ex}\sum_L (n_L\uparrow - n_L\downarrow), \tag{2.30}$$

where $g\mu_B B$ is the 'bare' spin energy, E_{ex} is the exchange parameter, and $n_L\uparrow$ and $n_L\downarrow$ are the spin level occupations. The experimental value of the bare g factor in bulk GaAs is found to be $|0.44|$ [25] whilst the enhanced g^* factor in a high mobility GaAs-AlGaAs heterojunction is greater than five [26, 27, 28].

Bibliography

[1] H. van Houten *et al.* in *Physics and Technology of Submicron Structures,* (H. Heinrich, G. Baure, and F. Kuchar, eds). Springer, Berlin, (1988)

[2] B. L. Al'tshuler, A. G. Aronov, and P. A. Lee, Phys. Rev. Lett. **44**, 1288 (1980).

[3] H. Fukuyama, J. Phys. Soc. Japan **48**, 2169 (1980).

[4] N. F. Mott, Proc. Phys. Soc. **62**, 416 (1949).

[5] N. F. Mott, Rev. Mod. Phys. **40**, 677 (1968).

[6] P. W. Anderson, Phys. Rev. **109**, 1492 (1958).

[7] N. F. Mott, *Metal-Insulator Transitions,* (Taylor and Francis: London) (1974).

[8] N. F. Mott, *Electronic Processes in Non-Crystalline Materials,* (Oxford University Press, Oxford, 1979).

[9] *The Metal-Insulator Transition in Disordered Systems,* edited by L. R. Friedman and D. P. Tunstall (SUSSP, Edinburgh, 1978).

[10] A. Miller and E. Abrahams, Phys. Rev. **120**, 745 (1960).

[11] A. L. Efros and B. I. Shklovskii, J. Phys. C **8**, L49 (1975).

[12] J. M. Ziman, *Electrons and phonons,* OUP (Oxford), (1960).

[13] M. A. Paalanen, D. C. Tsui, and J. C. M. Hwang, Phys. Rev. Lett. **51**, 2226 (1883).

[14] J. P. Harrang, R. J. Higgings, R. K. Goodall, P. R. Jay, M. Laviron, and P. Delescluse, Phys. Rev. B **32**, 8126 (1985).

[15] S. Das Sarma and F. Stern, Phys. Rev. B **32**, 8442 (1985).

[16] S. Das Sarma and B. Vinter, Phys. Rev. B **24**, 549 (1981).

[17] P. T. Coleridge, R. Stoner, and R. Fletcher, Phys. Rev. B **39**, 1120 (1989).

[18] S. Ben Amor, L. Dmowski, J. C. Portal, K. P. Martin, R. J. Higgins, and M. Razeghi, Appl. Phys. Lett. **52**, 2915 (1990).

[19] U. Bockelmann, G. Abstreiter, G. Weimann, and W. Schlapp, Phys. Rev. B **41**, 1120 (1990).

[20] A. C. Churchill, G. H. Kim, A. Kurobe, M. Y. Simmons, D. A. Ritchie, M. Pepper, and G. A. C. Jones, J. Phys.: Condens. Matter **6**, 6131 (1994).

[21] K. von Klitzing, D. Dorda, and M. Pepper, Phys. Rev. Lett. **45**, 494 (1980).

[22] M. Büttiker, Phys. Rev. B **38**, 9375 (1988).

[23] B. W. Alphenaar, P. L. McEuen, R. G. Wheeler, and R. N. Sacks, Phys. Rev. Lett. **64**, 677 (1990).

[24] T. Ando and Y. Uemura, J. Phys. Soc. Jpn. **37**, 1044 (1974).

[25] A. M. White, I. Hinchliff, P. J. Dean, and P. D. Greene, Solid State Commun. **10**, 497 (1972).

[26] Th. Englert, D. C. Tsui, A. C. Gossard, and Ch. Uihlein, Surf. Sci. **113**, 295 (1982).

[27] R. J. Nicholas, R. J. Haug, K. v. Klitzing, and G. Weimann, Phys. Rev. B **37**, 1294 (1988).

[28] A. Usher, R. J. Nicholas, J. J. Harris, and C. T. Foxon, Phys. Rev. B **41**, 1129 (1990).

Chapter 3

Device Processing and Measurement Techniques

3.1 Introduction

In this chapter the processing of a device from a typical MBE grown wafer and the low temperature measurement techniques employed in the study of semiconductor transport properties are described. This discussion is divided into three sections. The first, section 3.2, outlines optical and electron beam lithography: the former has been used to define the large scale features ($>$ 1 μm), whilst the latter has been used to customize small patterns ($<$ 1 μm). Section 3.3 describes the cryostats used to achieve the low temperatures ($<$ 4.2 K) necessary for this work. Finally, section 3.4 describes the electrical circuits used to measure the properties of the devices.

3.2 Optical lithography

Optical lithography is used to fabricate relatively large structures such as Hall bars, ohmic contacts and gate pads. The standard steps in the optical lithography processes are illustrated in figure 3.1. The MBE grown wafer, 3

inches in diameter must first be cleaved into more manageable sized sections. The orientation of these sections with respect to the wafer flat is indicated by a line scribed onto the surface. This enables a study of the transport characteristics in the two orthogonal directions.

The cleaved chip was dipped in a dilute HCl solution for 15 seconds to remove surface oxides. Mesa fabrication begins by spinning photoresist onto the surface of the cleaved chip [figure 3.1 (a)]: Shipley 1813 photoresist was spun on at 5500 rpm for 30 seconds to give a layer approximately 1500 nm in thickness. The chip was then baked for 10 minutes at 90°C in a fan oven to dry off any remaining solvent and to harden the resist. A chrome-on-quartz glass photomask designed for a Hall bar mesa was held above the sample to selectively expose the photoresist using ultra-violet light for 3.5 seconds [figure 3.1 (b)]. The areas exposed to the UV radiation become soluble in Shipley LF319 developer. Immersion in the developer for 20 seconds followed by a rinse in de-ionized water is sufficient to remove the unwanted resist. The chip was then immersed in $H_2SO_4 : H_2O_2 : H_2O$ mixture in the ratio 1:8:160, this solution has an etchrate of ≈ 25 Å/s at room temperature. The depth of the mesa is checked with a Sloan Dektak profiler to ensure that the Hall bar is etched below the 2DEG [figure 3.1 (d)]. All resist is removed from the chips' surface by immersing the sample in acetone.

The most common technique used to fabricate conventional ohmic contacts to a 2DEG is based upon an annealed AuNiGe metallization. After exposure through a second photomask, the chip was soaked for 2 minutes in chlorobenzene to harden the top surface of the photoresist. The chip was next developed in a developer solution for 90 seconds and washed in de-ionized water. The hardened surface of the resist develops at a slower rate than the lower layers and an overhang edge profile is produced. This is necessary for easy lift-off of the subsequent metallization stages. The sample was dipped in a dilute HCl solution for 15 seconds to remove the oxide layer

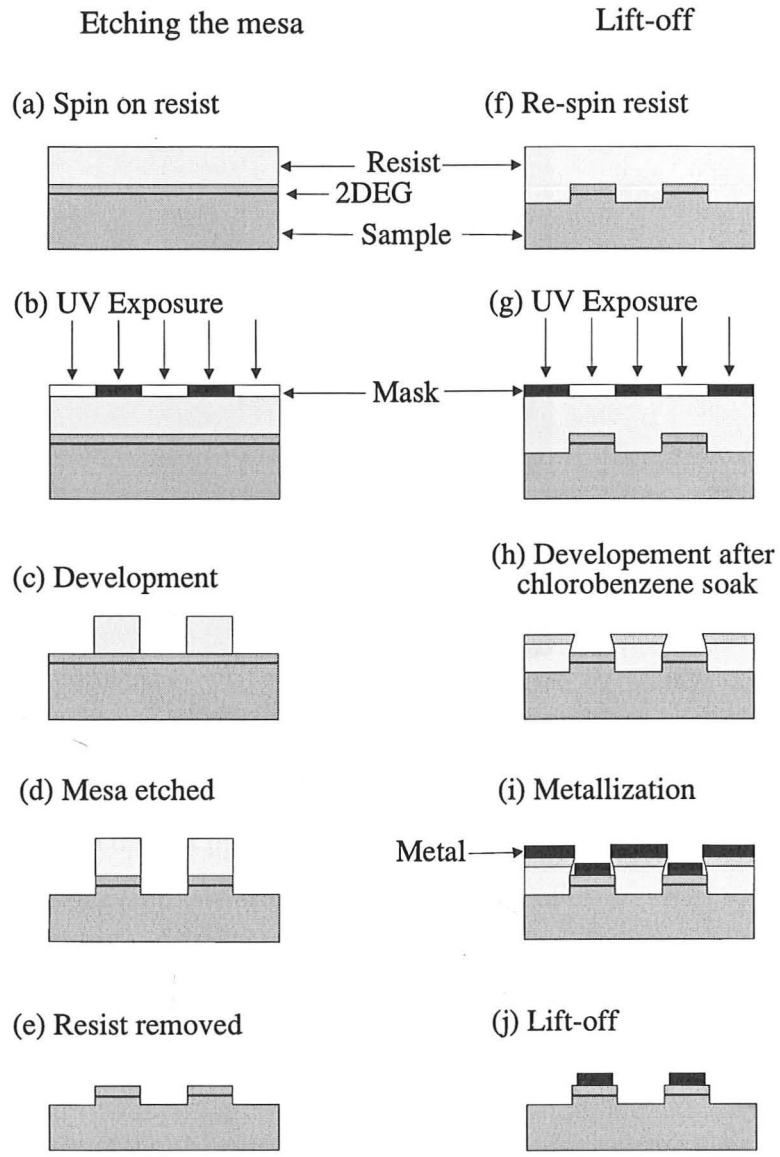

Figure 3.1: A schematic diagram showing the optical lithography processing steps.

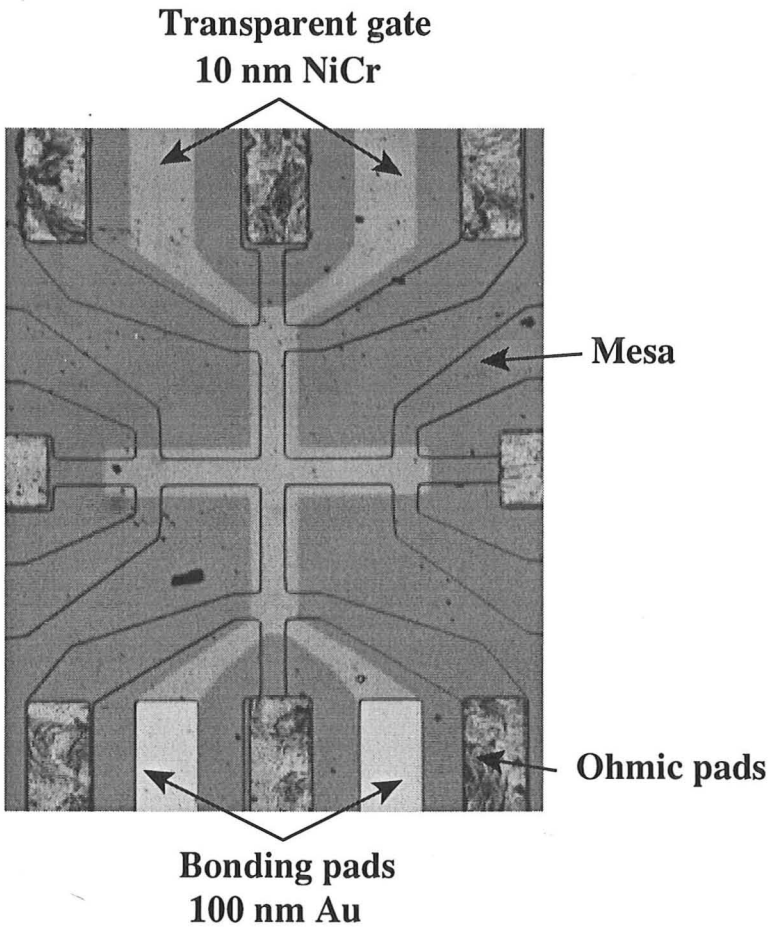

Figure 3.2: An optical photograph (50 × magnification) of a completed Hall bar with ohmic contacts and a transparent full gate.

from the surface, hence improving the adhesion of the ohmic metallization. A 150 nm layer of AuGeNi alloy in the ratio 88:12:1 followed by 30 nm of Au were evaporated onto the surface at a pressure less than 1×10^{-6} mbar. Subsequently the evaporated metal was annealed, at 430 °C for 80 seconds in a N_2-H_2 atmosphere such that the metal diffused down through the chip and contacts the 2DEG.

At this stage the quality of the contacts was examined for linear I – V characteristics on a probe station both at room temperature and at 77 K to check that good contact to the 2DEG has been established. It is quite

common for contacts to 'freeze-out', becoming highly resistive at low temperatures. If this is the case, the chip can be re-annealed to improve the poor contacts.

The procedure for depositing a Schottky gate on the structure is similar to that for depositing the ohmic contact metallization. The gate metallization used was a 10 nm layer of NiCr, which adheres very well to the GaAs surface. This thickness of NiCr forms a transparent gate which allows the carrier density in the 2DEG to be increased by using a red LED. In order to make electrical contact to the NiCr gate a 100 nm Au layer was evaporated to create bond pads (see figure 3.2). The completed Hall bar is shown in figure 3.2.

3.3 Electron-beam lithography

After conventional processing of the sample into Hall bars, electron beam lithography is frequently used to fabricate submicron features. There are many excellent review papers on electron beam lithography [1, 2]. A positive-acting resist called poly-methyl-metha crylate (PMMA) is the most commonly used electron beam resist. A thin 150 nm layer of PMMA was spun onto the chip and baked in an oven at 150°C for more than 30 minutes. The electron beam lithography is carried out in a modified Hitachi S800 scanning electron microscope (SEM) with a 25 keV electron beam. The patterned chip was developed in a solution of 3 parts propanol to 1 part methyl isobutyl ketone (MIBK) for 20-40 seconds. The device was then etched with the $H_2SO_4 : H_2O_2 : H_2O$ mixture to a depth of about 170 nm, which is below the 2DEG. Figure 3.3 shows the SEM image of a number of narrow constructions defined by e-beam and chemical etching.

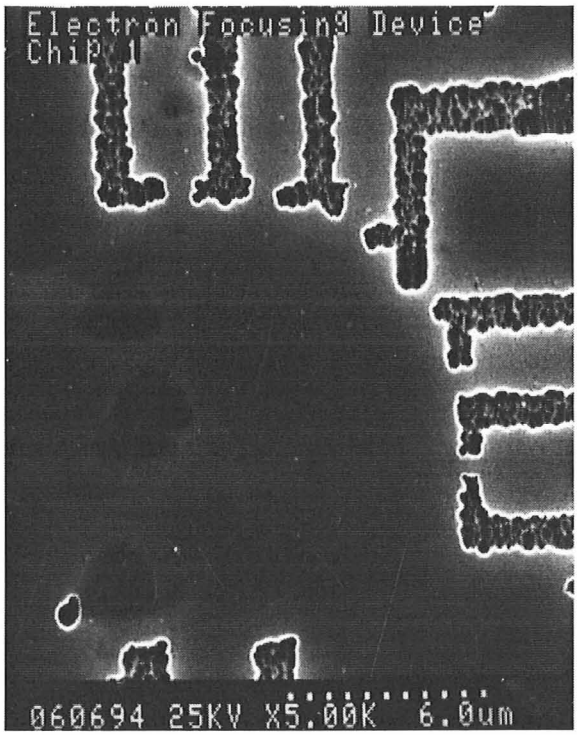

Figure 3.3: A scanning electron micrograph of a number of nanostructures defined by electron beam lithography.

3.4 Cryogenic systems

Most of the measurements described in this thesis were carried out at low temperature (< 4.2 K). Low temperatures are required to observe the quantum mechanical properties of electrons in the semiconductor structure. In this section, the cryostats used in this work at the Semiconductor Physics Group, Cavendish Laboratory will be briefly described.

After a device's fabrication, we initially check the performance of the device before continuing with extensive measurements in a ^{3}He cryostat or ^{3}He/^{4}He dilution refrigerator. The simplest assessment involves immersing the device into a 'dipping dewar' of liquid Helium (4.2 K). The device is mounted in a Charntek holder and is connected to an external aluminum contact box via a number of electrical wires. The performance of the gate,

ohmic contacts and the gate leakage, can then be quickly determined.

An Oxford Instruments pumped ^{4}He system was frequently used for measurements at temperatures down to 1.5 K and magnetic fields up to 8 T (using superconducting solenoids). The sample is again mounted in a probe and inserted into the cryostat's sample space: a sealed airspace surrounded by insulating vacuum liquid Helium and Nitrogen jackets. The sample space is periodically filled with liquid helium from the main reservoir through a needle valve. By pumping on the liquid helium the sample space temperature can be reduced to, and maintained at 1.5 K for 6-8 hours. The sample temperature was monitored with a calibrated resistance thermometer affixed near the sample. The magnetic field was calculated from the magnetic power supply current. The helium and the liquid nitrogen jackets are refilled every day to maintain 4.2 K in the main helium bath. Using this system the base temperature can be obtained in 5-10 minutes and samples may be changed quickly. Using a sample heater and varying the pumping rate, the temperature can be varied over the range 1.5 K to 20 K.

An Oxford Instruments ^{3}He croystat provided measurement temperatures down to 300 mK and magnetic fields up to 12.5 T. A device is mounted on the end of a probe which is gently lowered into the ^{3}He space, gradual cooling over 50 minutes is necessary to avoid excessive heating of the ^{3}He. To condense ^{3}He in the sample space, an external tank containing gaseous ^{3}He in a carbon matrix (graphite sorb) is heated to 45 K to drive out the ^{3}He gas. The vapor is passed through tubing cooled to 1.2 K via a pumped ^{4}He pot and the condensed ^{3}He liquid passed into the sample space. This takes approximately 1 hour. In order to cool the sample to 300 mK the graphite sorb is cooled to 4.2 K and acts as a pump on the liquid ^{3}He. The minimum temperature (300 mK) can be maintained for $\sim$ 2 days before the ^{3}He needs to be recondensed.

An Oxford Instruments 400 TLM top-loading dilution refrigerator can

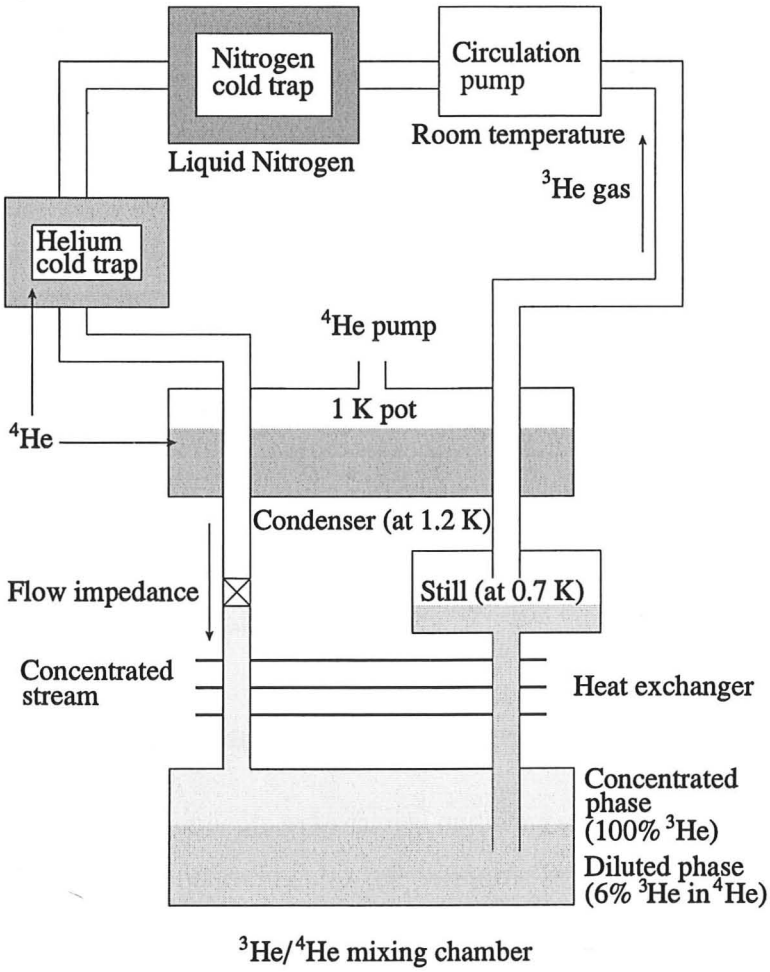

Figure 3.4: A schematic diagram showing a dilution refrigerator.

achieve temperatures between 600 mK to 20 mK and magnetic fields up to 13.6 T. A device is mounted on a probe and the probe lowered as in the ^{3}He cryostat. Once fully inserted, base temperature is reached in about 2-3 hours. A schematic diagram of a fridge is given in figure 3.4. When the mixture of liquid ^{3}He and ^{4}He is cooled below a critical temperature (about 860 mK), it separates into two phases. The light concentrated phase is almost pure liquid He^3 and the heavier dilute phase is about 6% ^{3}He in 94% ^{4}He. The cooling mechanism is obtained from the evaporating of ^{3}He from the concentrated phase into the dilute phase. The atoms of ^{3}He

which are removed from the dilute phase are recondensed into liquid ^{3}He at the still. The room temperature pumping system then removes the ^{3}He gas from the still, passes it through the nitrogen and helium cold traps to remove impurities, and returns it to the concentrated phase. The ^{3}He is condensed by passing it through a tube in thermal contact with the helium main bath and condensing on the 1 K pot. A flow impedance in front of a capillary tube is used to maintain a high enough pressure in the 1 K pot region for the gas to condense whilst allowing a flow pass through at a reduced pressure. The liquid ^{3}He enters then the condensed phase after passing through heat exchangers to pre-cool the liquid between the condensor and the mixing chamber. The continuous circulation of the ^{3}He allows the base temperature to be maintained indefinitely.

3.5 Experimental set-up for electrical measurement

The transport measurements were carried out using standard phase-sensitive techniques. The low experimental temperatures require very low currents to avoid Joule heating of the electrons. Low frequency alternating current (ac) techniques using lock-in amplifiers allow accurate measurement of small output signals, whilst coaxial cable and twisted pairs of wires are used to minimize noise pickup. The frequencies typically used were 78 Hz or 34 Hz, although a lower frequency (< 15 Hz) was used for high resistivity (> 25 kΩ) measurements. Care must be taken with regard to the earthing of the measuring circuit to prevent ground loops. Ideally the cryostat is used as the ground, and all other equipment is then grounded to the cryostat. If a screened room is used, the cryostat ground is passed through filters to the instruments outside the screened room.

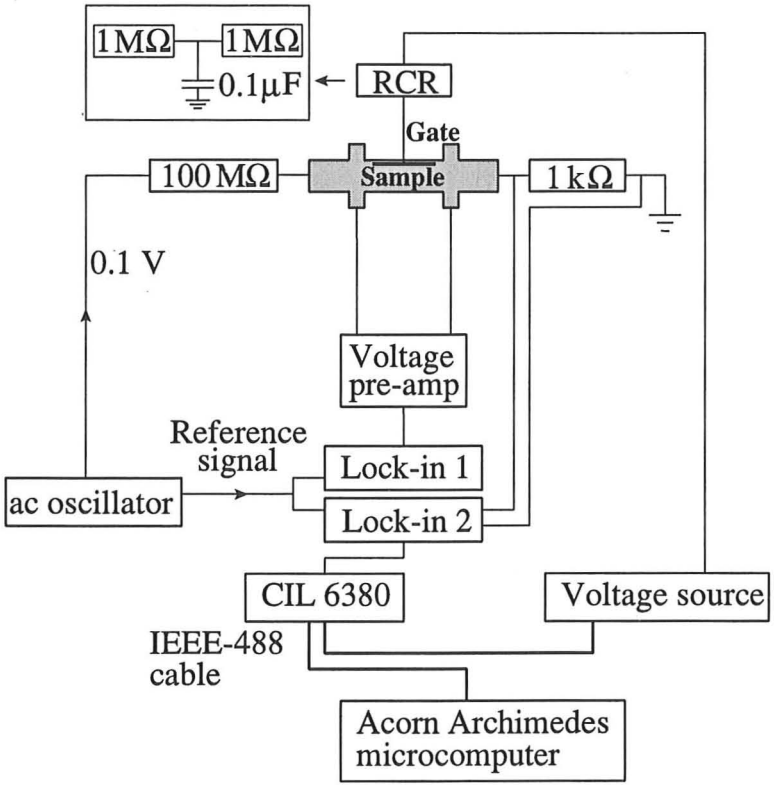

Figure 3.5: The circuit used for four-terminal resistance measurements using constant current biasing.

3.5.1 Four-terminal resistance measurement

The majority of the experiments in this thesis were performed using four-terminal resistance measurements. A constant current (1 nA) is obtained by connecting an ac voltage (0.1 V) through a large series resistance (typically 100 MΩ) to the device. When the device resistance is much less than the series resistance, a constant current flows in the circuit. The voltage drop along the device (related to the longitudinal resistance $R_{xx} = V/1$ nA) was measured with lock-in amplifiers via a voltage pre-amplifier (Stanford SR560 or Brookdeal 5006) if necessary. A second lock-in amplifier was used to measure the current via a 1kΩ resistor. An IOTech Quad voltage source provided direct current (dc) voltage for the gate. The signal from the lock-in

amplifier was transferred to a computer after converting the signal from analogue to digital through a CIL 6380 ADC. The four-terminal measurement circuit is shown schematically in figure 3.5.

3.5.2 Two-terminal conductance measurement

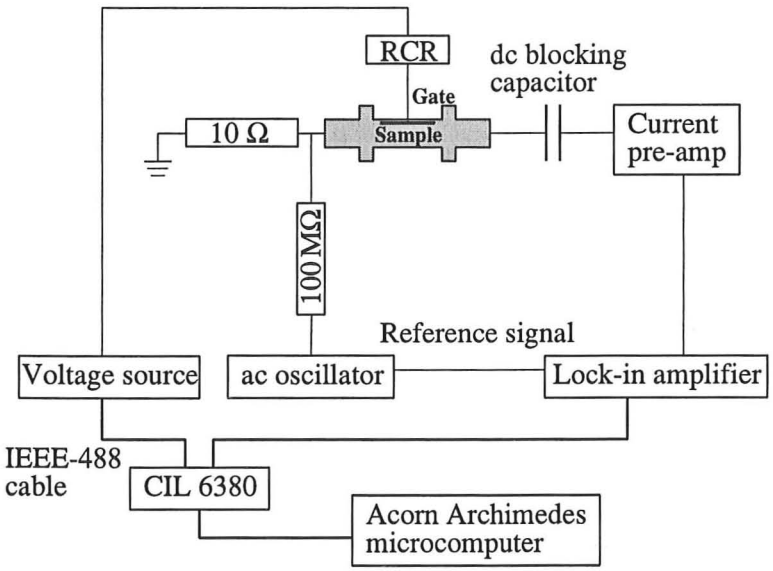

Figure 3.6: The circuit used for two-terminal conductance measurements using constant voltage.

The two terminal conductance measurement requires a constant voltage as shown in figure 3.6. The two-terminal technique was used to measure the conductance of highly resistive devices. A constant low frequency ac voltage, typically 10-100 μV, is provided by applying the signal from the output of an ac oscillator, via a voltage divider, to the source of the device. The current flowing through the device was measured with a virtual ground current pre-amplifier connected to the drain. However, the current pre-amplifiers input has a small ($\sim$ 0.1 mV) dc offset voltage thus a large blocking capacitor ($\sim$ 40 μF) was used to ensure that this dc bias was not dropped across the device. The output voltage from the pre-amplifier is measured by a lock-in

amplifier (usually Brookdeal 9503). The measured current is proportional to the conductance of the device. To avoid electron heating, the current through the device is kept small.

3.5.3 Data recording and analysis

All of the experimental data in this thesis was recorded using a program called 'CryoMeas' written by Dr. Chris Ford. This program, running on an Acorn Archimedes computer, can control a wide variety of equipment: lock-in amplifiers, temperature controller, voltage sources and sweeping the magnetic field.

Data obtained through CryoMeas can be analyzed, plotted, fitted to curves etc. by a second program called 'Lab Assistant', also written by Dr. Chris Ford.

3.6 Summary

In this chapter the optical processing techniques used to process wafers into Hall bar samples has been described. A brief explanation of electron beam lithography was given. Various experimental techniques were also discussed.

Bibliography

[1] G. R. Brewer, *Electron-Beam Technology in Microelectronic Fabrication,* Academic Press, New York, (1980).

[2] R. Thornton, Adv. Electron Phys. **48**, 272 (1979).

Chapter 4

Magnetotransport on (311)B GaAs Substrates

4.1 Introduction

In this chapter we consider magnetotransport in a 2DEG grown on (311)B GaAs substrates. In order to understand the origin of an anisotropic mobility, dependent upon the direction of electron propagation, we first need to introduce the properties of (311) structures. These are reviewed in section 4.2. In section 4.3, we discuss and compare the anisotropic transport life-time with the isotropic quantum life-time. In section 4.4, we will introduce the scattering mechanisms behind the low-temperature anisotropic transport life-time: interface roughness and ionized impurity scattering. The theoretical calculation and experimental data are then compared [1]. We also describe transverse magnetic focusing experiments [2] which demonstrate that both the effective mass and Fermi surface are isotropic in the two orthogonal directions $[\bar{2}33]$ and $[01\bar{1}]$, even though the mobility is anisotropic. The experiment can be also seen as a method to study electron scattering. Such an application will be illustrated in a determination of the electron ballistic length. The results presented here demonstrate that the

(311)B surface can be used to fabricate high mobility samples [3].

4.2 (311) structures

All of the devices studied in the course of this chapter were fabricated on silicon doped GaAs-AlGaAs hetrostructures grown on a (311)B oriented substrate. Most modulation-doped GaAs-AlGaAs hetrostructures are grown on the (100) orientation, which is not necessarily the optimum orientation. In this section, I shall describe the structure of the (311) surface.

The (311) surface is cut 25° towards the $[01\bar{1}]$ direction from the conventional (100) and the properties of the (311) surface can be explained by comparison with other surface orientations. Consider the (111)B and (100) surfaces. Each (100) surface atom has one double-dangling bond and each (111)B surface atom has one single-dangling bond. Generally, every adsorption site in a GaAs (100) orientated crystal grown by MBE is a double-dangling bond site at which the dopant can be strongly bonded. On the other hand, dopant on GaAs (111)B surfaces must be bonded to single-dangling bond sites. In contrast to this, the (211)B, (311)B, and (511)B surfaces are composed of both single- and double-dangling bond sites. In the case of the (211)B surface, there are twice as many single-dangling bond sites as double-dangling bond sites. For the (511)B orientation and higher index planes, the double-dangling bonds outnumber the single-dangling bonds. However, the (311)B surface consists of equal densities of both Ga double-dangling bond sites and As single-dangling bond sites as shown in figure 4.1. Therefore, on the (311)B plane silicon dopants bond to the As atoms, taking up Ga lattice sites whereas, on the (311)A plane, the silicon bonds to Ga atoms, taking up As lattice sites. Wang *et al.* [4] have reported the use of silicon selectively as either an n- or p-type dopant in GaAs-AlGaAs grown on high index substrates; silicon behaving as an n-type dopant on (311)B orientation and p-type on (311)A.

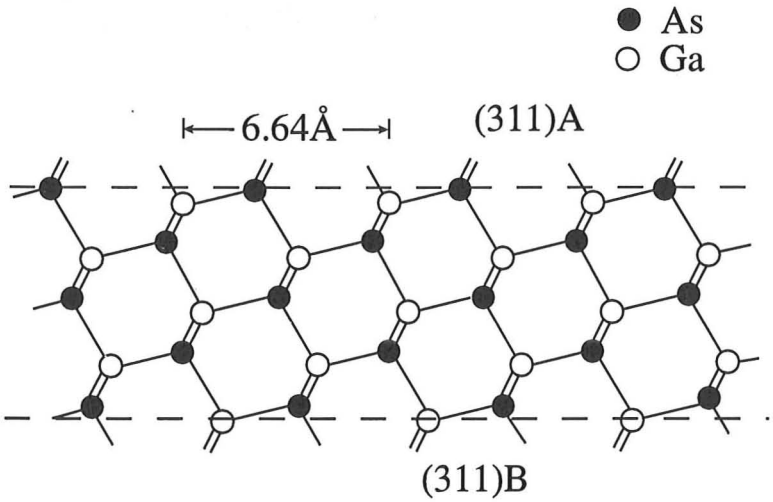

Figure 4.1: A schematic diagram of (311) GaAs along the $[01\bar{1}]$ direction showing the single-dangling and double-dangling bond sites.

Under certain growth conditions the (311) GaAs surfaces relax giving rise to undulations or regular corrugations. Nötzel *et al.* [5], together with Daweritz, [6] have observed reflection high-energy electron diffraction (RHEED) patterns during growth that can be interpreted as arising from regular corrugations running in the $[\bar{2}33]$ direction. Such corrugations can be explained through an energetically favourable surface relaxation, which has been found to be temperature dependent. At typical growth temperatures (630 °C) they find that the surface relaxes into a periodic superlattice of 32 Å period and 10.2 Å height. A schematic diagram of the stepped (311) surface is shown in figure 4.2. Indeed, Nötzel *et al.* [7] have also presented evidence that, under certain growth conditions, such corrugations have been observed in high resolution transmission electron microscopy (TEM) and can explain energies and line shapes observed in photoluminescence spectra.

All of the orthoganal Hall bars used in this work were orientated along the orthogonal $[\bar{2}33]$ and $[01\bar{1}]$ directions. Cleaved (311)B wafers have two bevelled edges and the $[\bar{2}33]$ and $[01\bar{1}]$ directions run perpendicular and

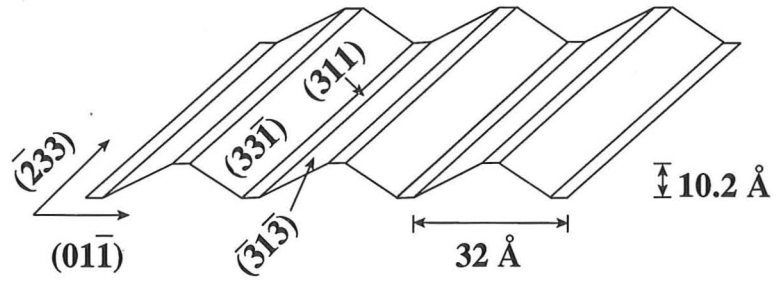

Figure 4.2: A schematic diagram of stepped (311) GaAs surface.

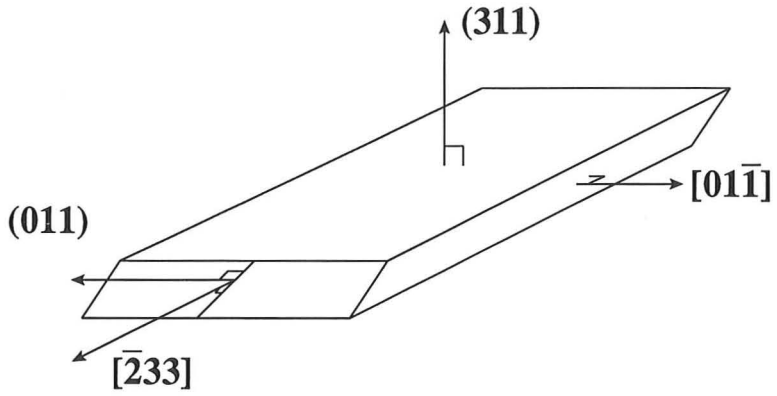

Figure 4.3: A schematic diagram showing a cleaved (311)B wafer.

parallel to these edges (see figure 4.3).

4.3 Transport and quantum life-times

There are two different characteristic electron life-times which are important in determining the transport properties of a 2DEG system: transport life-time τ_t and quantum life-time τ_q. It has been shown both theoretically [8, 9] and experimentally [10, 11] that there is a large difference between the transport life-time and quantum life-time in high-mobility GaAs-based heterojunctions.

Transport life-time is defined by the relaxation-time approach to the Boltzmann equation, and is related to the conductivity by $\sigma = n_s e^2 \tau_t / m^*$ where n_s is the carrier density and e and m^* are the electronic charge and

effective mass, respectively. On the other hand, quantum life-time is connected with the amplitudes of the SdH oscillations and with the Landau level broadening Γ_s by the relation $\tau_q = \hbar/2\Gamma_s$ and gives rise to such effects as renormalization of the density of states and rounding-off of the polarizability function [12, 15]. Thus, quantum life-time is an important time scale in order to understand the effect of the electron-impurity interactions on the density of states.

Theoretically, both life-times are considered functions of the probability of scattering an electron through an angle θ. The transport life-time is weighted by the scattering angle θ as

$$\frac{1}{\tau_t} = \int_0^{\pi} \nu(\theta)(1 - cos\theta)d\theta, \tag{4.1}$$

where the differential cross section, $\nu(\theta)$, is given by elsewhere [11]. The quantum life-time, which is the total scattering rate, is given by

$$\frac{1}{\tau_q} = \int_0^{\pi} \nu(\theta)d\theta. \tag{4.2}$$

For short-range potentials, such as interface roughness scattering in metal-oxide semiconductor (MOS) structures and bulk systems, the two life-times are identical. However, for the long-range potential associated with donors which are placed away from the GaAs-AlGaAs heterointerface, the dominant scattering mechanism involves remote ionized impurities. There produce predominantly small angle scattering and as a result the two life-times differ by a factor of 10 or more [14].

Experimentally, the transport and quantum life-times can be determined from the longitudinal magnetoresistance at zero and higher magnetic fields, (through SdH oscillations prior to spin splitting) respectively. The transport life-time, identical to the mean-life time used in Chapter 2 section 2.2, τ_t is given by

$$\tau_t = \frac{m^*\mu}{e} = \frac{m^*}{n_s e^2 \rho_0}, \tag{4.3}$$

where ρ_0 is the longitudinal magnetoresistivity at zero magnetic field. The transport life-time depends generally on the energy of the electrons, but at low temperatures it can be shown that in this equation only the life-time at the Fermi energy is important. On the other hand, quantum life-times can be determined from 'Dingle plots' and are connected with the oscillatory part of the longitudinal magnetoresistivity (SdH oscillations). The magnitude $\Delta\rho(B)$ is given by;

$$\Delta\rho(B) = 4\rho_0 X(T)\exp\left(-\frac{\pi}{\omega_c\tau_q}\right), \tag{4.4}$$

where we have used $\Delta\rho(B) = \rho(B) - \rho_0$, the cyclotron frequency ω_c, and a temperature reduction factor $X(T)$ given by;

$$X(T) = \frac{(2\pi^2 kT/\hbar\omega_c)}{\sinh(2\pi^2 kT/\hbar\omega_c)}. \tag{4.5}$$

In calculating the temperature dependence of the oscillation amplitude $[X(T)]$, we used the quantum life-time obtained at 1.7 K and then fitted the equation 4.5 using the peak-to-peak values of normalized resistivity. The value of the quantum life-time can be extracted from the exponential function in equation 4.4. In figure 4.4, we plot the logarithm of oscillation amplitudes $[\Delta\rho(B)]$ as a function of reciprocal magnetic field 1/B. These points lie on a straight line with a slope of $-\pi m^*/e\tau_q$. The results from sample T104 for the transport and quantum life-times as functions of carrier density are summarized in figure 4.5. Varying the gate voltage from 0 to 0.5 V, it is possible to investigate the carrier density dependence of these quantities between $n_s = 1.6\times10^{11}$ cm^{-2} and $n_s = 4.2\times10^{11}$ cm^{-2}. It can be seen that the quantum life-time ($\sim$ 1 ps) has virtually no dependence on either carrier density or the direction of current. The transport life time is between 10 and 60 times higher than the quantum life-time. Such ratios of quantum transport life-times are typical of a high mobility 2DEG in which the dominant scattering is due to remote ionized impurities [8]. The observation of anisotropy in the transport life-time but not the quantum life-time is striking

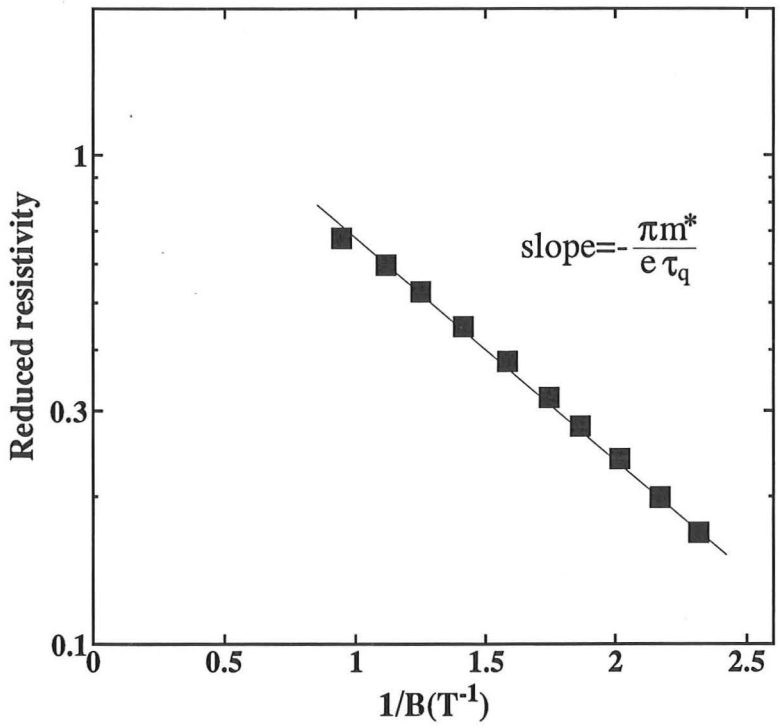

Figure 4.4: Dingle plot from the method of calculating the longitudinal oscillation amplitude. The temperature is 1.7 K.

and could be explained by some form of anisotropic scattering mechanism. The quantum life-times are derived from SdH oscillations, which presuppose that the electrons are moving in cyclotron orbits. Thus the electron experiences scattering in all directions as it travels on its circular path and hence the quantum life-time has no directional dependence. At low fields, in the region where transport life-time is measured, the electron predominantly moves in one direction and thus anisotropic scattering will affect the value of transport life-time.

Although the transport life-time at low carrier densities is almost independent of direction, as the carrier density is increased the anisotropy in the transport life-time also increases. The increased anisotropic transport life-time at higher carrier density is due to the interface roughness scattering.

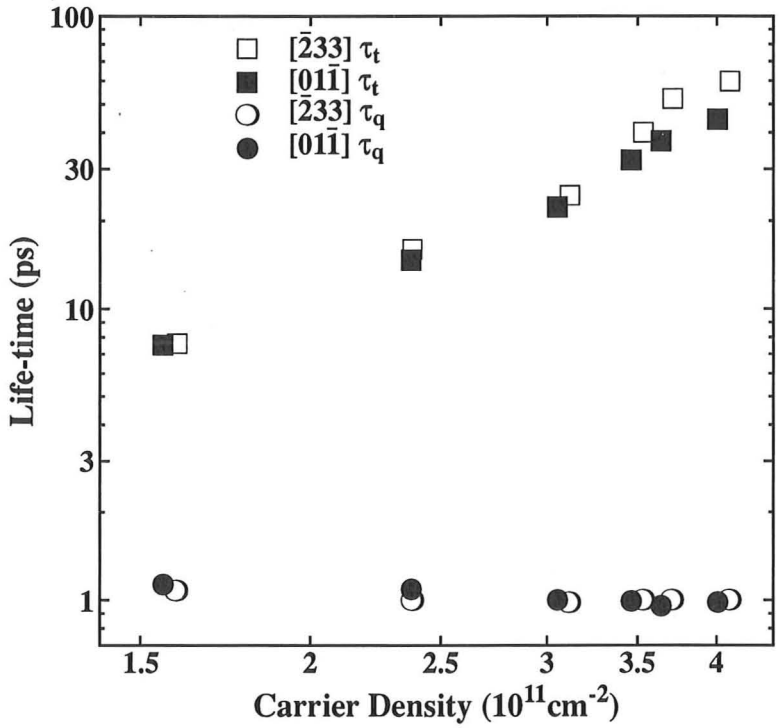

Figure 4.5: Transport τ_t and quantum τ_q life-times for a (311)B 2DEG sample T104 over a range of carrier densities. The life-times were derived from zero magnetic field mobility values and SdH data. Note the small anisotropy in quantum life-times but a large anisotropy in transport life-times as carrier density increases.

This is investigated in section 4.4.2.

4.4 Anisotropic transport at low temperature

4.4.1 Magnetoresistivities for orthogonal directions

Initial magnetoresistivity measurements in this sample (T104) also suggest a marked anisotropy in the mobility in the orthogonal directions. Figure 4.6 shows the typical magnetoresistance in two directions for a sample measured at 1.7 K. The magnetic field is oriented perpendicular to the plane of the

2DEG and the carrier density is 3.2×10^{11} cm^{-2}. The mesa structure consists of two orthogonal Hall bar each with a channel length of 320 μm and a channel width of 80 μm. In each of the two directions Hall and resistivity measurements yield mobilities of 5.3×10^5 cm^2/Vs and 1.4×10^6 cm^2/Vs for $[01\bar{1}]$ and $[\bar{2}33]$ directions, respectively, at the same carrier density. It can be seen that at high fields $B > 0.2$ T, for which $\mu B > 1$ and $\hbar\omega_c > kT$, SdH oscillations are observed that are essentially identical in the two orthogonal directions. However, at low fields ($B < 0.2$ T) a negative magnetoresistance is observed which is directionally dependent; very pronounced in the $[01\bar{1}]$ direction. As the zero-field resistance in the $[01\bar{1}]$ orientation is higher than in the $[\bar{2}33]$ direction, the mobility is reduced and the $[01\bar{1}]$ orientation is termed the 'slow' direction. There is some negative magnetoresistance in the $[\bar{2}33]$ direction but this is negligible compared to that of the $[01\bar{1}]$ direction.

4.4.2 Scattering by anisotropic interface roughness and ionized impurity

In this section we consider the interface roughness and remote ionized impurity scattering. It is well known that the mobility at low temperatures is mainly due to the remote ionized impurities and that the interface roughness scattering becomes larger at high carrier densities. A Fang-Howard wavefunction (see Appendix A.1) is used in these calculations in which the shape of the wavefunction changes as the carrier density is varied. The calculation of the mobility due to the ionized impurities follows a theory by Ando *et al.* [13], in which the mobility is calculated from an integration of the scattering rate over θ with a weight function $(1-\cos\theta)$ (see equation 4.1), where θ is the relative scattering angle. The topology of the interface roughness scattering is modeled by a Gaussian correlation as a function of

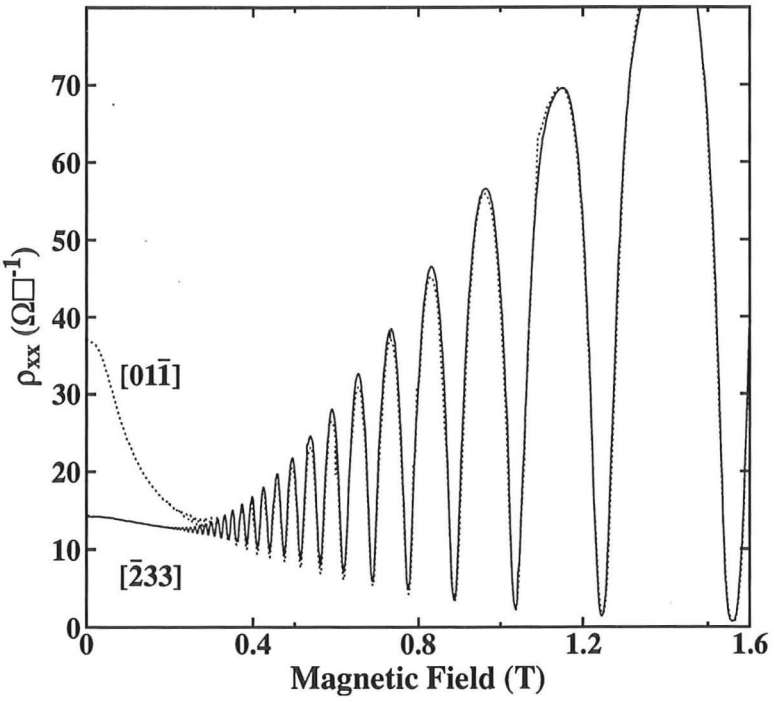

Figure 4.6: $\rho_{xx}(B)$ for a 2DEG, sample T104, on (311)B GaAs measured in two orthogonal directions, namely [$\bar{2}$33] and [01$\bar{1}$]. Note the large negative magnetoresistance in the [01$\bar{1}$] direction. The measurement temperature was 1.7 K.

the surface position:

$$< \Delta(\vec{r}) \cdot \Delta(\vec{r'}) >= \Delta^2 \exp\left(\frac{\left|\vec{r} - \vec{r'}\right|}{\Lambda^2}\right), \tag{4.6}$$

where $\Delta(\vec{r})$ is the average displacement of the surface height at position $\vec{r}$ and Λ represents the lateral decay rate of the fluctuations at the interface. However, the calculation of the anisotropic interface scattering is defined by three parameters: the amplitude of the roughness Δ, and the correlation lengths (Λ_x and Λ_y) in the [01$\bar{1}$] and [$\bar{2}$33] directions, respectively. Applying a Gaussian form of correlation (equation 4.6) of the interface roughness in

both directions one obtains

$$< \Delta(\vec{r}) \cdot \Delta(\vec{r'}) >= \Delta^2 \exp\left(\frac{(x-x')^2}{\Lambda_x^2} + \frac{(y-y')^2}{\Lambda_y^2}\right), \tag{4.7}$$

where Λ_x and Λ_y are the range of the spatial variation in the x- and y-directions. A typical calculation, made by Dr. A. Kurobe is shown in figure 4.7(b). Both the life-times and the anisotropy are comparable to our experimental results. The values of the life-time at low carrier densities are determined by the number of remote ionized impurities in the AlGaAs region, since this is an unknown parameter a minor discrepancy can exist between the calculated and measured life-times. The individual contributions to the total scattering time due to remote ionized impurities and interface roughness scattering are shown in figure 4.7(b). Figure 4.7(a) shows detail of experimental transport life-times of a typical (311)B 2DEG of sample T94, where the carrier density is changed with a front gate.

In comparing the experimental and theoretical results we see that there is some discrepancy in life-times for carrier densities in the region of 3 to 4×10^{11} cm^{-2}. In the theoretical model it is assumed that below a pinch-off bias there are no electrons in the system; with increasing gate voltage electrons enter the channel GaAs quantum well and the density increases almost linearly with gate voltage, V_g, according to $en_s = C(V_g - V_{th})$, where C is capacitance and V_{th} is the threshold voltage. In the real system, however, the carrier density tends to saturate as electrons either neutralize donors in the AlGaAs barrier or enter the AlGaAs as free electrons [16]. Thus the experimental life-time increases in this region more rapidly than the theory predicts.

We have tried various sizes of scattering correlations, including one corresponding to a corrugated surface reported by Nötzel *et al.* [7]. In figure 4.7(a), it can be assumed that at high carrier density ($\sim 5 \times 10^{11}$ cm^{-2}) the life-times are dominated by interface roughness scattering. Using the ratio of the experimental life-times at high carrier density, a best fit to the

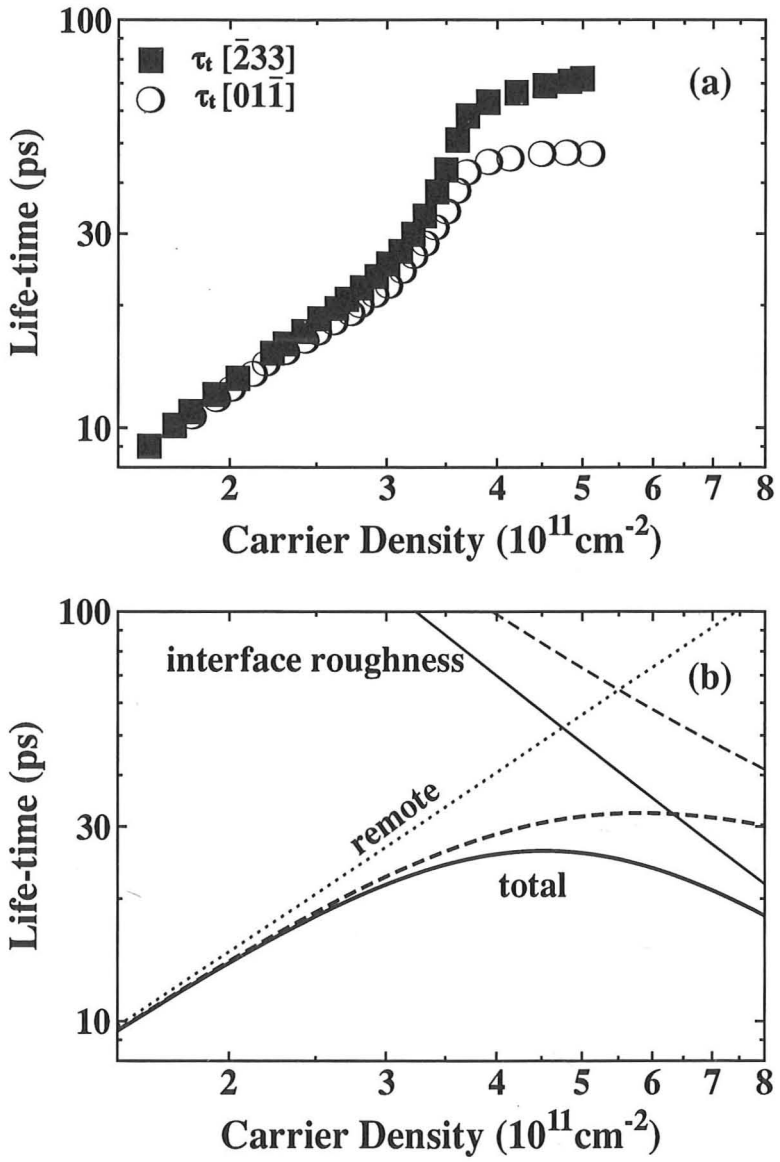

Figure 4.7: (a) The experimental transport life-times for sample T 94 in the [$\bar{2}33$] and [$01\bar{1}$] directions. (b) Calculated values of transport life-times as a function of carrier density. It has been assumed that the form of the interface roughness scattering enables an anisotropy to be observed which increases with carrier density. The model parameters for this calculation are scattering correlation lengths of 13 × 61 Å and height 2.6 Å.

models three parameters has been obtained using the calculation of the interface roughness function (see equation A.20). The anisotropic correlation lengths have been calculated to be 13 Å in the $[01\bar{1}]$ direction and 61 Å in the $[\bar{2}33]$ direction, with an amplitude of 2.6 Å. Neglecting any discrepancy due to remote ionized scattering, a reasonable approximation at high densities, the fit is quite reasonable. If these dimensions are compared with the corrugations that Nötzel *et al.* observed (see figure 4.2), then our calculated amplitude is $\sim 1/4$ of theirs and their period is about twice as large. We could surmise that rather than scattering from corrugations of height 10.2 Å and period 32 Å the corrugated surfaces is actually due to terracing and electrons scatter from the terraces that have a step size of one monolayer (2.6 Å) and lengths of the order 10.2 Å. The correlation length of 61 Å in the $[\bar{2}33]$ direction is not unreasonable for the length of a linear part of a terrace on the substrate surface. It is clear from the model, however, that the scattering has not arisen from corrugated surfaces of height 10.2 Å and period 32 Å.

Whilst interface roughness scattering describes the mobility anisotropy as a function of carrier density fairly well, it should be noted that in the momentum relaxation time approximation, in which our calculations are performed, the theory simply produces two different scattering times for the $[01\bar{1}]$ and $[\bar{2}33]$ directions. These determine the mobility through the empirical relation $\mu = e\tau/m^*$. However, when these life-times are substituted into the conductivity tensor, both σ_{xx} and σ_{xy} are changed and no magnetoresistance is predicted: contrary to experimental observation. So although interface roughness scattering can, at least within the relaxation time approximation, explain mobility anisotropy the cause of the negative magnetoresistance is not a result of an anisotropic scattering mechanism. The physical mechanism giving rise to the observed negative magnetoresistance will be discussed in appendix B.

4.5 Background of electron focusing effect

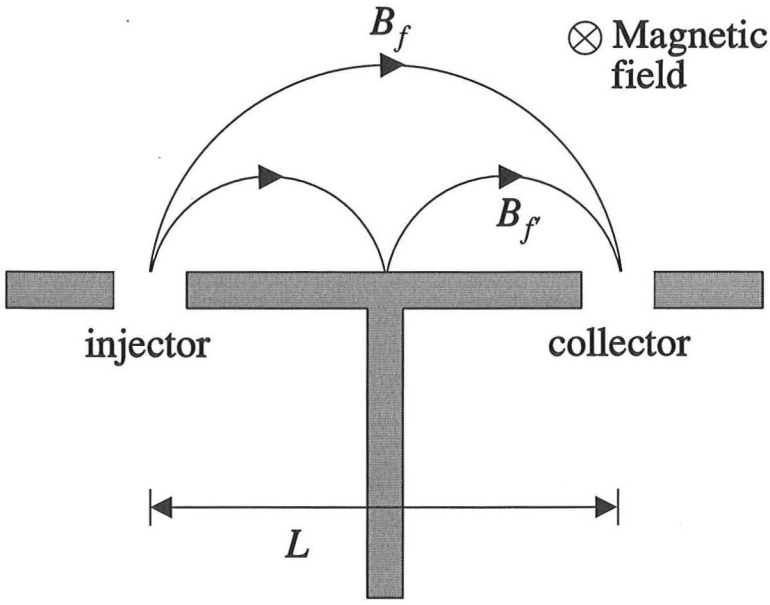

Figure 4.8: Schematic transverse electron focusing arrangement. Trajectories leaving the injector are focused into the collecting constriction channel.

The device geometry for the focusing experiments is shown in figure 4.8. Transverse magnetic focusing is achieved by measuring the current passing between two narrow openings, the injector and collector, separated by a distance (L) as a function of perpendicular magnetic field (B). Peaks in the collector current are observed when the separation length between the injector and collector probe is equal to an integer multiple n of the cyclotron diameter of the injected electrons:

$$B_f = n\frac{2\hbar k_F}{eL} \quad n = 1, 2, \cdots, \tag{4.8}$$

where $k_F = (2\pi n_s)^{1/2}$ and B_f are the Fermi wave vector and focusing magnetic field, respectively. Peaks with $n \geq 2$ arise from those electrons reflected at the sample boundary $n - 1$ times.

Transport between the injector and collector openings [one-dimensional (1D) channels] must be ballistic rather than diffusive requiring that: (i) their

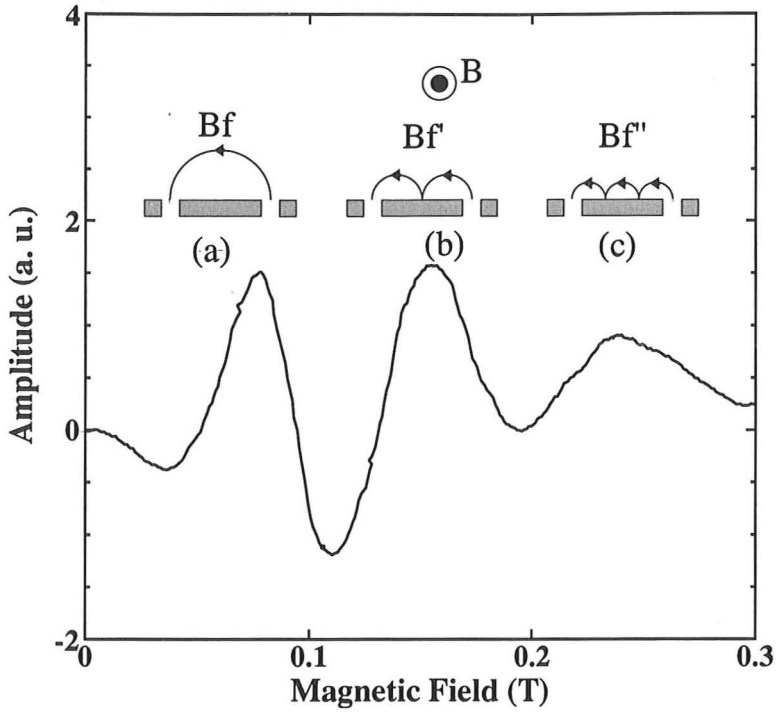

Figure 4.9: Focusing in a 2D electron gas. The position of each of the focusing peaks are compared with orbits (a), (b), and (c). Magnetic focusing of electron occurs for positive magnetic field only.

separation (L) is less than the ballistic length in the two-dimensional (2D) system and (ii) that the constriction lengths are smaller than the effective ballistic length in 1D [17]. The mean free path for a high mobility 2DEG (T104) is typically between 1.3 and 16.5 μm at densities 1.5×10^{11} and 4.5×10^{11} cm^{-2}. Therefore at a density of 2.5×10^{11} cm^{-2} the mean free path (~ 3.5 μm) is larger than both the 1D channel lengths (typically ≤ 1 μm) and the constriction separation (typically 2 μm). A classical picture (figure 4.8) is therefore a good description of the well defined, equidistant at $B_f, B_{f'} \cdots$ peaks seen experimentally. In transverse electron focusing experiments, the collector current is measured as a function of the magnetic field. Typical data is illustrated in figure 4.9 for a device with $L = 2$ μm and a carrier density of 2.5×10^{11} cm^{-2} (mean free path ~ 3.5 μm). A clear focusing

peak is seen at the expected B_f (inset a) of 0.08 T. In insets (b) and (c), the trajectories of the second and third peaks at $B_{f'} = 0.16$ T and $B_{f''} = 0.24$ T involve two and three skipping orbits, respectively.

4.6 Device fabrication and pattern design

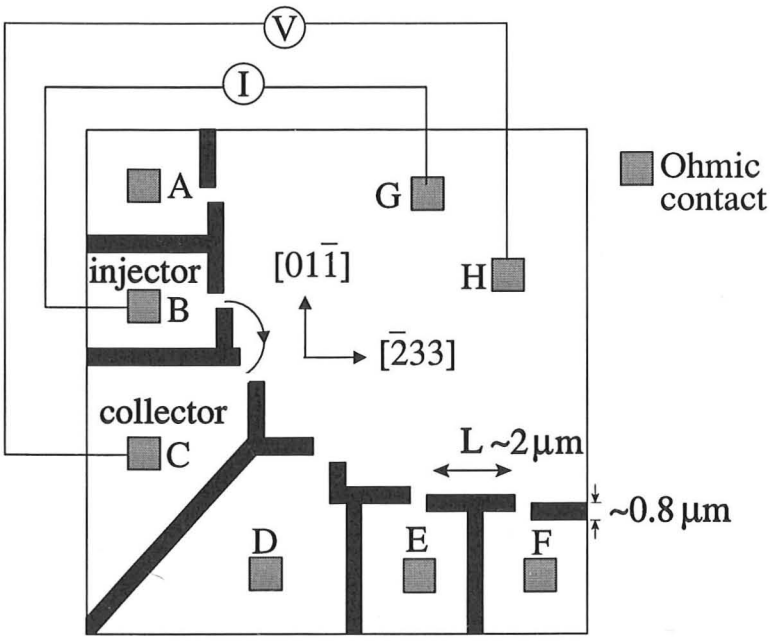

Figure 4.10: A schematic representation of the device showing lithographically defined constrictions (the solid regions) and ohmic contacts A-H for current and voltage probes. Electron orbits are interacted for two different measurement angles.

Figure 4.10 shows a schematic diagram of the device fabricated on a (311)B wafer containing a single heterojunction. The solid black regions were patterned using standard electron beam lithographic techniques and subsequently etched with a $H_2SO_4 : H_2O_2 : H_2O$ mixture to a depth of about 700 Å thus defining a number of narrow constrictions of about 0.8 μm in width and 2 μm separation. Alloyed AuGeNi ohmic pads made electrical

contacts to the 2DEG allowing resistance measurements to be performed.

The array of constructions is designed to allow the electron orbit to be analyzed as a function of angle between the $[01\bar{1}]$ and $[\bar{2}33]$ directions. The magnetic field is applied in order to direct a ballistic cone of electrons from an emitter to a collector. If the Fermi surface is warped in any way, due to a modification of the band structure, then the classical cyclotron orbit will no longer be a normal circular orbit typical of an isotropic system. The device design allows us to measure the diameter of the cyclotron orbit for a given magnetic field at five different cross sections.

4.7 Experimental determination of the Fermi surface

Electron focusing has been used quite extensively to determine the shape of the Fermi surface. While originally used for metals [18], the idea has been transferred to the study of surface scattering [19, 20] and electron-phonon interaction [21]. Magnetic focusing of two-dimensional electrons at low magnetic fields was first studied in semiconductor heterostructures by van Houten *et al.* [22]. More recently Heremans *et al.* [23], from their results for transverse hole focusing, suggested that an anisotropic mobility in (311)A GaAs two dimensional hole gases could be explained by a warped Fermi surface that gives rise to a directional dependence of hole wave-vector magnitude and corresponding effective mass.

Figure 4.11 shows transverse magnetic focusing spectra, plotted as the collector voltage normalized by injector current versus magnetic field. The experiment was carried out at 1.7 K, sufficiently high such that quantum interference effects can be ignored, and the sample was illuminated prior to measurement. The first oscillation corresponds to a magnetic field B_f, at which the electron wave vector is $\vec{k} = \pi B_f e\vec{L}/h$ and $\vec{L}$ is the vector length

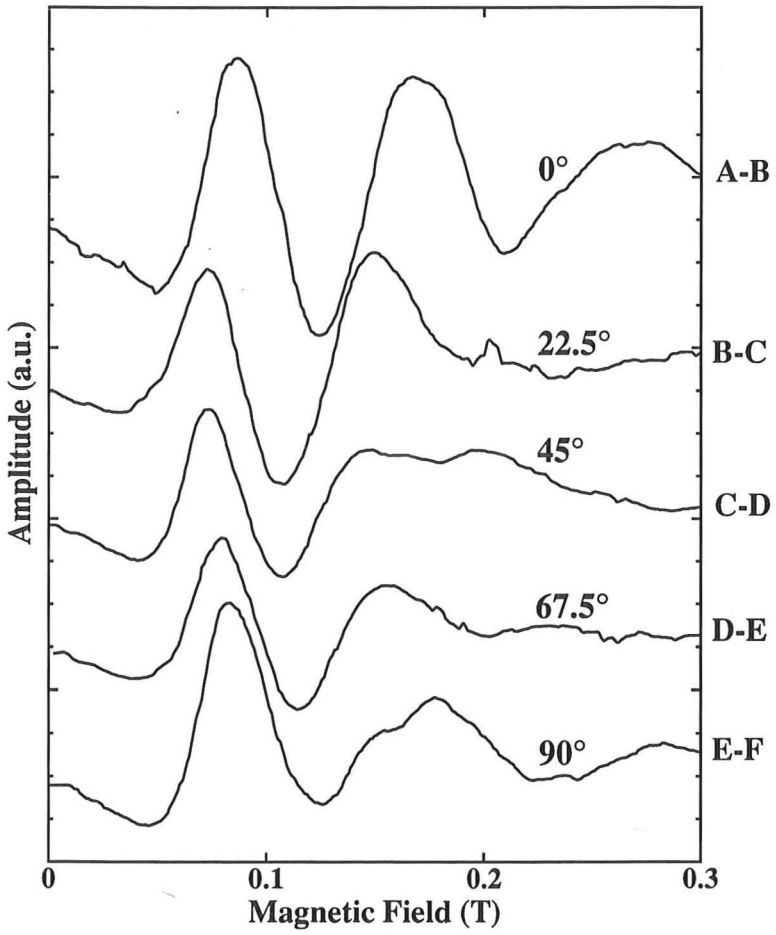

Figure 4.11: The transport magnetic focusing for different orientation of the focusing barrier for sample T104a.

between the two constrictions. In a semiclassical model, the electrons trajectory in k-space coincides with the constant energy contour in the magnetic field. The further oscillations at higher fields correspond to multiple skipping orbits along the edge of the lithographic region between the constrictions, where $\vec{k} = n\pi Be\vec{L}/h$, for $n = 2, 3, ..., \infty$. Unfortunately, some of the second and third peaks are not clearly seen because the designed focusing barriers are not flat (for example between B and C in figure 4.10). However, first peak is well defined and has been measured on two samples from the same wafer. At higher fields, SdH oscillations are observed from which the carrier

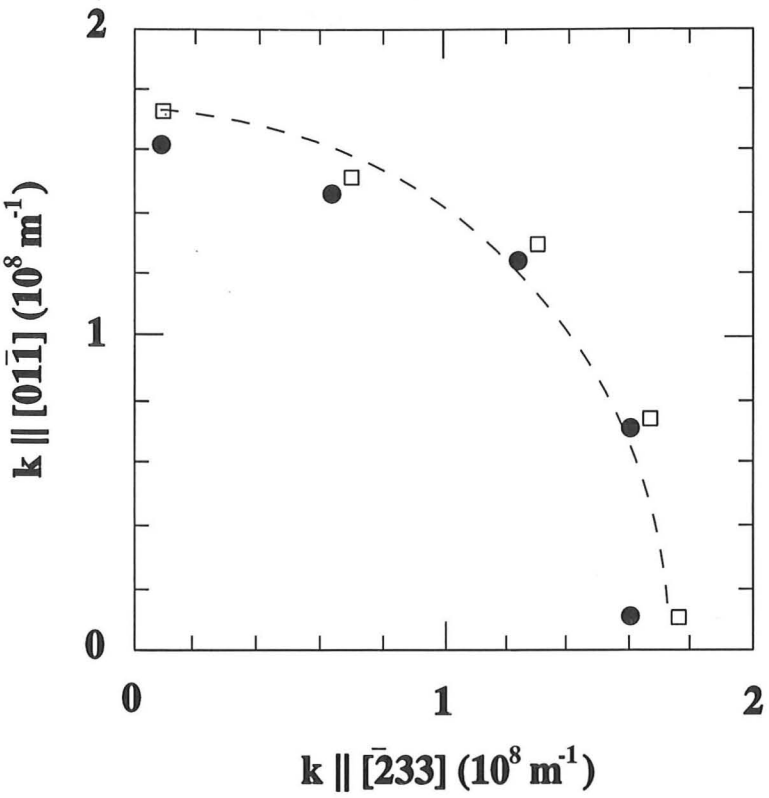

Figure 4.12: Values of the electron wave vector are plotted as a function of different measurement angles for two different samples T104a (solid circles) and T104b (open squares). A circle is plotted to demonstrate that the Fermi surface is isotropic.

density was determined to be 4.5×10^{11} cm^{-2} in both samples. Figure 4.12 shows a plot of $\vec{k}$ as a function of angle for each sample: the values of $\vec{k}$ are obtained from a polar plot of the first peak in figure 4.11 for each of the different injector/collector orientations. From section 4.3, higher mobilities are found in the [$\bar{2}$33] direction than in the [01$\bar{1}$] direction and using two orthogonal Hall bars Hall and resistivity measurements yield mobilities of 1.04×10^6 and 1.43×10^6 cm^2/Vs for [01$\bar{1}$] and [$\bar{2}$33] directions, respectively at the same carrier density. It can be seen that, within experimental error, the electron wave vector $\mid \vec{k} \mid$ lies on a circle. This can be compared to

the results of Heremans *at al.* [23], which showed an elliptical contour for hole wave vectors. Heremans *at al.* explained their results by introducing an anisotropic effective mass induced by a periodic modulation in the band structure, which they surmised could be due to surface corrugations on the (311) substrate which have been reported elsewhere [7]. This would explain the anisotropic wave-vector contour and mobilities $\mu = e\tau_t/m^*$. However, we observed an anisotropy in the mobility but not in the effective electron mass. This confirms our earlier prediction that the anisotropic mobility is caused purely through a scattering time (or transport time) τ_t and not an effective mass m^*. This conclusion is also in agreement with the work of Simmons *at al.* [24] on (311)A hole gas hetrojunctions.

4.8 Experimental determination of ballistic length

Electron focusing experiments have been used by Spector *et al.* [25] to study scattering processes for ballistic length in a 2DEG. We have employed their technique to determine the electron ballistic length in our samples. The device used is shown in figure 4.10 and was arranged such that electrons were emitted from a constriction (A) at one end of the device and collected in one of the other constrictions (B-F). Figure 4.13 shows experimental data of the measured focusing voltage as a function of magnetic field with path length L' from 3.9 to 13.1 μm: the path length over which electrons propagate before hitting a collector is equal to the arc length of each orbit. This can be calculated from the geometry of the pattern. Consequently, the ballistic length of the electrons can be determined according to the path lengths successfully traversed.

The amplitude of the focused electron spectra L', as a function of length, results in a length scale that is related to the ballistic length of the electrons. Figure 4.14 shows a plot of electron-focus peak amplitude as a function of path length. Two samples from the same wafer T104 have been used. It can

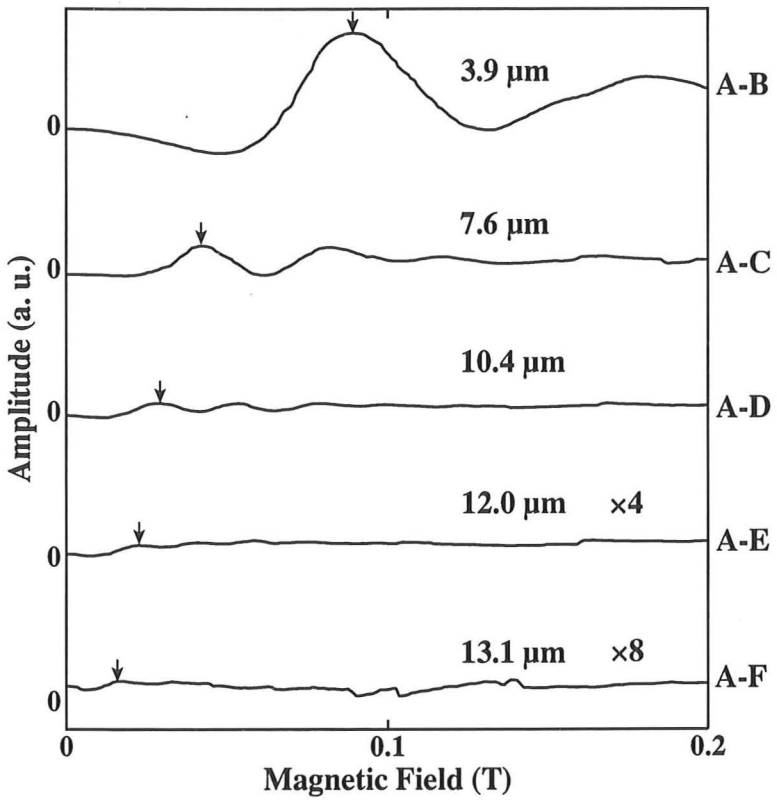

Figure 4.13: Experimental electron focusing spectra at 1.7 K for five different injector-collector separations.

be seen that the peak amplitude has a functional form of $\exp(-L'/L_0)$, where L_0 is the ballistic length and is determined to be between 2.2 and 2.5 μm for devices A and B, respectively. The ballistic length is sample dependent and hence there is a slight variation. We noted that as the electron trajectories are parts of circular orbits, the electron will travel the same distance in both the $[01\bar{1}]$ and $[\bar{2}33]$ direction, thus the value of L_0 is an average of the two orthogonal directions. In order to investigate anisotropy of the ballistic length in orthogonal directions it would be necessary to employ an experimental technique that does not involve the use of magnetic field.

The elastic mean free path l, determined from the mobility and carrier density, has values of 10.9 μm for the $[01\bar{1}]$ direction and 15 μm for

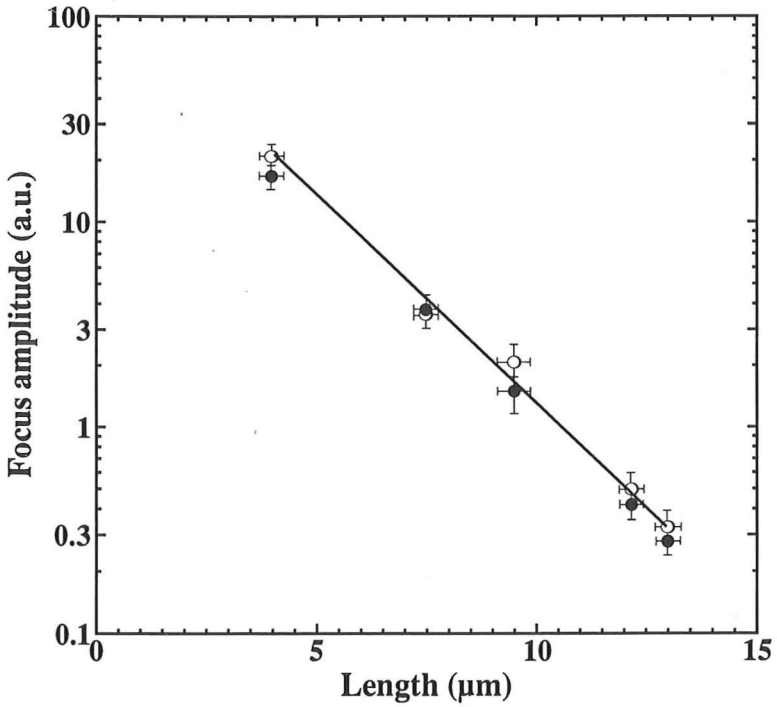

Figure 4.14: Focus amplitude for spectra of the type shown in figure 4.13 refare plotted as a function of path length (L') for two samples A and B. The current was injected between contacts A-G, and the voltage probed between H-(B, C, D, E, and F). The exponential dependence of the peak amplitude upon the path length (L') allows the ballistic length to be determined as 2.2 and 2.5 μm, for sample A and B, respectively.

the [$\bar{2}$33] direction. These values are much larger than the averaged experimental ballistic length. Spector *et al.* [25] showed that the scattering length L_0 associated with the suppression of focusing is smaller than the transport length l. They argue that this is due to the greater sensitivity of the focusing technique to forward scattering, therefore the scattering length obtained from a focusing experiment is a better estimate of the ballistic length between large-angle scattering processes. However it is likely that the ballistic length depends on different criteria, for example the inclusion of some small angle scattering processes. The coherence length calculated

from the quantum life-time τ_q, which does include small-angle scattering, is found to be 0.29 μm at a carrier density of 4.5×10^{11} cm^{-2} and a value of $\tau_q = 1$ psec (see section 4.3). Thus we see that the ballistic length lies between the mean free path and the phase coherence length.

4.9 Conclusions

We have observed anisotropic mobility and magnetoresistance that appears to be universal for electron gases grown on (311)B orientated GaAs substrates. The mobility in the $[\bar{2}33]$ direction is always high than that in the $[01\bar{1}]$ direction at higher carrier density. Although interface roughness scattering is shown to be a possible cause of the mobility anisotropy, the negative magnetoresistance associated with the anisotropy cannot, as yet, be explained using this theory.

We also described electron focusing experiments carried out on 2DEGs formed on (311)B substrates. The focusing experiments show that the effective mass is isotropic and an anisotropic transport time τ_t is inferred confirming that anisotropic scattering is the cause of the anisotropic mobility. The ballistic length for electrons in this system was determined at 1.7 K and found to be between 2.2 and 2.5 μm. This length is much shorter than the mean free path of the electrons but longer than the length scale derived from the quantum life-time.

Bibliography

[1] A. C. Churchill, G. H. Kim, A. Kurobe, M. Y. Simmons, D. A. Ritchie, M. Pepper, and G. A. C. Jones, J. Phys.: Condens. Matter **6**, 6131 (1994).

[2] A. C. Churchill, G. H. Kim, M. Y. Simmons, D. A. Ritchie, and G. A. C. Jones, Phys. Rev. B **50**, 17636 (1994).

[3] M. Y. Simmons, A. C. Churchill, G. H. Kim, A. R. Hamilton, A. Kurobe, D. R. Mace, D. A. Ritchie, and M. Pepper, Microelectronics Journal **26**, 897 (1995).

[4] W. I. Wang, E. E. Mendez, T. S. Kuan, and L. Esaki, Appl. Phys. Lett. **47**, (8) 826 (1985).

[5] R. Nözel, N. N. Ledenstov, L. Daweritz, M. Hohenstein, and K. Ploog, Phys. Rev. B **45**, 3507 (1992).

[6] L. Daweritz, J. of Cryst. Growth **127**, 949 (1993)

[7] R. Nözel, N. N. Ledenstov, L. Daweritz, M. Hohenstein, and K. Ploog, Phys. Rev. Lett. **67**, 3812 (1991).

[8] S. Das Sarama and F. Stern, Phys. Rev. B **32**, 8442 (1985).

[9] A. Gold, Phys. Rev. B **38**, 10798 (1988).

[10] P. T. Coleridge, R. Stoner, and R. Fletcher Phys. Rev. B **39**, 1120 (1989).

[11] A. Kurobe, Semicond. Sci. Technol. **8**, 742 (1993).

[12] S. Das Sarama and B. Vinter, Phys. Rev. B **24**, 549 (1981).

[13] T. Ando, J. Phys. Soc. Japan **51**, 3215 (1982).

[14] P. Harrang, R. J. Higgins, R. K. Goodall, P. R. Jay, M. Laviron, and P. Delescluse, Phys. Rev. B **32**, 8126 (1985).

[15] T. Ando, A. B. Fowler. and F. Stern, Rev. Mod. Phys. **54**, 437 (1982).

[16] B. Vinter, Appl. Phys. Lett. **44**, 307 (1984).

[17] C. W. J. Beenakker and H. van Houten, Solid State Phys. **44**, 1 (1991).

[18] Yu. V. Sharin, Zh. Eksp, Teor. Fiz. **48**, 984 (1965). [Sov. Phys. JETP Lett. **21**, 655 (1965)].

[19] V. S. Tsoi, Zh. Eksp, Teor. Fiz. **19**, 114 (1974). [JETP Lett. **19**, 70 (1974)].

[20] V. S. Tsoi and X. Razgonov, Zh. Eksp, Teor. Fiz. **74**, 1137 (1978) [JETP Lett. **47**, 597 (1978)].

[21] P. C. van Son, H. van Kempen, and P. Wyder, Phys. Rev. Lett. **58**, 1567 (1989).

[22] H. van Houten, C. W. J. Beenakker, J. G. Williamson, M. E. I. Broekaart, P. H. M. van Loosdrecht, B. J. van Wees, J. E. Mooij, C. T. Foxon, and J. J. Harris, Europhys. Lett. **5**, 721 (1988); Phys. Rev. B **39**, 8556 (1989).

[23] J. J. Heremans, M. B. Santos, and M. Shayegan, Surf. Sci. **305**, 348 (1994).

[24] M. Y. Simmons, A. R. Hamilton, S. J. Stevens, D. A. Ritchie, M. Pepper, and A. Kurobe, Appl. Phys. Lett. **70**, 2750 (1997).

[25] J. Spector, H. L. Stormer, K. W. Baldwin, L. N. Pfeiffer, and K. W. West, Appl. Phys. Lett. **56**, 1290 (1990).

Chapter 5

Transport Properties of 2DEGs Containing InAs Dashes

5.1 Introduction

In this chapter we study the magnetotransport properties of AlGaAs-GaAs heterostructures in which a number of InAs monolayers (MLs) have been inserted in the centre of a GaAs quantum well. The sample structures are characterised by transmission electron microscopy (TEM) and atomic force microscopy (AFM) in section 5.2. In section 5.3 we present the results of transport measurements to show the relation between the mobility and carrier density. In sections 5.4 and 5.5 we plot the phase diagram of the localisation-delocalisation transitions in the quantum Hall effect. Section 5.6 presents activation energy data obtained from Arrhenius plots at $\nu = 1$, showing the collapse of spin-splitting.

5.2 Device structure

The samples used in this study were grown on undoped GaAs(100) substrates. The structure consists of a 0.6 μm thick undoped GaAs buffer layer grown at a substrate temperature of 580°C (as measured by an optical pyrometer), followed by a 500 Å undoped $Al_{0.33}Ga_{0.67}As$ barrier, a 200 Å undoped GaAs quantum well, a 400 Å undoped $Al_{0.33}Ga_{0.67}As$ spacer layer, a 400 Å Si-doped (1×10^{18} cm^{-3}) $Al_{0.33}Ga_{0.67}As$ layer, and finally a 170 Å GaAs capping layer. Figure 5.1 shows the cross-sectional TEM image of a sample with 2.79 MLs of InAs.

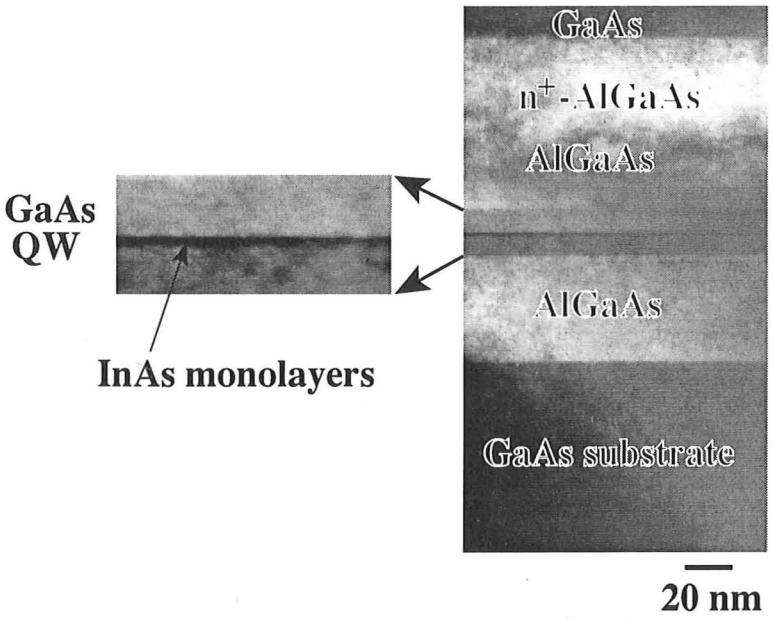

Figure 5.1: A cross-sectional TEM image of a heterostructure with 2.79 MLs of InAs (sample C1105) in the GaAs quantum well (QW).

Within the GaAs quantum well an InAs layer was inserted with a coverage of either 0.54, 1.07, 1.61, 2.15 or 2.79 MLs. The InAs layers and the 10 Å GaAs cap were grown at a substrate temperature of 530°C. A reference sample was also grown that had no InAs layer. The wafers were processed into a patterned Hall bar geometry with length 800 μm and width 80 μm.

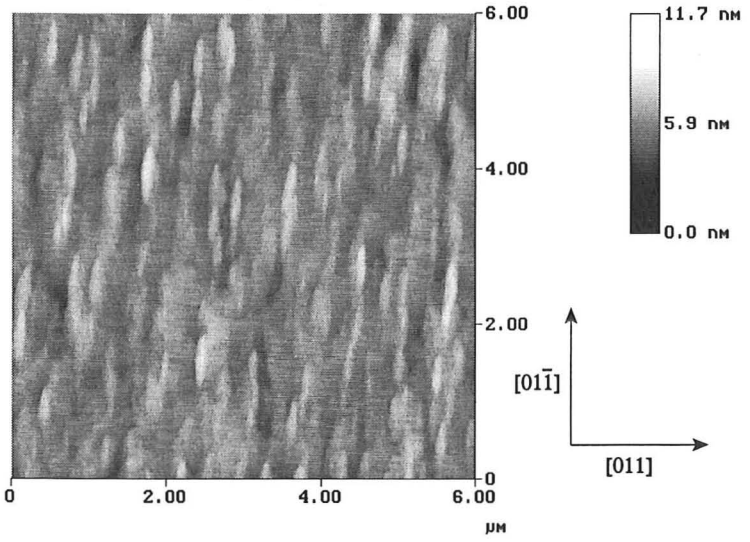

Figure 5.2: An AFM image of InAs dashes formed with 2.15 MLs coverage of InAs grown on GaAs (sample C1330).

The surface morphology of the InAs on (100)GaAs was characterised by AFM. Figure 5.2 shows a 6 μm $\times$ 6 μm AFM image of surface with 2.15 MLs InAs. This surface was grown under the same conditions as the transport device and had a 10 Å GaAs cap. The anisotropy of the cigar-shaped InAs islands is such that they from elongated 'dashes' that are about 8 times larger in the [01$\bar{1}$] direction than the [011] direction. Such characteristics have been reported using InGaAs islands grown on (100)GaAs substrate by Tillmann *et al.* [1] and are discussed in chapter 6.

5.3 Transport properties of InAs dashes

5.3.1 Carrier density dependence of mobility

In order to systematically study the variation in 2DEG mobility with different InAs coverages, each sample was taken from central regions of the wafer and was processed using the same technique. The InAs coverage is

Wafer	Sample	Mobility ($10^4 cm^2/Vs$)	Density ($10^{11} cm^{-2}$)	InAs coverage (ML)	α
C1127	centre	12.00	1.50	0.00	0.88
C1122	centre	8.20	1.50	0.54	0.70
C1123	centre	6.35	1.50	1.07	0.68
C1125	centre	4.95	1.50	1.61	0.66
C1126	centre	3.25	1.50	2.15	0.65
C1105	centre	1.30	1.50	2.79	0.65

Table 5.1: Sample characteristics at 1.6 K. The thickness of the GaAs layers is 10 Å grown on the InAs dashes at the temperature of 530°C.

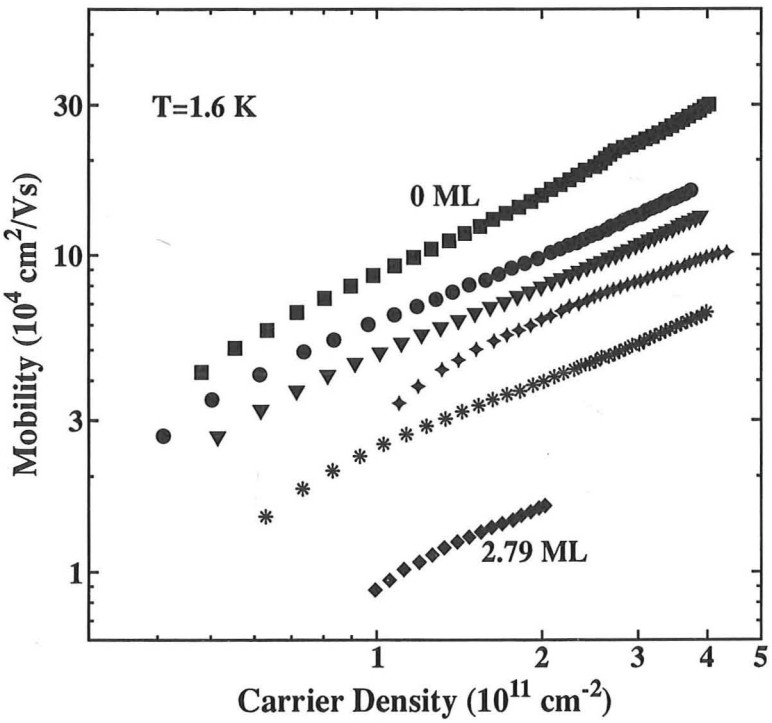

Figure 5.3: Electron mobility μ as a function of carrier density n_s at 1.6 K on a log-log scale. Estimated InAs coverage is 0, 0.54, 1.07, 2.15, 1.61, and 2.79 MLs from top to bottom.

not exactly the same in each of the samples, differing by small fractions of a monolayer. The resistivity was obtained from four-terminal resistance measurements using a constant ac current (100 nA) at 73 Hz. The mobilities and densities are summarized in table 5.1.

Figure 5.3 shows the electron mobility μ as a function of carrier density n_s for six different samples (InAs coverage from 0 to 2.79 MLs) at 1.6 K. The carrier density before illumination was varied by changing the gate voltage V_g. The relationship between the mobility and carrier density is given by $\mu \propto n^{\alpha}$, where α is a constant between 0.5 and 1.5. For typical HEMT structures, with the 2DEG formed at an GaAs-AlGaAs interface and remote modulation doping, remote ionized impurity scattering [2] is the dominant scattering mechanism at low temperatures giving $\alpha = 1.5$ [3]. The reference sample (indicated with square symbols in figure 5.3), has a small α of 0.88 which results from the increased incorporation of impurities in the GaAs due to the low growth temperature (530°C). At a constant carrier density of $1.5 \times 10^{11}\text{cm}^{-2}$ we have found that the mobility decreases from 1.2×10^5 to 1.3×10^4 cm^2/Vs as the InAs coverage is increased from 0 to 2.79 MLs. With a sample coverage of 2.79 MLs (diamond symbols in figure 5.3) the exponent has decreased to $\alpha = 0.65$. We believe that the decrease in α values with increasing InAs layer thickness is due to increased short-range scattering from the InAs islands.

5.3.2 Strong localisation

At the low carrier density end of the traces in figure 5.3 the increased dependence of μ on n_s has been attributed to strong localisation [4]. Such localisation occurs when the electrons are trapped by potential fluctuations caused by the InAs islands: the conduction band offset at the InAs-GaAs interface forms local potential minima in the 2DEG. Figure 5.4 shows the zero field resistivity as a function of gate voltage for temperatures between 200 mK

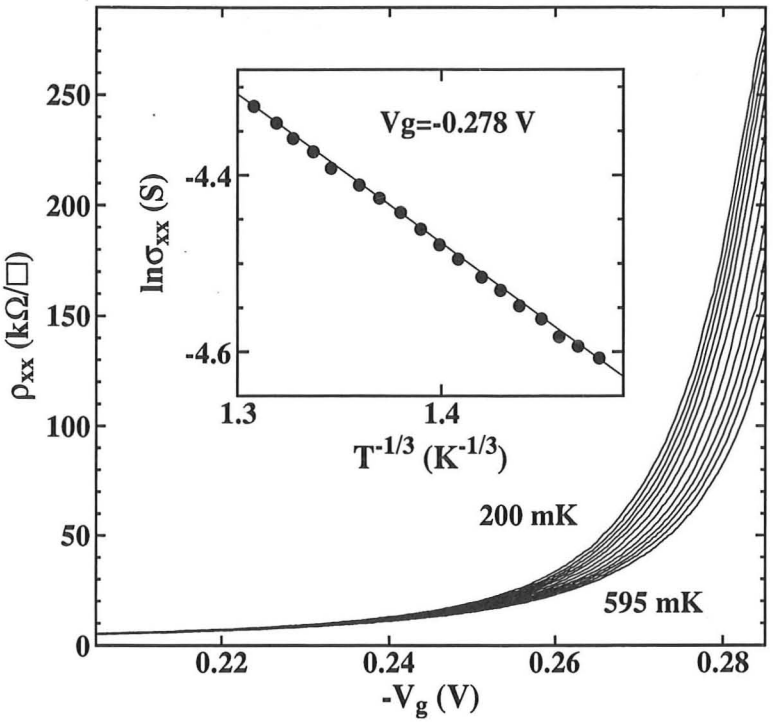

Figure 5.4: Resistivity of the 2DEG electrons as a function of gate voltage in the temperature range of 200-595 mK for sample C1125 (1.61 MLs InAs). The inset shows the logarithm of the conductivity as a function of temperature, $1/T^{1/3}$, at $V_g = -0.278$ V.

and 595 mK for sample from wafer C1125 (coverage of 1.61 MLs). Four-terminal measurements were carried out at the base temperature (20 mK) of a dilution refrigerator using a constant ac current of 2 nA at a frequency of 13.4 Hz. The samples were briefly illuminated prior to measurement. For $V_g > -0.24$ V the carrier density is high enough such that the localisation of electrons is not significant; this is seen the 2DEG resistivity which is almost temperature independent, indicative of metallic behaviour. As the carrier density is reduced with a more negative gate bias the localised character of the electrons dominates and the resistivity increases rapidly. The resistivity is seen to diverge exponentially as $T \to 0$, reaching measured values as high

as 280 kΩ/□ at the lowest temperatures. The inset to figure 5.4 shows the conductivity as a function of temperature at a bias of $V_g = -0.278$ V. At these low temperatures, the conductivity is well described by Mott's law [5] $\sigma_{xx} \sim \exp(-T_0/T)^{1/3}$, describing hopping conduction in a strongly disordered regime. Applying this relation, the localisation length ξ can be determined through $\xi = (3/k_B T_0 \rho)^{1/2}$ where ρ is the electron density of states at the Fermi energy. At $V_g = -0.278$ V, ξ is approximately 2700 Å. This length is much smaller than the sample size, therefore the behaviour is that of an insulator. Additionally the localisation length has been observed to decrease as the effective disorder is increased (reduced densities).

5.4 Delocalised states of Landau levels

Figure 5.5 shows plots of the longitudinal conductivities σ_{xx} and σ_{xy} as a function of gate voltage (carrier density). These data have been calculated from ρ_{xx} and ρ_{xy} for sample C1122 at a temperature of 100 mK. We convert from resistivity to conductivity using the standard matrix conversions,

$$\sigma_{xx} = \frac{\rho_{xx}}{\rho_{xx}^2 + \rho_{xy}^2} \text{ and } \sigma_{xy} = \frac{\rho_{xy}}{\rho_{xx}^2 + \rho_{xy}^2}. \tag{5.1}$$

In a finite magnetic field, the integer quantum Hall state is characterised by a quantized Hall conductivity $\sigma_{xy} = ie^2/h$ where $i = 1, 2, 3, \cdots$, when the Fermi energy E_F lies in localised states. The peaks in σ_{xx} occur when E_F lie in delocalised states [6]. Changing the electron density at a fixed magnetic field of 0.8 T [figure 5.5(a)], 1.2 T [figure 5.5(b)], and 2.2 T [figure 5.5(c)], sweeps the Fermi energy E_F through the localised and delocalised states. The carrier density was calculated from the low field Hall slope, and had a linear dependence upon gate voltage, as expected for a capacitive gate. For the lowest magnetic field $B = 0.8$ T, spin-degenerate Landau levels were observed, see figure 5.5(a) and only even $\nu = 2, 4, 6 \cdots$ filling factor seen. Figure 5.5(b) shows both cyclotron (even filling factors) and spin-split

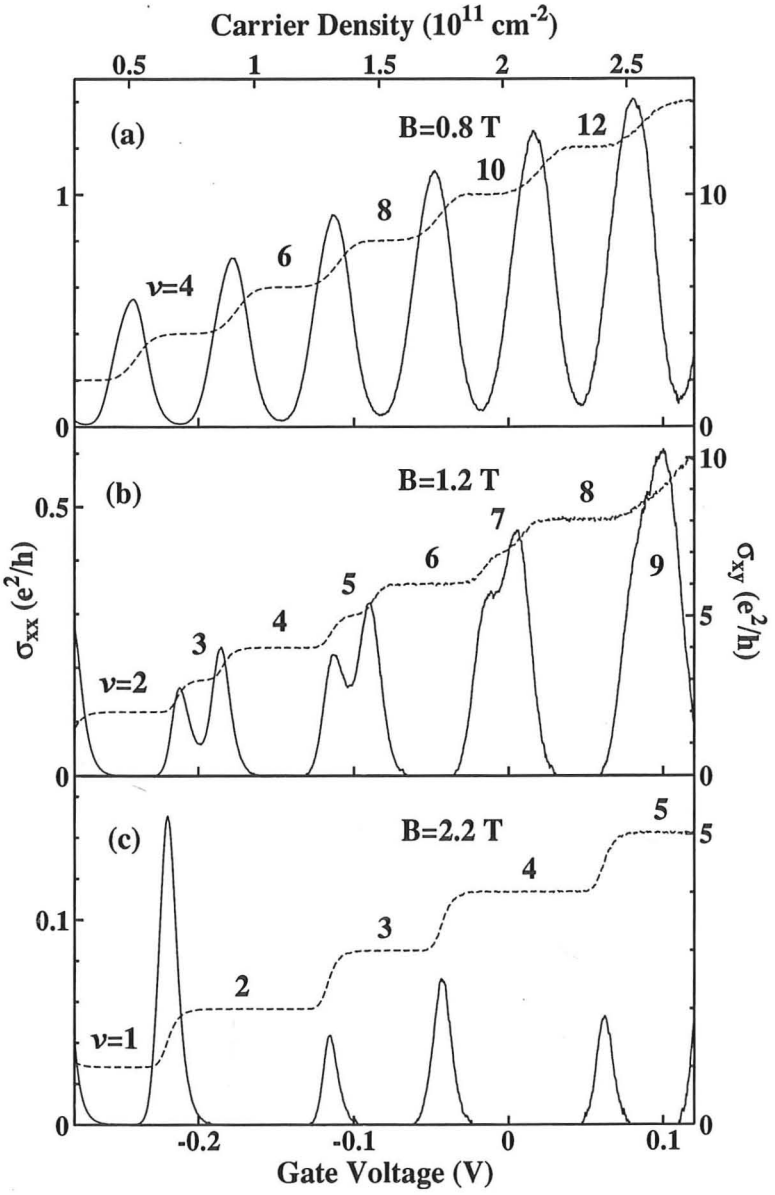

Figure 5.5: σ_{xx} (solid lines) and σ_{xy} (dashed lines) as a function of gate voltage calculated by matrix inversion from the measured ρ_{xx} and ρ_{xy} at $T = 100$ mK.

(odd filling factor) Landau levels. As the carrier density is increased, the energy of the spin ΔE_s states within a Landau level shrinks. As the gap decreases the odd ν minima plateaus are suppressed until finally the spin-split Landau levels at $\nu = 9$ can no longer be resolved. Similar behaviour of the density dependence of the spin gap has been reported by several groups using GaAs [7, 8] and InAs [9]. By increasing the magnetic field to 2.2 T in figure 5.5(c), the spin-splitting has increased such that it is nearly half the cyclotron-splitting.

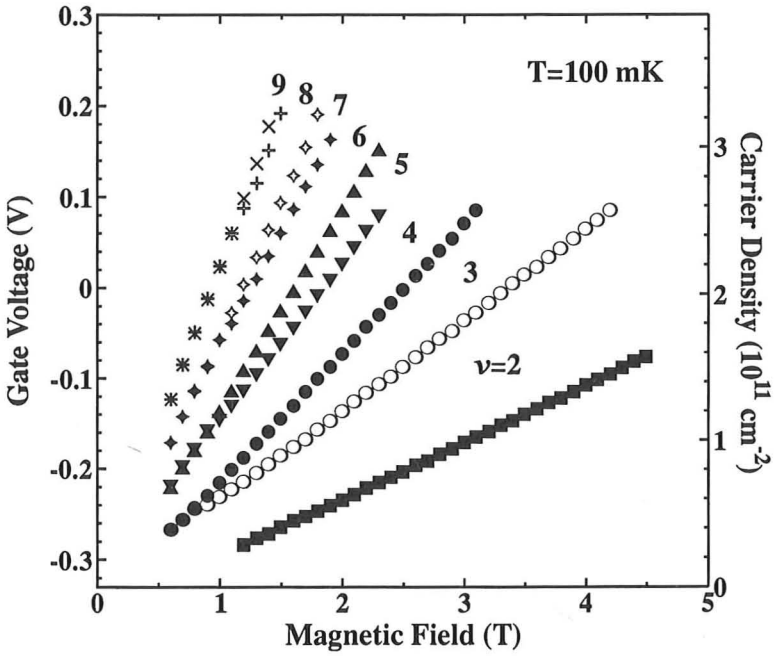

Figure 5.6: Gate voltage position of the conductance maxima as a function of magnetic field for a sample C1122 at T=100 mK.

Figure 5.6 shows the positions of the delocalised states as function of gate voltage (carrier density) and magnetic field. Each data point is the position of a peak in $\sigma_{x\dot{x}}$ (see figure 5.5). The gap between odd filling factors $\nu = 3$, 5, 7, and 9 collapses as the carrier density is increased and the magnetic field is reduced. Therefore, the spin-resolved integer quantum Hall effect disappears rapidly in decreasing magnetic field as well as increasing disorder. We will

discuss in more detail the collapse of the spin-splitting at filling factor $\nu = 1$ in section 5.6.

5.5 Experimental phase diagrams

It is well known there are delocalised (extended) states at the centre of each Landau level in a two-dimensional system in a strong perpendicular magnetic field. However, in zero magnetic field, all of the states in a two-dimensional system are believed to be localised [10]; implying that there are no delocalised states below the Fermi energy. Khmelnitskii [11] and Laughlin [12] resolved this paradox by suggesting that the delocalised states do not disappear discontinuously, but instead 'float up' in energy above the Fermi level as $B \rightarrow 0$. This interpretation is problematic as conventionally 2DEGs do not exhibit insulating behaviour at $B = 0$, but are only weakly localised.

Building on this picture of floating up a theoretical global phase diagram for the quantum Hall effect was proposed by Kivelson, Lee, and Zhang [13]. In early studies of magnetic field induced transitions a number of groups [14, 15, 16] observed a transition from an insulating state to the spin-degenerate $\rho_{xy} = h/2e^2$ quantum Hall liquid. However in a later study Shahar *et al.* [18] used high mobility samples at very low carrier densities to observe transitions from the insulating phase, through the spin-degenerate $\rho_{xy} = h/2e^2$ phase into the spin-polarised $\rho_{xy} = h/e^2$ state. More recently Nihey *et al.* [19] have also observed spin-splitting in the quantum Hall transitions in GaAs using samples of higher carrier density; in these samples the disorder is introduced by the randomness in the position and size of antidots defined by electron beam lithography and Hilke *et al.* [20] have demonstrated transitions between low and high magnetic field insulators and the $\nu = 1$ quantum Hall state in a Ge-SiGe quantum well.

In this section, we present a study of the effect of spin up on the trans-

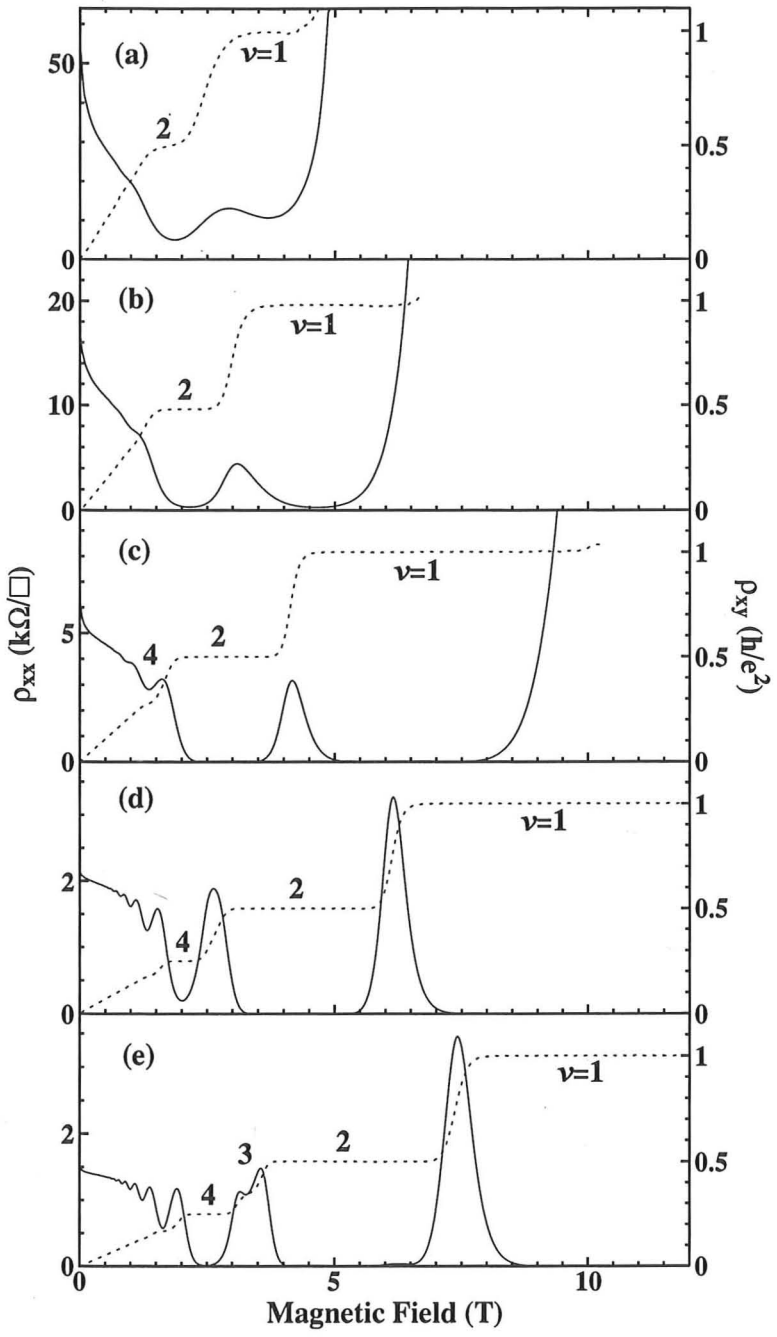

Figure 5.7: Typical ρ_{xx} (solid lines) and ρ_{xy} (dashed lines) traces as a function of magnetic field B at T=300 mK for sample C1105 shown in table 5.1. The mobilities μ = 0.35, 0.86, 1.80, 3.10, and 3.90 $\times 10^4$ cm^2/Vs, densities n_s = 0.67, 0.81, 1.10, 1.80, and 2.20 $\times 10^{11}$ cm^{-2} through (a) to (e), respectively. The numbers show the filling factors ν.

itions between insulating states and quantum Hall liquid states induced with inserted InAs islands. The low temperature mobility of samples with 2.79 MLs InAs is approximately ten times lower than that of samples with only a growth interruption and no InAs islands (see table 5.1). When the InAs islands are introduced they impose random short range potential fluctuations in the 2DEG. Compared to the reference sample with no InAs, these samples show two new effects. Firstly, at low temperatures, they exhibit insulating rather than metallic behaviour, and secondly, in a perpendicular magnetic field they show a number of different quantum Hall transitions. We have measured the temperature independent longitudinal resistivity at the localisation-delocalisation transitions between the insulating state and the $\nu = 1$ and $\nu = 2$.

Figure 5.7 shows the longitudinal (ρ_{xx}) and Hall (ρ_{xy}) resistivities as a function of magnetic field at $T = 300$ mK and $V_g = 0.025$, 0.050, 0.100, 0.200, and 0.300 V (top to bottom). At zero magnetic field, sample C1105 has carrier density $n_s = 0.67$, 0.81, 1.10, 1.80, and 2.20×10^{11} cm^{-2} and mobilities $\mu = 0.35$, 0.86, 1.80, 3.10, and 3.90×10^4 cm^2/Vs through figure 5.7(a) to (e), respectively. Here, the effective disorder increases as carrier density decreases. Despite the low carrier density in figures 5.7(a) and (b), ρ_{xy} looks conventional, with wide plateaus at spin-degenerate $\nu = 2$ and the spin-polarised $\nu = 1$ states. However, the finite ρ_{xx} minima in figures 5.7(a) and (b) are not zero resistivity at $\nu = 2$ and $\nu = 1$. In figure 5.7(c) and (d), ρ_{xx} looks metallic at $B = 0$ and develops into a quantum Hall liquid at $\nu = 6$, 4, 2, and 1. Figure 5.7(e) shows both the $\nu = 3$ and $\nu = 1$ spin-polarised states. There is no evidence of any transitions from an insulating state to a quantum Hall liquid state in this data, taken at only one temperature. An analysis of the temperature dependence of the resistivity would identify these states, whilst the resistance of an insulator increases with decreasing temperature the resistance of a quantum Hall liquid would

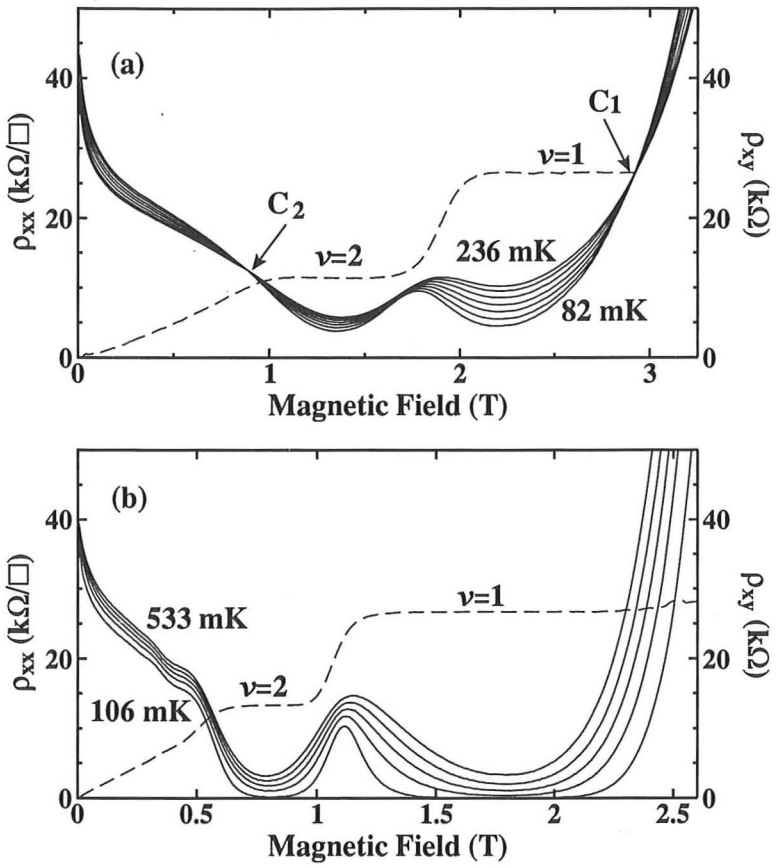

Figure 5.8: ρ_{xx} (solid lines) and ρ_{xy} (dashed lines) traces as a function of magnetic field B. (a) For device C1126 (2.15 ML InAs), the temperatures are 82, 116, 144, 168, 193, 217, and 236 mK for ρ_{xx} and 82 mK for ρ_{xy}. C_2 and C_1 are the delocalisation points. (b) For device C1122 (0.54 ML InAs), the temperatures are 106, 220, 311, 415, and 533 mK for ρ_{xx} and 106 mK for ρ_{xy}.

decrease.

Figure 5.8 shows the longitudinal resistivity as a function of magnetic field for (a) sample C1126 and (b) sample C1122, taken at various temperatures between 82 and 533 mK. The dashed lines shows the ρ_{xy} taken at 82 mK [figure 5.8(a)] and 106 mK [figure 5.8(b)]. In figure 5.8(a), we observe a magnetically induced transition from an insulating state in zero magnetic field to

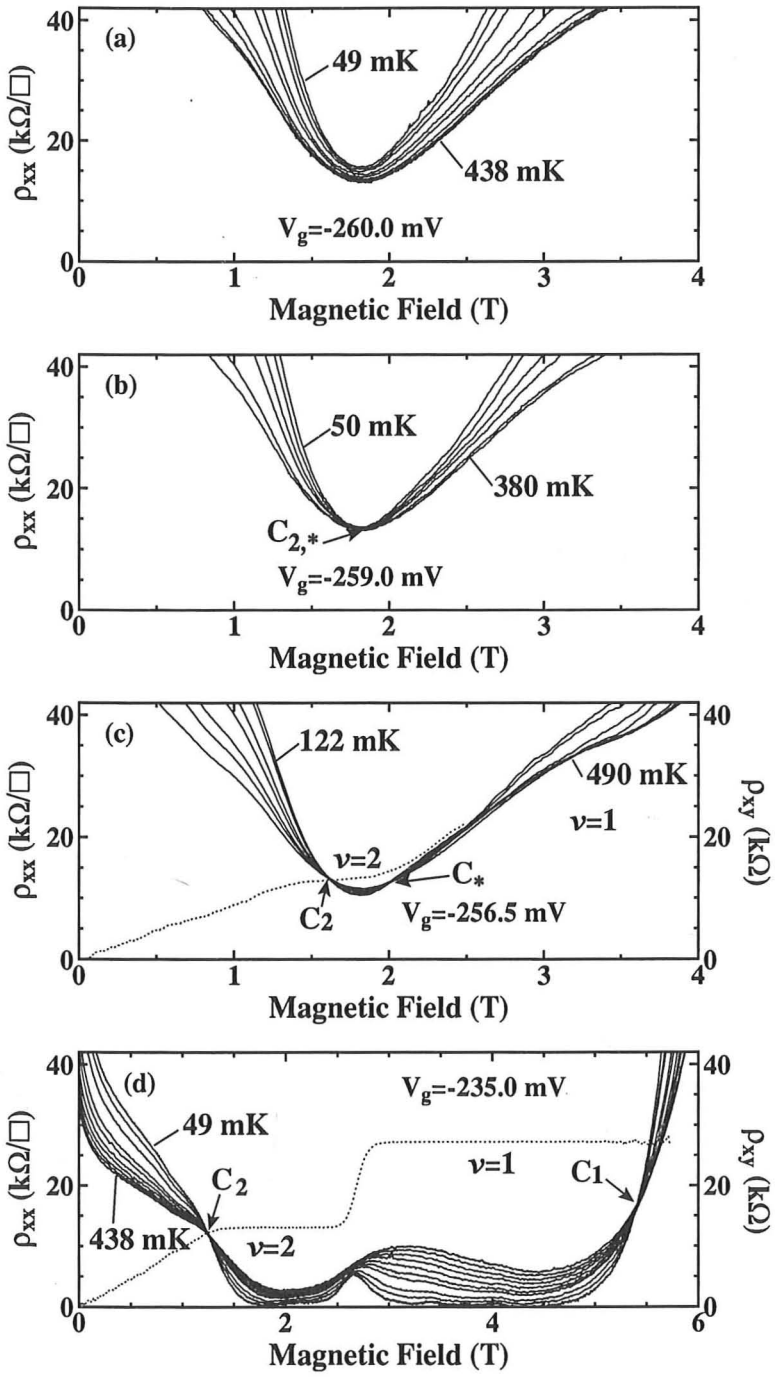

Figure 5.9: ρ_{xx} as a function of magnetic field at over temperatures 49 mK $\leq$ $T \leq$ 490 mK for the sample C1105 (2.79 MLs InAs). The dotted lines in (c) and (d) are traces of ρ_{xy} at T = 122 mK and 49 mK, respectively.

quantum Hall effect states with Hall resistance $\rho_{xy} = h/2e^2$ and $\rho_{xy} = h/e^2$ and back to an insulating state at higher field. Two magnetic fields where ρ_{xx} is independent of temperature state below C_2 and above C_1 are insulating, ρ_{xx} increasing as $T \to 0$. Similar transitions have been observed by Shahar *et al.* [18] in a high mobility sample. The region between C_2 and C_1 is a quantum Hall liquid; ρ_{xx} decreasing as $T \to 0$ and $\rho_{xy} = h/2e^2$ for $\nu = 2$ and $\rho_{xy} = h/e^2$ for $\nu = 1$. From all of the samples with InAs induced potential fluctuations we observed a transition to the spin-polarised $\nu = 1$ integer quantum Hall state. Although we observed similar phase transitions on samples with 1.61, 2.15, and 2.79 MLs InAs, upon reducing the InAs coverage below 1.07 MLs no insulator quantum Hall liquid transition is seen. In such devices it is believed that the potential fluctuations are not strong enough to localize electrons in the 2DEG.

After the first theoretical global phase diagram for the spinless phase transitions was proposed by Kivelson *et al.* [13], Fogler and Shklovskii [21] modified the global phase diagram to account for the spin-degree of freedom. The effect of the collapse of the spin-splitting on the phase diagram will be discussed in the next section. In the following we show three different types of experimental phase diagram:

(i) A transition from a zero field insulating state (0) to quantum Hall liquid state (2) with $\nu = 2$ ($\rho_{xy} = h/2e^2$) and back to an insulator. This transition is referred to as $(0 \to 2 \to 0)$.

(ii) The transition from an insulator, to the quantum Hall liquid at $\nu = 1$ and back to an insulator, $(0 \to 1 \to 0)$.

(iii) The 'camel-back' structure phase diagram with transitions $(0 \to 2 \to 0 \to 1 \to 0)$.

Figure 5.9 shows ρ_{xx} as a function of magnetic field at various temperature (49 mK $\leq T \leq$ 490 mK) for the sample C1105 (2.79 MLs InAs). In figure 5.9(a), all of the ρ_{xx} traces increase as $T \to 0$ at $V_g = -0.260$ V. This

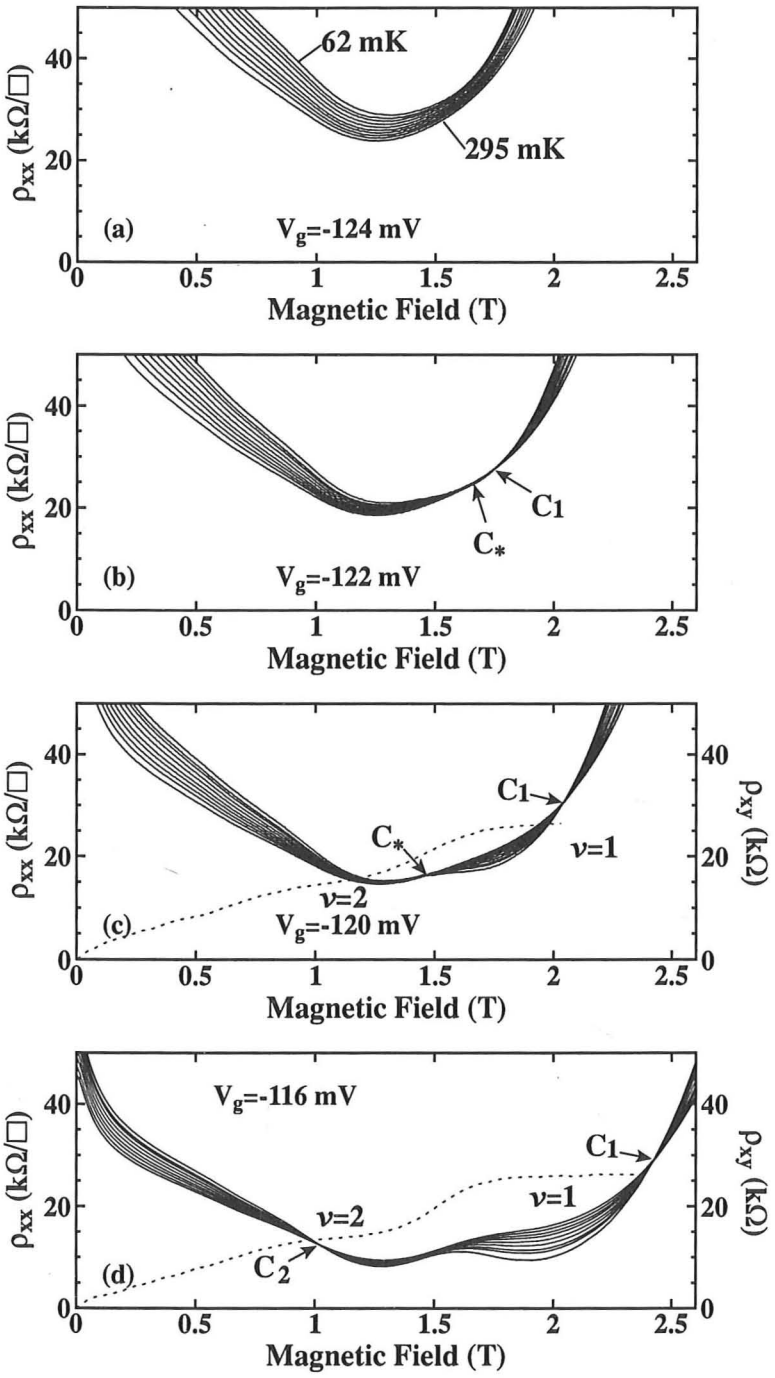

Figure 5.10: ρ_{xx} as a function of magnetic field at over temperatures 62 mK $\leq T \leq$ 295 mK for the sample C1126 (2.15 MLs InAs). The dotted lines in (c) and (d) are traces of ρ_{xy} at T = 65 mK and 123 mK, respectively.

demonstrates that all states are insulating (0) at all magnetic fields. The minimum value of ρ_{xx} is observed at $B \approx 1.8$ T for all temperatures. At $V_g = -0.259$ V [figure 5.9(b)], there is only one temperature independent point $C_{2,*}$ in ρ_{xx} which corresponds to the spin-degenerate $\nu = 2$ state. For $V_g = -0.2565$ V, we observed temperature independent points at $B = 1.61$ T and $B = 2.01$ T for the transitions $0 \rightarrow 2$ and $2 \rightarrow 0$, respectively. This is similar to transitions observed in references [14, 15, 16]. The dotted lines indicate the ρ_{xy} taken at $T = 122$ mK [figure 5.9(c)] and $T = 49$ mK [figure 5.9(d)]. As the effective disorder is decreased the spin-degenerate $\nu = 2$ state and the spin-split $\nu = 1$ state become resolved. At $V_g = -0.235$ V shown in figure 5.9(d), we observe transitions occurring at C_2 ($B = 1.25$ T) and C_1 ($B = 5.40$ T) for $0 \rightarrow 2$ and $1 \rightarrow 0$, respectively.

In figure 5.10, we also show ρ_{xx} and ρ_{xy} at very low carrier densities as a function of magnetic field for a sample with a lower InAs coverage of 2.15MLs (C1126). The temperatures used range between 62 mK and 295 mK. At $V_g = -0.124$ V [figure 5.10(a)], all of the ρ_{xx} traces show an insulating state, which is similar in behaviour to figure 5.9(a). However, the transitions now start at the spin-split quantum Hall liquid state $\nu = 1$ for $V_g = -0.122$ V. Figure 5.10(b) and (c) show the two transitions C_* and C_1 for transition $0 \rightarrow 1$ and $1 \rightarrow 0$, respectively. This situation was also experimentally observed in references. [18, 23] At $V_g = -0.116$ V [figure 5.10(d)] we observed the transitions between the phase $0 \rightarrow 2 \rightarrow 1 \rightarrow 0$.

We mapped out the experimental phase diagram for the integer quantum Hall effect using the temperature independent points in ρ_{xx} at different gate voltages. Figure 5.11 shows two different type of quantum Hall phase diagram possible, both including spin-degenerate $\nu = 2$ and spin-polarised $\nu = 1$ integer quantum Hall states. The open circles indicate the spin-down localised state between the $\nu = 2$ and $\nu = 1$ integer quantum Hall

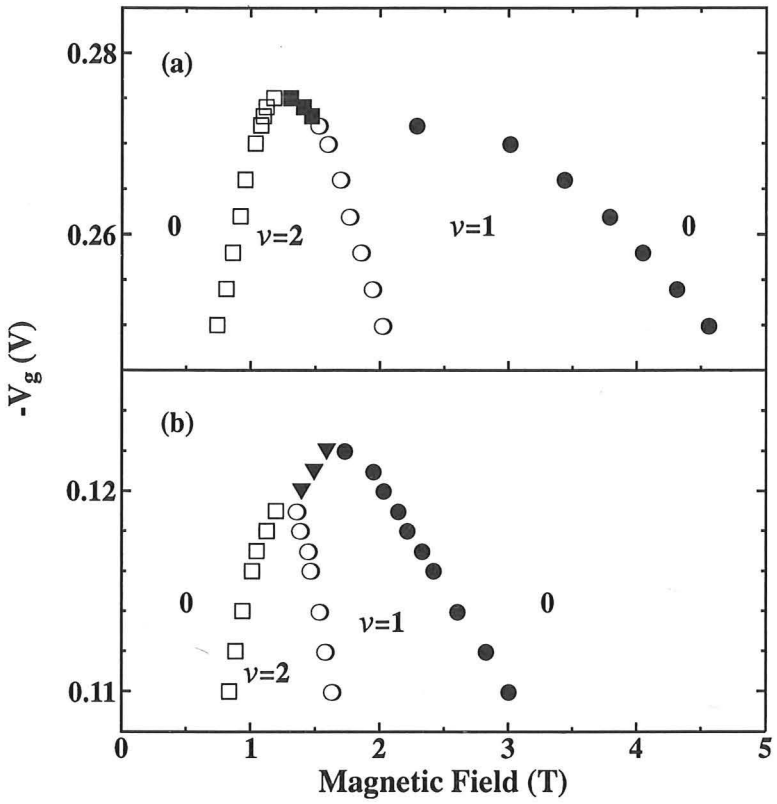

Figure 5.11: The experimental phase diagrams obtained from the temperature independent transition points for samples C1125 (1.61 MLs) and C1126 (2.15 MLs). Symbols indicate transitions from (i) $0-2$ (open squares), (ii) $2-0$ (solid squares), (iii) $2-1$ (open circles), (iv) $1-0$ (solid circles), and (v) $0-1$ (solid triangles).

states. The novel features of the phase diagram shown in figure 5.11(a), for sample C1125, are as follows. Firstly, a field sweep with a fixed bias between $V_g = -0.275$ V and -0.273 V only shows the $(0 \rightarrow 2 \rightarrow 0)$ transitions through the spin-degenerate $\nu = 2$ quantum Hall liquid. The transitions to the quantum Hall liquid at $\nu = 2$ is seen at fields about four times lower than in previous work [14, 15, 16, 17]. Secondly, field sweeps with $V_g > -0.273$ V illustrate the transition from the spin-degenerate ($\nu = 2$) to the spin-polarised ($\nu = 1$) quantum Hall liquids $(0 \rightarrow 2 \rightarrow 1 \rightarrow 0)$.

Increasing the disorder (greater InAs coverage), figure 5.11(b) shows the transition observed between the insulator and the $\nu = 1$ quantum Hall liquid $(0 \rightarrow 1 \rightarrow 0)$ at biases $(-0.122 \text{ V} \leq V_g \leq -0.119 \text{ V})$. At lower biases $(V_g < -0.119 \text{ V})$ one again sees the $(0 \rightarrow 2 \rightarrow 1 \rightarrow 0)$ transition. A similar phase diagram has been reported by Shahar *et al.* [18] in a high mobility sample.

The position of the triple point where the insulating state meets both the spin-degenerate $\nu = 2$ and spin-polarised $\nu = 1$ integer quantum Hall states indicates where the three states finally become merged. When the carrier density decreases, the triple point on the phase diagram shifts from $B = 1.6$ T [figure 5.11(a)] to $B = 1.3$ T [figure 5.11(b)]. Both phase diagrams show the disorder induced termination of the spin-splitting in the integer quantum Hall effect.

We show ρ_{xx} from sample C1125 with no illumination, this may be compared with the illuminated results at three biases $V_g = -0.067$ V [figure 5.12(a)], -0.065 V [figure 5.12(b)], and -0.050 V [figure 5.12(c)] for temperatures between 90 mK and 355 mK. The inset to figure 5.12(b) shows an enlargement of the C_1, $C_{2,*}$, and $C_{1,*}$ transitions. The ρ_{xy} data in figure 5.12(c) was taken at a temperature of $T = 156$ mK. At a bias of $V_g = -0.067$ V the field sweep shows only one localised-delocalised transition between the insulator and the $\nu = 2$ quantum Hall liquid. This transition

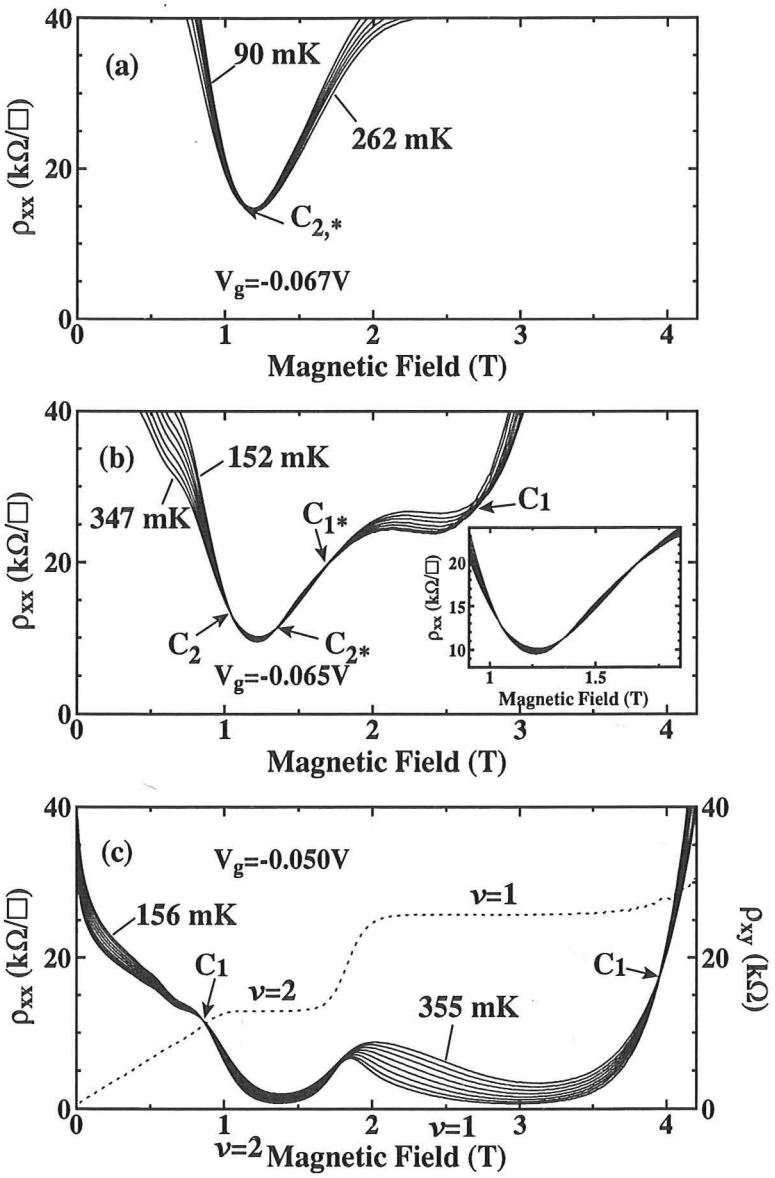

Figure 5.12: ρ_{xx} vs B for temperatures 90 mK $\leq T \leq$ 355 mK for sample C1125 (1.61 MLs). The inset to (b) shows an enlargment between 0.9 and 1.8 T. The dotted line in (c) shows ρ_{xy} at temperature 156 mK.

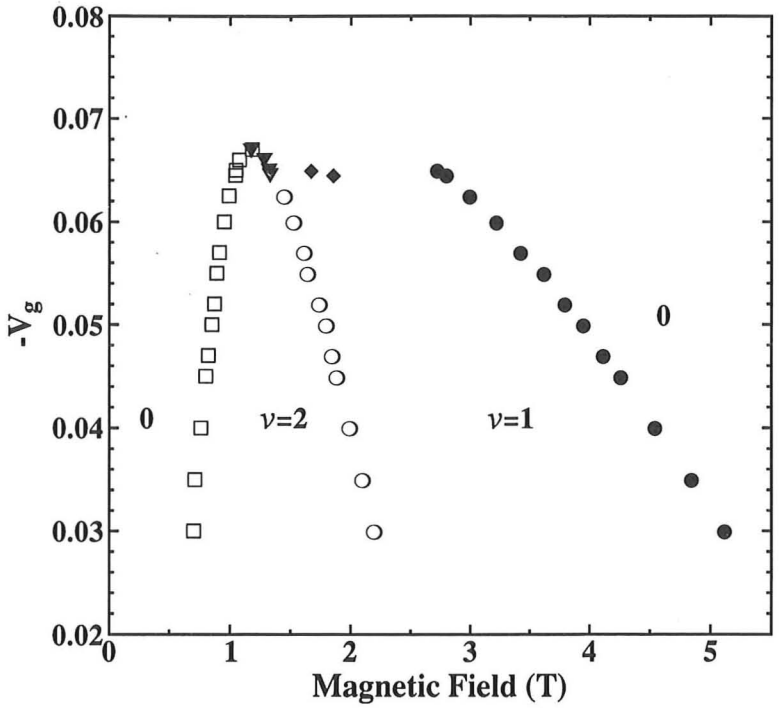

Figure 5.13: The experimental phase diagram obtained from the temperature independent transition points for C1125 (1.61 MLs) in the dark. Symbols indicate transition from (i) $0-2$ (open squares), (ii) $2-0$ (solid triangles), (iii) $2-1$ (open circles), (iv) $0-1$ (solid diamonds), and (v) $1-0$ (solid circles).

is designated by $C_{2,*}$ and occurs at 1.6 T in figure 5.12(a). At low gate biases (-0.062 V $\leq V_g \leq -0.030$ V) in figure 5.12(c), we see the familiar transitions $0 \rightarrow 2 \rightarrow 1 \rightarrow 0$ which have the characteristics similar to those in figures 5.9(d) and 5.10(d). Remarkably, between biases of $V_g = -0.0645$ V and $V_g = -0.0650$ V we can see both the $C_{2,*}$, and $C_{1,*}$ transitions, $2 \rightarrow 0$ and $0 \rightarrow 1$, respectively, in the same field sweep. This corresponds to the transitions $0 \rightarrow 2 \rightarrow 0 \rightarrow 1 \rightarrow 0$ and is referred to as the 'camel back' structure in the phase diagram. In figure 5.13, we show the experimental phase diagram using temperature independent points from the ρ_{xx} traces at different gate voltages. We observed another new type of phase diagram

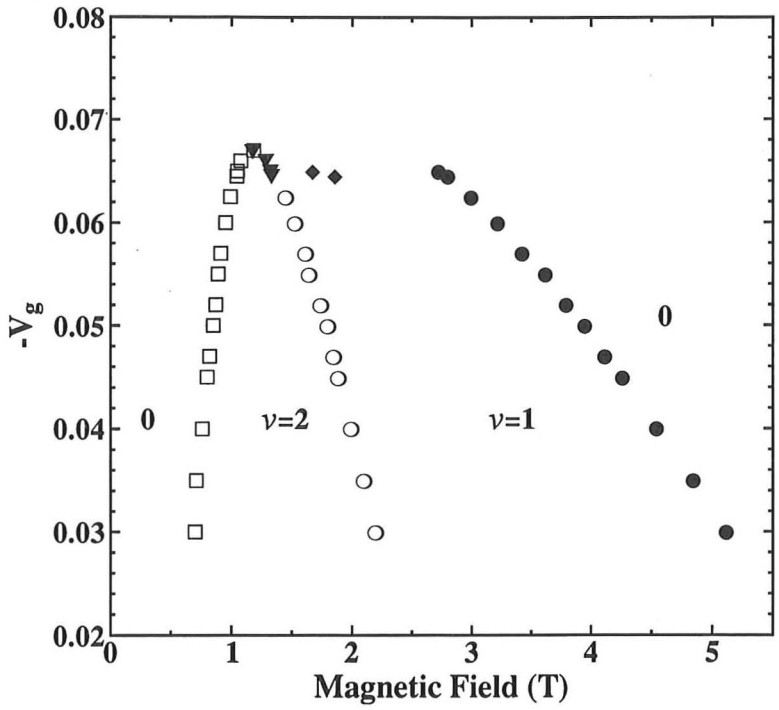

Figure 5.13: The experimental phase diagram obtained from the temperature independent transition points for C1125 (1.61 MLs) in the dark. Symbols indicate transition from (i) $0-2$ (open squares), (ii) $2-0$ (solid triangles), (iii) $2-1$ (open circles), (iv) $0-1$ (solid diamonds), and (v) $1-0$ (solid circles).

is designated by $C_{2,*}$ and occurs at 1.6 T in figure 5.12(a). At low gate biases (-0.062 V $\leq V_g \leq -0.030$ V) in figure 5.12(c), we see the familiar transitions $0 \rightarrow 2 \rightarrow 1 \rightarrow 0$ which have the characteristics similar to those in figures 5.9(d) and 5.10(d). Remarkably, between biases of $V_g = -0.0645$ V and $V_g = -0.0650$ V we can see both the $C_{2,*}$, and $C_{1,*}$ transitions, $2 \rightarrow 0$ and $0 \rightarrow 1$, respectively, in the same field sweep. This corresponds to the transitions $0 \rightarrow 2 \rightarrow 0 \rightarrow 1 \rightarrow 0$ and is referred to as the 'camel back' structure in the phase diagram. In figure 5.13, we show the experimental phase diagram using temperature independent points from the ρ_{xx} traces at different gate voltages. We observed another new type of phase diagram

in the quantum Hall effect states at $\nu = 2$ and $\nu = 1$. In Si MOSFETs the camel back structure, recently reported by Kravchenko *et al.* [24] was attributed to many-body enhancements of the energy gaps at integer filling factors.

5.6 Spin effects

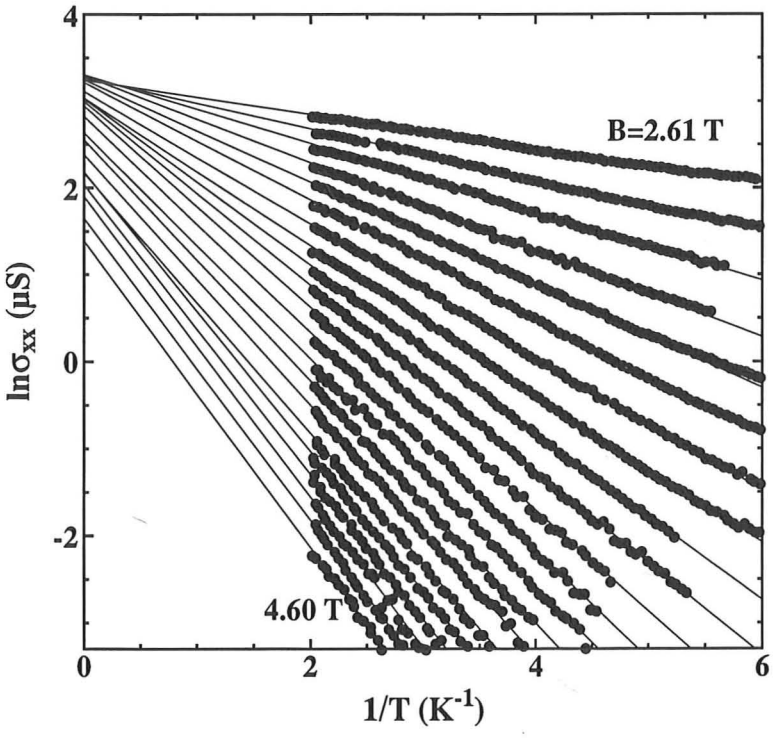

Figure 5.14: Activation plots at $\nu = 1$ for sample C1125 for magnetic fields. B=2.61, 2.78, 2.84, 3.00, 3.10, 3.20, 3.30, 3.40, 3.50, 3.60, 3.70, 3.80, 3.90, 4.00, 4.10, 4.20, 4.30, 4.37, 4.45, 4.52, and 4.60 T.

The delocalised spin-up and spin-down states occur when the disorder width Γ of the Landau level is smaller than the Zeeman energy. ΔE_s is defined as the energy to flip a spin. The exchange gap of the energy splitting between the Ladau level subbands for high mobility GaAs samples was estimated to be $\sim$ 20 times higher than the bare Zeeman energy [25, 26]. When

$\Gamma \gg \Delta E_s$, we expect that two delocalised states merge to form a single peak of the density of states. Theoretically, Fogler and Shklovskii [21] studied the disorder induced collapse of spin-splitting and its implications on the global phase diagram. Experimentally, Wong *et al.* [22] observed recently the collapse of spin-splitting in the filling factor $\nu \geq 2$ for spin gaps related with carrier density. At zero temperature, electrons are localised within the disorder potential at zero and finite magnetic fields. Tunnelling between localised states may make a small contribution to the transport conductance. At slightly higher temperatures, electrons are thermally excited from the localised states in a Landau level tail to the extended states at the centre of the next available Landau level. Therefore, the activation energy for the spin effect can be measured from the activated temperature dependence of the ρ_{xx} at odd filling factors.

In the section we study the collapse of spin-splitting in the quantum Hall effect using activation energies deduced from the temperature dependence of the conductivity. Figure 5.14 shows the experimental conductivity for $\nu = 1$ in sample C1125 for temperature below 500 mK. The device was measured at different biases whilst changing the magnetic field to maintain the filling factor at $\nu = 1$. The measured values of ρ_{xx} and ρ_{xy} were converted to σ_{xx} using equation 5.1, where ρ_{xy} has quantized value h/e^2, when the ρ_{xx} minima are in activated regions. Expressed in terms of ΔE_s and T for σ_{xx} is given by;

$$\sigma_{xx} = \sigma_0 \exp\left(-\frac{\Delta E_s}{2k_B T}\right), \tag{5.2}$$

where σ_0 is related to temperature independent minimum metallic conductivity.

Extracting the activation energy ΔE_s from the gradients in figure 5.14 we plot the parameter $\Delta E_s/k_B$ as a function of magnetic field in figure 5.15. The dashed lines show the bare Zeeman splitting $\mid 0.44\mu_B B \mid$.

Figure 5.15(a) and (b) show data from samples C1125 and C1126, re-

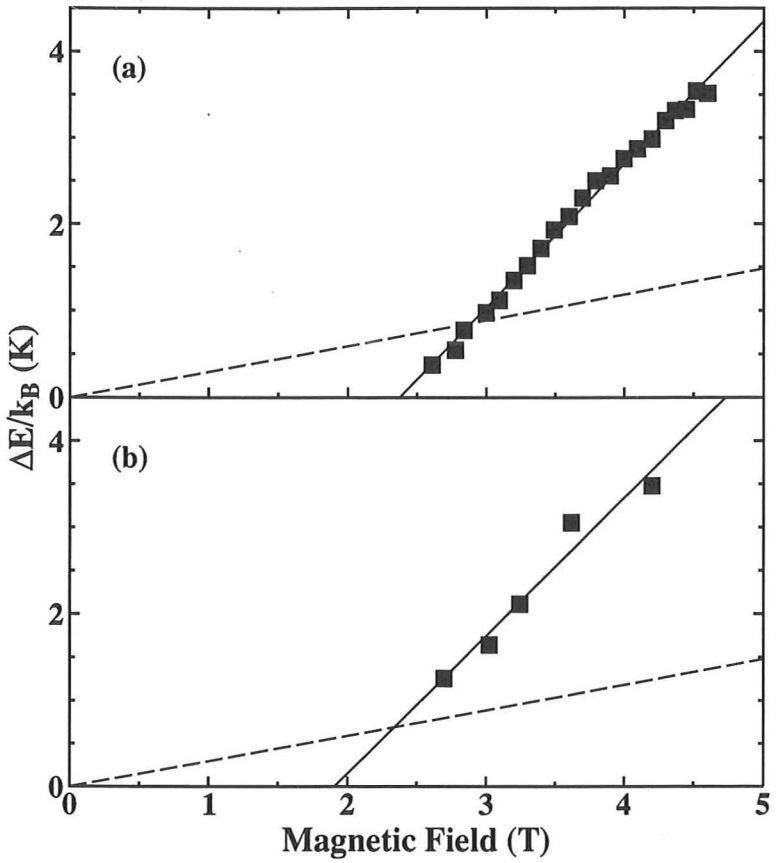

Figure 5.15: Plots of $\Delta E_s/k_B$ vs B obtained from the activation measurements of σ_{xx} at $\nu = 1$ for samples (a) C1125 and (b) C1126. The dotted lines show the bare Zeeman energy assuming $\mid g \mid = 0.44$.

spectively. The corresponding phase diagrams are seen in figure 5.11(a) and (b). The spin gap in sample C1125 is approximately linear with magnetic field and the collapses at $B \sim 2.4 \pm 0.1$ T. Similarly, for sample C1126, the spin gap decreases linearly to zero at a field of $B \sim 1.9 \pm 0.2$ T.

5.7 Conclusions

In summary, we have shown that the transport properties are correlated to the thickness of the InAs layer. The electron mobility at 1.6 K is significantly

decreased at a given carrier density as the InAs thickness increases from 0 to 2.79 MLs. We have also observed that the 2DEG becomes insulating at very low temperatures, due to the strong localisation of electrons in potential fluctuations introduced by the InAs layers. We have constructed the three different types of experimental phase diagram with the insulating, spin-degenerate $\nu = 2$, and spin-polarised $\nu = 1$ states. We have also studied the disorder induced collapse of spin-splitting in the lowest Landau level.

Bibliography

[1] K. Tillmann, D. Gerthsen, P. Pfundstein, A. Förster, and K. Urban, J. Appl. Phys. **78**, 3824 (1995).

[2] See, for example, C. Weisbuch and B. Vinter, *Quantum Semiconductor Structures,* (Academic, New York, 1991).

[3] T. Ando, J. Phys. Soc. Jpn. **51**, 3900 (1982).

[4] C. T. Foxon, J. J. Harris, R. G. Wheeler, and D. E. Lacklison, J. Vac. Sci. Technol. **B 4**, 511 (1986).

[5] N. F. Mott *et al.*, *Electronic Processes in Non-crystalline Materials,* (Clarendon, Oxford, 1979).

[6] H. Aoki and T. Ando, Solid State Commun. **38**, 1079 (1981).

[7] D. Stein, K. von Klitzing, and G. Weimann, Phys. Rev. Lett. **51**, 130 (1983).

[8] G. Lommer, F. Malcher, and U. Rossler, Phys. Rev. B **32**, 6965 (1985).

[9] M. J. Yang, R. J. Wagner, B. V. Shanabrook, J. R. Waterman, and W. J. Moore, Phys. Rev. B **47**, 6807 (1993).

[10] E. Abrahams, P. W. Anderson, D. C. Licciardello, and T. V. Ramarkrisham, Phys. Rev. Lett. **42**, 673 (1979).

[11] D. E. Khmelnitskii, Phys. Lett. **106**, 182 (1984); JETP Lett. **38**, 556 (1983).

[12] R. B. Laughlin, Phys. Rev. Lett. **52**, 2304 (1984).

[13] S. Kivelson, D. Lee, and S. Zhang, Phys. Rev. B **46**, 2223 (1992).

[14] H. W. Jiang, C. E. Johnson, K. L. Wang, and S. T. Hannahs, Phys. Rev. Lett. **71**, 1439 (1993).

[15] T. Wang, K. P. Clark, G. F. Spencer, A. M. Mack, and W. P. Kirk, Phys. Rev. Lett. **72**, 709 (1994).

[16] R. J. F. Hughes, J. T. Nicholls, J. E. F. Frost, E. H. Linfield, M. Pepper, C. J. B. Ford, D. A. Ritchie, G. A. C. Jones, E. Kogan, and M. Kaveh, J. Phys.: Condens. Matt. **6**, 4763 (1994).

[17] I. Glozman, C. E. Johnson, and H. W. Jiang, Phys. Rev. Lett. **74**, 594 (1995).

[18] D. Shahar, D. C. Tsui, and J. E. Cunningham, Phys. Rev. B **52**, R14372 (1995).

[19] F. Nihey, M. A. Kastner, and K. Nakamura, Phys. Rev. B **55**, 4085 (1997).

[20] H. Hilke, D. Shahar, S. H. Song, D. C. Tsui, Y. H. Xie, and D. Monroe, Phys. Rev. B **56**, 15545 (1997).

[21] M. M. Fogler and B. I. Shklovskii, Phys. Rev. B **52**, 17366 (1995).

[22] L. W. Wong, H. W. Jiang, E. Palm, and W. J. Schaff, Phys. Rev. B **55**, R7343 (1997).

[23] S.-H. Song, D. Shahar, D. C. Tsui, Y. H. Xie, and Don Monroe, Phys. Rev. Lett. **78**, 2200 (1997).

[24] S. V. Kravchenko, W. Mason, J. E. Furneaux, and V. M. Pudalov, Phys. Rev. Lett. **75**, 910 (1995).

[25] R. J. Nicholas, R. J. Haug, K. von Klitzing, and G. Weimann, Phys. Rev. B **37**, 1294 (1988).

[26] A. Usher, R. J. Nicholas, J. J. Harris, and C. T. Foxon, Phys. Rev. B **41**, 1129 (1990).

Chapter 6

Transport Properties of 2DEGs Containing InAs Self-Assembled Dots

6.1 Introduction

This chapter discusses magnetoresistance measurements performed on GaAs-AlGaAs heterostructures in which self-assembled InAs dots have been inserted in the centre of the GaAs quantum well. Section 6.2 characterises the structure of the InAs dots using *in situ* ultra-high vacuum scanning tunnelling microscopy (UHVSTM), transmission electron microscopy (TEM), and scanning transmission electron microscopy (STEM). Section 6.3 describes the transport and quantum life-times in samples with different InAs dot densities. In section 6.4, experimental phase diagrams for localised-delocalised transitions are mapped using: (i) temperature-independent points in the longitudinal resistivity traces ρ_{xx}, and (ii) the conductivity σ_{xx} peaks.

6.2 Structure of the self-assembled InAs quantum dots

The properties of electrons in one- and zero-dimensional structures have attracted a great deal of interest, both for investigating fundamental physics [1, 2] and device applications [3, 4] such as quantum dot lasers [5, 6] and single electron transistors [7]. However artificially constructed systems, such as a 1D split gate defined by electron beam lithography, can be constrained by technological limitations. A potentially significant route for the fabrication of one-[8, 9, 10] and zero-dimensional [11, 12, 13] nanostructures is by natural formation during the growth procedure. For example, self-assembled quantum dots can be created in the Stranski-Krastanov growth mode by growing a highly strained layer above a critical thickness. By employing InGaAs layers grown on (100)GaAs [14], self-assembled InGaAs dots have recently been realised. In the case of growing InAs on the GaAs substrate, the lattice mismatch is very much higher $\approx 7\%$ and we have carried out an extensive study to characterize the growth of self-assembled dots. Previously, the density and size of the dots has been controlled by varying the InAs deposition and improvements in the InAs dot assembly have concentrated on this front. We investigate the effect of the GaAs capping layer deposited upon the InAs islands and show that this strongly affects the dot assembly.

6.2.1 Characterization of the InAs coverage using STM

The surface morphology of the InAs on GaAs(100) was characterized as a function of InAs coverage using an *in situ* UHVSTM. The images were taken by Dr. Stuart Brown. Fig. 6.1 shows 500 nm×500 nm UHVSTM images of different wafers with InAs coverages of 0.81, 1.61, 2.79, and 4.21 MLs. These coverages have been estimated from the MBE growth of each device.

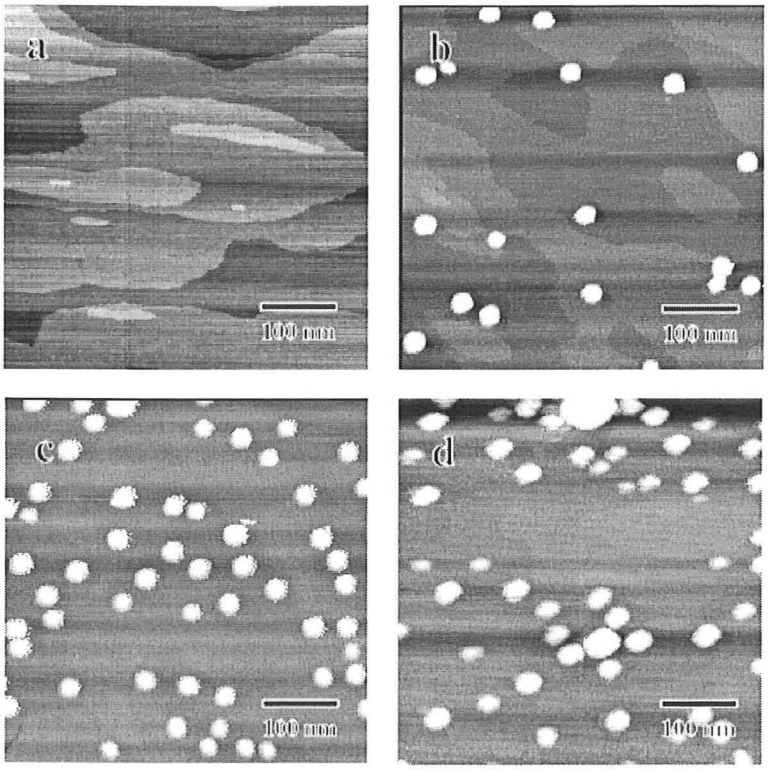

Figure 6.1: 500 nm×500 nm STM images of self-assembled InAs dots formed with varying coverage of InAs on GaAs. Estimated InAs coverage is 0.81, 1.61, 2.79, and 4.21 MLs for (a) through (d), respectively. Images taken by Dr. S. J. Brown.

Figure 6.1(a) is a representative image of the strained InAs surface prior to island nucleation. In this case the surface appears smoother with less jagged terrace edges and more rounded islands than an equivalent GaAs surface grown at this temperature. The anisotropy in the dimensions of the monolayer islands of GaAs(100) is such that they are elongated in the $[01\bar{1}]$ direction by a factor of 10:1 with respect to the [011] direction. However, with an InAs coverage of 1.20 MLs (not shown) there is an anisotropy of 4.6:1, also elongated in the $[01\bar{1}]$ direction, whilst for higher coverages from 1.34 to 1.61 MLs the anisotropy is typically 2.7:1. Such changes could be anticipated as the GaAs surface is transformed to InAs and the growth

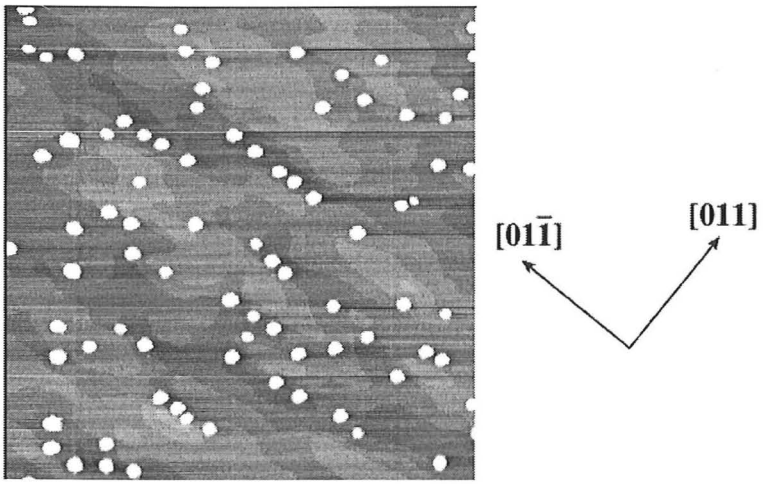

Figure 6.2: 1 μm $\times$ 1 μm UHVSTM scan (sample C1107) showing the uniform size distribution of InAs islands. These images have been contrast enhanced so that the step edges can be resolved. Image taken by Dr. S. J. Brown.

kinetics change, which in turn modify the surface morphology. Atomic scale images of the (100) surface with increasing InAs coverage, prior to island nucleation, by Yamaguchi *et al.* [15] show the surface atomic structure changing from the single As-dimer (2×4).

We have observed the formation of InAs islands when the InAs coverage is greater than 1.6 MLs [figure 6.1(b)]. These measurements were supported by further investigations using AFM. The average dot widths ($\sim$ 260 Å) and the heights ($\sim$ 80 Å) are in close agreement with high resolution cross sectional TEM measurements performed by Guha *et al.* [16]. The critical InAs coverage required for maximum dot density is estimated to be 2.15 MLs from published work [17]. Upon increasing the coverage above 2.15 MLs the density of dots decreases as they coalesce, as has previously been reported [18]. This is the case in figure 6.1(c) for a coverage of 2.79 MLs. With a coverage of 4.21 MLs the majority of features have become irregular shaped clusters, as shown in figure 6.1(d).

The large area image in figure 6.2 for 1.61 MLs shows that due to the anisotropy of the surface morphology there is a greater chance of nucleating on the step edge of islands, which are parallel to the $[01\bar{1}]$ direction. Therefore groups of dots have a tendency to be orientated in a line. Figure 6.2 also shows the uniformity of the islands' size distribution and that the average self-assembled dots are $\sim$ 260 Å in diameter and $\sim$ 80 Å in height, corresponding to a dot density of $\sim 1.0 \times 10^{10}$ cm^{-2}.

6.2.2 TEM characterization of the GaAs capping layer

We show that the sublimation of the self-assembled InAs dots is strongly affected by the degree of partial coverage of the GaAs capping layer. By varying the thickness of the GaAs cap, the sublimation can be controlled leading to a narrowing of the dot size distribution and modification of the dot height. The following TEM images are used to illustrate a number of points; firstly how the coverage of the GaAs cap layer affects the InAs dot formation and secondly the structure of the InAs clusters.

Three samples were grown with the same general structural sequence but with different growths of GaAs in the top half of the GaAs quantum well layer, this half being the capping layer for the InAs dot structure. The thickness of the GaAs capping layers considered are d_c = 100 Å, 50 Å, and 10 Å and were grown over the InAs dots at T = 530°C. This is shown schematically in figure 6.3.

Figure 6.4 shows plan view TEM images of the two samples C1349 and C1335. These TEM images were taken by Dr. Guoda Lian. For sample C1349 in figure 6.4(a), the InAs dots are clearly resolved through the well-known strain contrast mechanism of Ashby and Brown [19]. The dot density with a 100 Å GaAs capping layer ($\sim 5.8 \times 10^9$cm^{-2}) is approximately one quarter the value that would be expected [20] ($\sim 2.2 \times 10^{10}$cm^{-2}) if there were no capping layer. This reduction in dot density is also accompanied

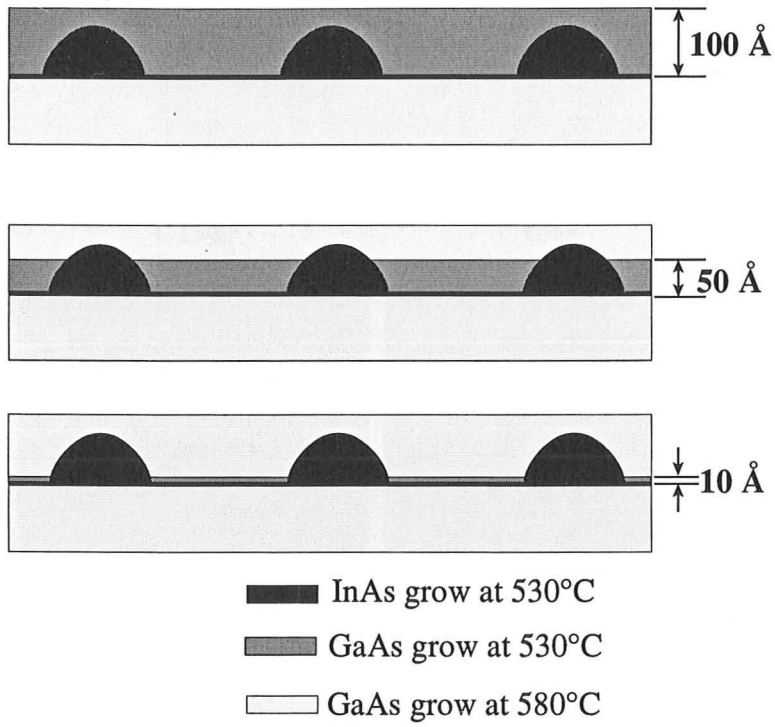

Figure 6.3: Schematic diagram of InAs self-assembled dots for three different coverages of GaAs at 530°C: (a) 100 Å (b) 50 Å and (c) 10 Å.

by a broadened size distribution [20, 21], shown in figure 6.4(c), and is a result of the overlayer growth. Further reductions in the width of the GaAs overlayer, figure 6.4(b), decrease the dot density to $\sim 3.0 \times 10^{9}$ cm^{-2} whilst narrowing the dot size distribution [figures 6.4(c)]. It is clear, therefore, that the redistribution of InAs depends strongly upon the thickness of the GaAs overlayer. The same trends are clearly apparent in the cross-sectional images shown later.

A closer examination (figure 6.5) of the plan-view TEM image in figure 6.4 reveals contrast variations between InAs dots. An area is imaged at higher magnification using the two-beam strain contrast to reveal two different forms of clusters. Those clusters showing a line of no contrast perpendicular to the g-vector [19] are coherent, those with much stronger

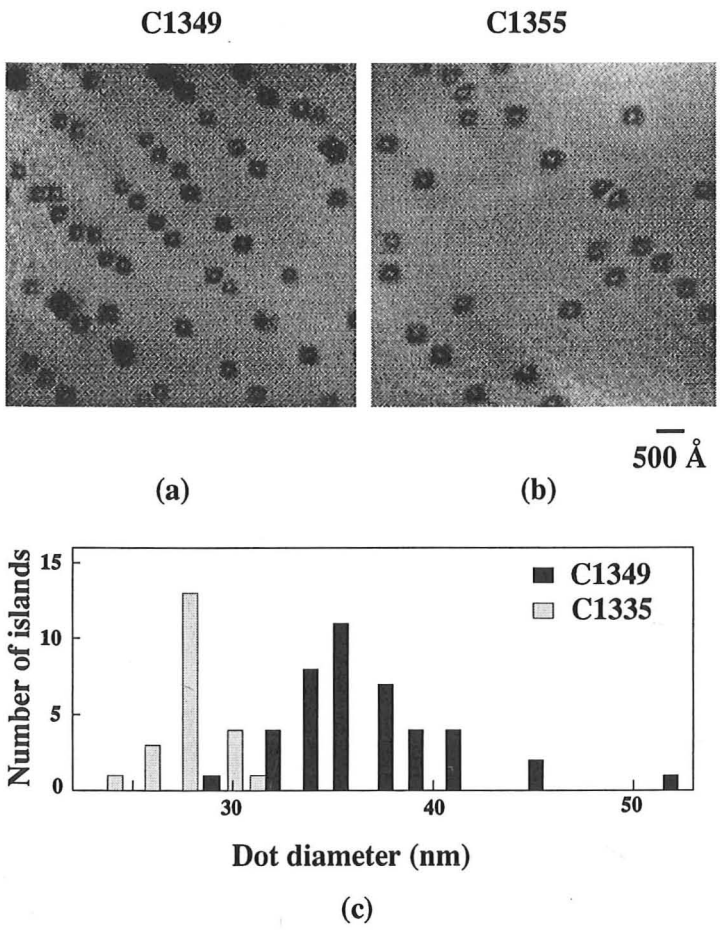

Figure 6.4: Plan view TEM images of sample for (a) GaAs capping layer d_c = 100 Å (the wafer number C1349) and (b) d_c = 50 Å (C1335). Histograms (c) of dot diameter with an approximate error of ± 1 nm. Both samples have been grown with 2.15 MLs of InAs.

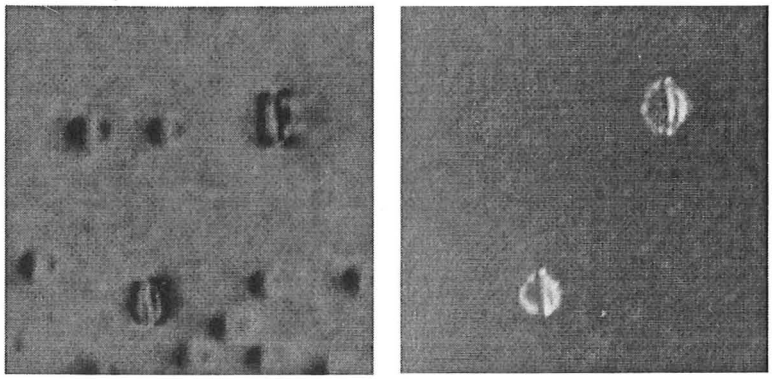

Figure 6.5: (a) Bright field and (b) weak beam dark field ($g/3g$) plan view TEM images of the same area for sample C1349.

and complicated strain contrast are incoherent. The incoherent clusters are clearly revealed by the threading dislocation lines imaged by the TEM in the g/3g weak beam dark field condition [figure 6.5(b)]. The number of incoherent clusters in sample C1349 is about 12% of the total clusters present whereas no incoherent clusters are observed in samples from wafer C1335. It is interesting that the coherent islands have insufficient strain to be visible in the weak beam images.

When InAs is grown on GaAs atoms, the first few atomic layers arrange themselves in a planar layer called the wetting layer. As epitaxial growth proceeds the atoms tend to bunch up and form clusters. Plastically relaxed cluster formation is energetically favourable over growth of pseudomorphic quantum dots and thus reduces the strain energy within the dots. Figure 6.6(a) shows a cross-sectional strain field TEM image of an InAs dot buried in the GaAs quantum well. The absolute size of the InAs dot is expected to be smaller than apparent in figure 6.6(a), since it is the strain field near the dot which actually causes the contrast [22]. Figures 6.6(b) and (c) show a schematic diagrams of the coherent and incoherent cluster

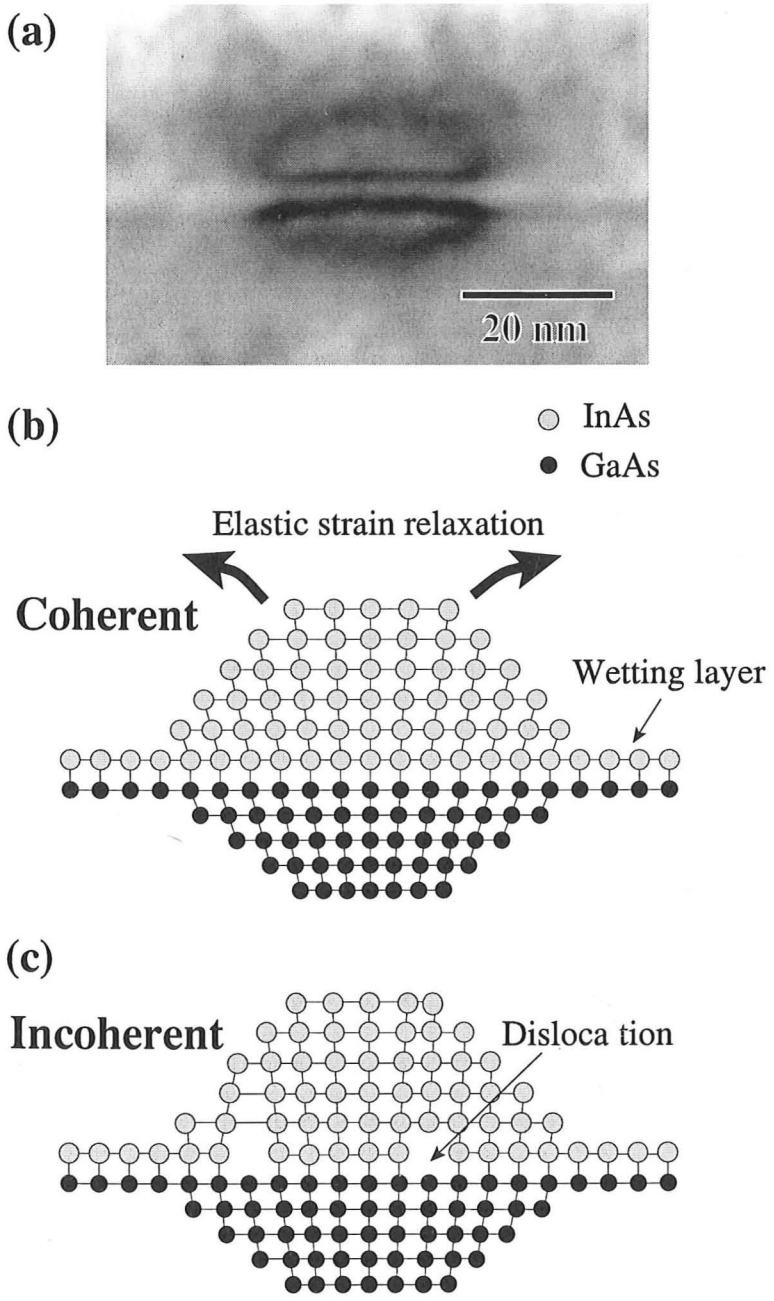

Figure 6.6: (a) A cross-sectional TEM image of a coherent InAs cluster in GaAs. A schematic diagram of (b) coherent and (c) incoherent cluster formation during epitaxial growth of InAs on top of GaAs.

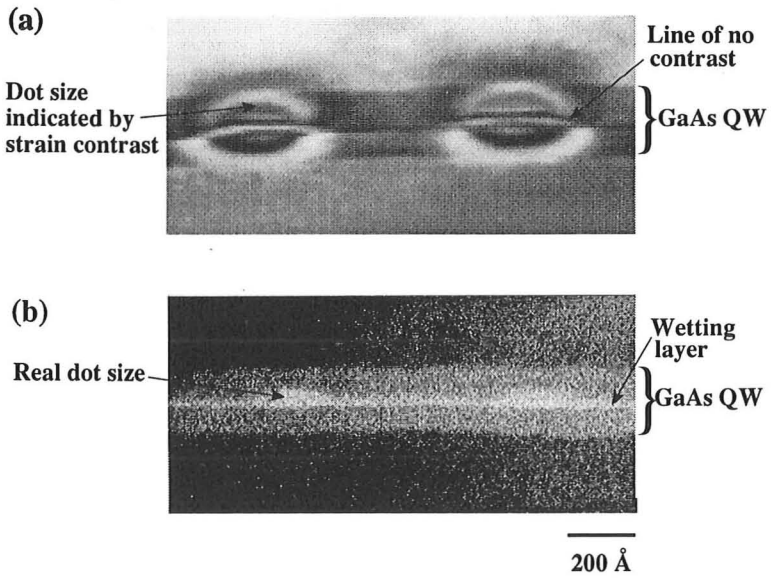

Figure 6.7: The comparison of (a) centred dark field image using TEM and (b) annular dark field image using STEM for sample C1335.

formation, respectively.

To accurately determine the dimensions of the dots, we have used the quasi-kinematic imaging condition suggested by Woolhouse [23] with the incoherent annular dark field imaging (ADF) technique. Figure 6.7 shows the comparison of a centred dark field image, obtained using this technique and an image obtaine using ADF technique (STEM). The TEM image, figure 6.7(a), clearly shows that the strain contrast is dominant and that it is not easy to identify the true dot shape. However the line of no-contrast at the interface between the strained/unstrained layer is seen to bend upwards slightly within the islands indicating the real boundary of the dots. The STEM image in figure 6.7(b) also shows the real InAs islands as well as the wetting layer and the GaAs quantum well. From these measurements, we find the average dimension of the dots to be $\sim$360 Å wide and $\sim$ 80 Å high in sample C1349, and $\sim$ 280 Å wide and 40 Å high in sample C1335.

The evolution of the self-assembled dots in the two samples may be un-

derstood if we consider the desorption sites for the subsequent GaAs cap layer deposition. The incoming adatoms see an inhomogeneous and uneven substrate consisting of the InAs wetting layer, a few monolayers thick, and InAs dots several nanometres in height. The wetting layer is strained to have a lattice spacing approaching that of the bulk InAs crystal. From energetic considerations alone we therefore expect the GaAs overlayer growth to start preferentially on the wetting layer, if the adatoms have sufficient surface mobility. Evidence for such growth selectivity has been demonstrated using AlGaAs multilayers grown upon self-assembled InAs dots on GaAs(100) surfaces [24] and we can expect that our case is similar. As a consequence, we do not expect the top of the InAs dots to be covered by the GaAs overlayer until the equivalent thickness of the total GaAs deposition is at least equal to, or in excess of, the dot height. In reality the GaAs overlayer growth over the dot will be driven both by curvature of the growth front and the redistribution of the strain in the dot. For samples C1349 and C1335, the nominal thickness of the low temperature grown GaAs overlayers (100 Å and 50 Å, respectively) are less than the height of the uncapped InAs dots. Since the growth of the GaAs overlayer takes place at an elevated temperature, we would expect partial evaporation of the InAs dots [25]. This is consistent with the observation that the dot height is reduced to 40 Å in sample C1335. As the dots are not completely evaporated there remains some partial protection of the dot from the edge of the islands.

From sample C1349 to sample C1335 there is a reduction in dot density from 5.8×10^9 cm^{-2} to 3.0×10^9 cm^{-2} (counting from an area of ~ 12 μm^2), and a complete absence of incoherent clusters in sample C1335. This suggests that the partial protection offered by the partial GaAs layer cap in sample C1335 is not fully effective at reducing evaporation for some of the clusters. This is possible if the cluster is sufficiently large that evaporation proceeds from the centre towards the edge. We have evidence for this in the

observation of some ring shaped clusters in sample C1335. It is also likely that the longer clusters have a more relaxed surface, hence are more difficult for the GaAs adatoms to adhere to. Therefore the larger clusters remain uncovered for larger periods and are likely to undergo selective thermal desorption. This is supported by the narrower size distribution for dots found in sample C1335. The same mechanism is thought to be responsible for the disappearance of incoherent dots in sample C1335 since the surface of such large dots will be fully relaxed. The density of voids observed in sample C1335 is consistent with this selective desorption model. The sublimation model outlined has been simplified, as Ga-In intermixing is known to be important as well, however the general consequences remain the same.

6.3 Transport properties of InAs self-assembled quantum dots

The experiments present in this section determine the transport τ_t and quantum τ_q life-times of electrons in GaAs quantum wells with inserted InAs dots. Samples are taken from different areas of the same wafer. We also determine the anisotropy of the mobility in the $[01\bar{1}]$ and [011] directions. A sample with no InAs islands is used as a comparison.

6.3.1 Device structure

The structures and conduction band diagram of a sample are schematically shown in figure 6.8. The 1.5 ML thick InAs wetting layer, characteristic of the Stranski-Krastanow growth mode, is also shown. In this conduction band profile, electrons can be strongly localised in the InAs quantum dots. The growth conditions were the same as in section 5.2 with the exception of different thickness of GaAs capping grown at $T = 530°C$ on the 2.15 MLs of InAs.

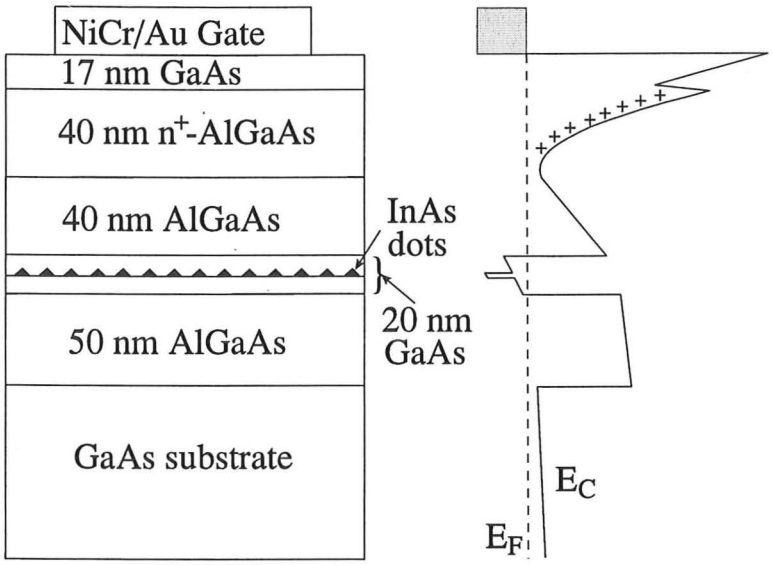

Figure 6.8: Sample structure and conduction band diagram.

Figure 6.9 shows the plan view TEM images from wafer C1349. These samples are taken from three different wafer regions, each with different dot densities. The samples are as follows: C1349c (center of the wafer), C1349m (midway between centre and edge), and C1349e (edge of the wafer). There is a factor of two variation in the InAs dot density between the C1349c and C1349e samples. The experimental dot densities for C1349c [figure 6.9(a)], C1349m [figure 6.9(b)], and C1349e [figure 6.9(c)] are $5.8 \times 10^9 \text{cm}^{-2}$, $4.6 \times 10^9 \text{cm}^{-2}$, and 2.5×10^9 cm^{-2}, respectively. This values are counted from an area of ~ 12 μm^2.

6.3.2 Transport and quantum life-times

To illustrate how the disorder introduced by the InAs dots affects the transport and quantum life-times, a number of samples with differing InAs dot densities have been studied. Sample C1127 has a 200 Å GaAs quantum well with no inserted InAs islands. All of the devices were processed using standard optical lithgraphy and wet etching into Hall bars. A NiCr/Au gate

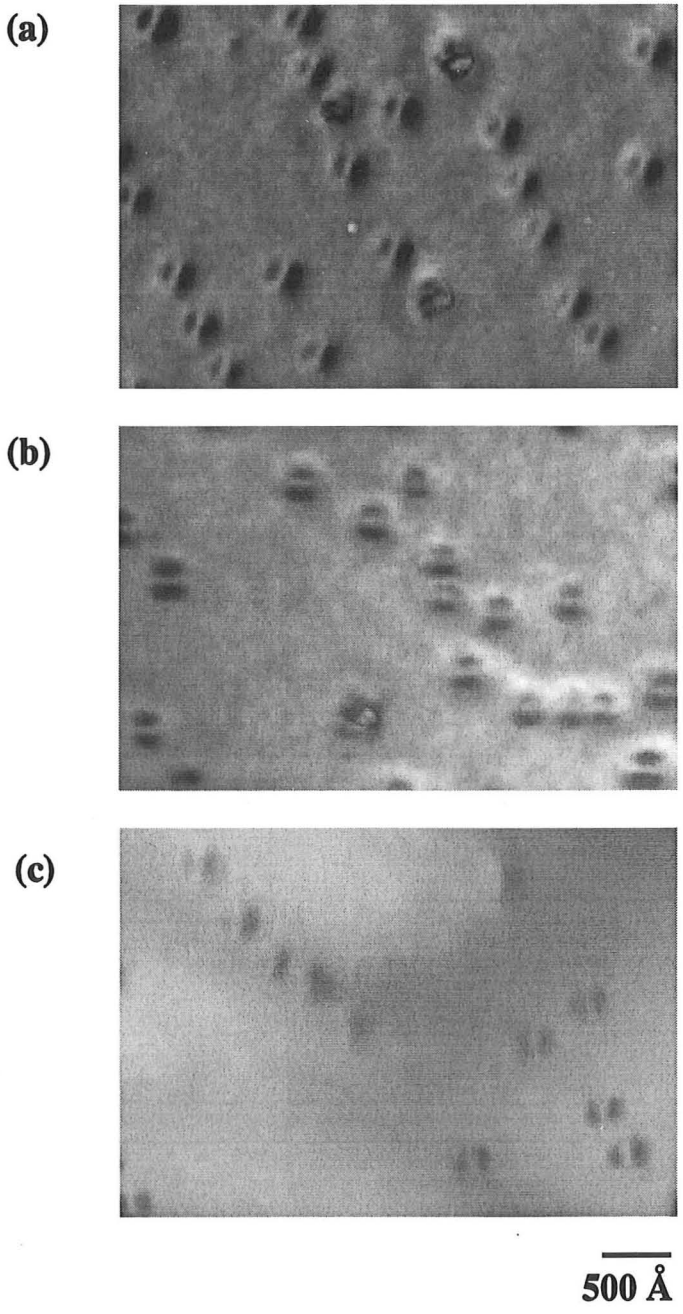

Figure 6.9: Plan view TEM images of self-assembled InAs dots an wafer C1349 for three different regions: (a) centre, (b) midway between centre and edge, and (c) edge.

Wafer	Sample	μ ($\times 10^4 \mathrm{cm}^2/\mathrm{Vs}$)	n_s ($\times 10^{11} \mathrm{cm}^{-2}$)	τ_t (ps)	τ_q (ps)	d_c (Å)
C1127	-	18.48	2.52	6.85	0.41	-
C1335	edge	4.70	3.00	1.79	0.37	50
C1335	middle	3.20	3.00	1.22	0.26	50
C1335	centre	2.40	3.00	0.91	0.22	50
C1349	edge	2.50	2.95	0.95	0.13	100
C1349	middle	1.50	2.95	0.57	0.10	100
C1349	centre	1.10	2.95	0.41	0.08	100

Table 6.1: Sample characteristics for transport measurements in the [011] direction at 1.6 K. d_c is the thickness of GaAs capping layer on InAs dots at 530°C. All samples were required illumination with a red LED to promote conduction.

was deposited to form a surface Schottky gate enabling the 2DEG's carrier density to be changed. Standard low frequency lock-in techniques were used to measure the magnetoresistance with a constant current of 100 nA passed between the source and drain. Table 6.1 shows a summary of the transport characteristics at 1.6 K.

Magnetoresistance measurements show that the resistivity decreases as the InAs dot density decreases. Figure 6.10 shows typical magnetoresistance data for the three different regions of the wafers C1349 and C1335 at $T = 1.6$ K. As each device has equivalent carrier densities the period of the SdH oscillations remains the same. Here the carrier densities have been determined as $2.95 \times 10^{11} \mathrm{cm}^{-2}$ [figure 6.10(a)] and $3.00 \times 10^{11} \mathrm{cm}^{-2}$ [figure 6.10(b)]. For wafer C1349 in figure 6.10(a) the longitudinal resistivity at zero magnetic field increases as the density of InAs dots increases. Consequently the mobility is higher in sample C1349e than in sample C1349c. However, the zero field resistance, and hence the mobilities, for the same

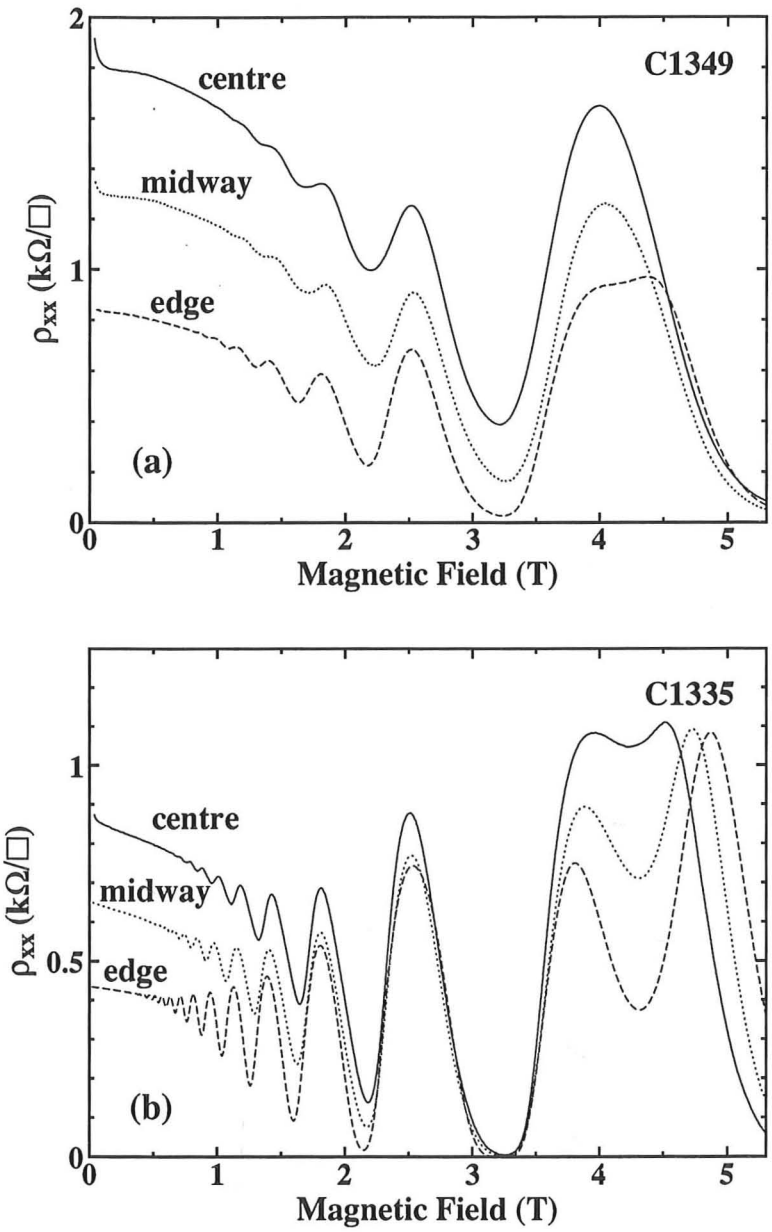

Figure 6.10: Compares the longitudinal resistivity of sample C1349 and C1335 at a carrier density of 2.95×10^{11} and $3.00 \times 10^{11}\text{cm}^{-2}$, respectively for three different part of the wafers C1349 and C1335: centre (solid lines), midway between centre and edge (dotted lines), and edge (broken lines).

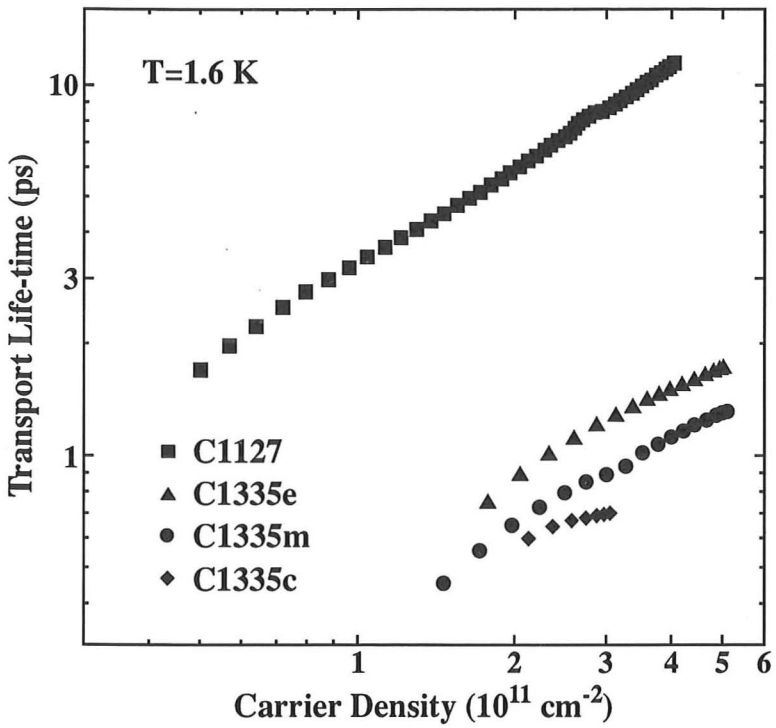

Figure 6.11: Electron mobility μ as a function of carrier density n_s at $T = 1.6$ K.

positions on the wafer are approximately twice as large in wafer C1335. The spin-splitting of the SdH oscillations also reflects the sample disorder. For wafer C1335 in figure 6.10(b) the two spin-split peaks at $\nu = 3$ ($B = 4.3$ T) are well resolved in sample C1335e. However as the sampling point moves towards the centre the increasing disorder (InAs dot density) causes a blurring of the spin-splitting. Similar behaviour, albeit for lower mobilities, is observed in sample C1349.

Figure 6.11 shows the transport life-time as a function of carrier density for samples C1335c, C1335m, C1335e, and C1127 at 1.6 K. The carrier densities were determined by low-field Hall measurements and were varied by applying a front gate voltage. The transport life-time in the reference sample C1127 is about 10 times larger than that of sample C1335 with InAs dots. This extreme reduction in transport life-time is caused by the inserted

InAs dots. For sample C1349, the transport behaviour is similar to C1335 (see table 6.1).

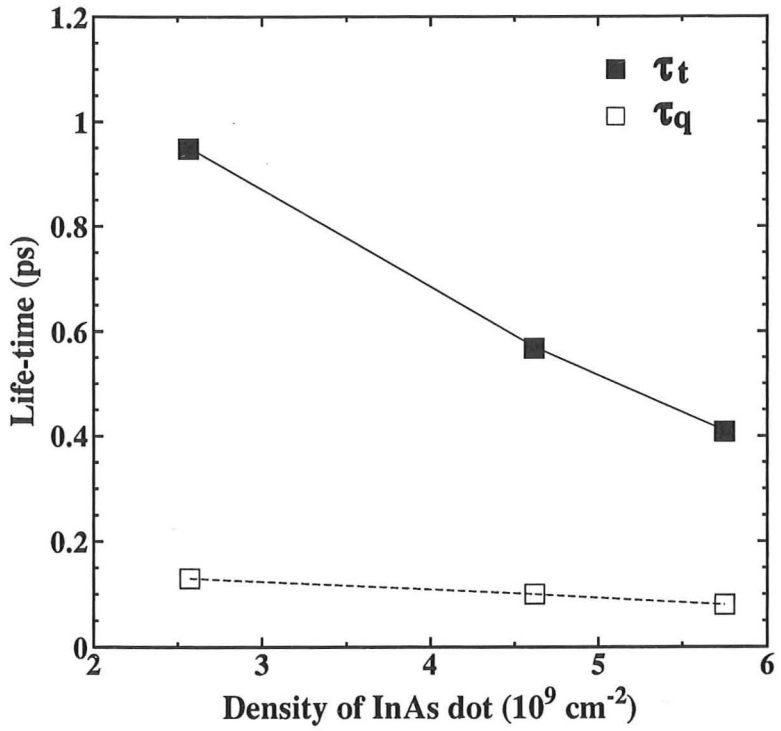

Figure 6.12: Summary of the transport and quantum life-times from wafer C1349. The transport and quantum life-times are plotted as a function of the InAs dot density.

Using the SdH oscillation amplitudes we have determined the quantum life-times. The analysis for the quantum life-times is similar to that employed in section 4.3. Figure 6.12 shows both the transport and quantum life-times plotted against InAs dot density, where the InAs dot densities were determined from TEM images. The quantum life-time decreases as the InAs dot density increases and remains five times smaller than the transport life-time. The ratio between the quantum and transport life-times is a result of the short range scattering due to the inserted InAs dots. For the high mobility 2DEGs formed on (311)B GaAs surfaces (section 4.3), the

ratio of transport to quantum life-time was observed to be greater, between 10 and 70 [26]. This indicates that the dominant scattering mechanism involves long range scattering from remote ionised impurities. In contrast to the GaAs-AlGaAs heterojunction, the SiO_2/Si interface in MOSFETs is very rough, and the transport and quantum life-times are almost the same since interface roughness scattering is the predominant scattering mechanism [27, 28, 29]. In our sample the transport to quantum life-time ratio lies between the values for high mobility GaAs-AlGaAs heterojunctions and MOSFETs.

6.3.3 Anisotropic mobility

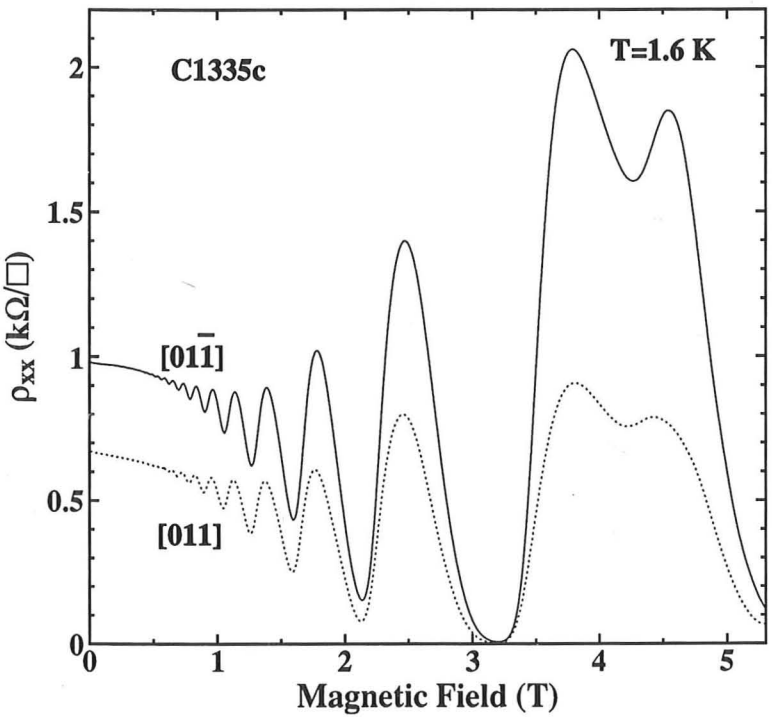

Figure 6.13: ρ_{xx} measured in the [0$\bar{1}$1] and [011] directions of wafer C1335c.

Figure 6.13 shows typical magnetoresistance data for two orthogonal Hall bar orientations on sample C1335c at 1.6 K, at a carrier density of 3.0 $\times$ 10^{11} cm^{-2}. From the zero-field resistance the mobilities are 3.06×10^4 cm^2/Vs

and 2.12×10^4 cm^2/Vs in the [01$\bar{1}$] and [011] directions, respectively. This mobility anisotropy is caused by anisotropy in scattering from the InAs dots.

The anisotropy in the InAs island formation is such that they are elongated in the [01$\bar{1}$] direction at the initial stages (< 1.6 MLs). Upon increasing the InAs coverage above 1.61 MLs the InAs dots nucleate at the step edges. Therefore, InAs dots become linearly ordered along the [01$\bar{1}$] directions as may be observed in figure 6.2. This increases the electron scattering in this direction thereby modifying the mobility.

6.4 Insulator-quantum Hall liquid transitions

This section describes a study on the quantum Hall effect in the disordered 2DEG formed in a GaAs well with inserted InAs dots. The strong, random disorder potential in such devices is provided by the InAs self-assembled dots. With these devices it is also possible to observe a transition between an insulating state and a quantum Hall liquid by increasing the magnetic field. The experimental phase diagrams are determined for this transition by two methods: (i) the crossing points at which ρ_{xx} is virtually temperature independent (section 6.4.1), and (ii) the peaks in σ_{xx} calculated from ρ_{xx} and ρ_{xy} (section 6.4.2).

6.4.1 Temperature dependence

Figure 6.14 shows ρ_{xx} as a function of magnetic field at different temperatures (20 mK $\leq T \leq$ 580 mK) for sample C1335c (2.15 MLs InAs). At $V_g = -0.278$ V [figure 6.14(a)], there are two temperature independent points, C_2 and C_*, in ρ_{xx} for transitions $0 \rightarrow 2 \rightarrow 0$. For a more detailed description of the identification of these states see section 5.5. The ρ_{xx} minimum at a magnetic field of $B \simeq 1.4$ T correspond to the spin-degenerate filling factor $\nu = 2$. At $V_g = -0.260$ V [figure 6.14(b)], we observe the

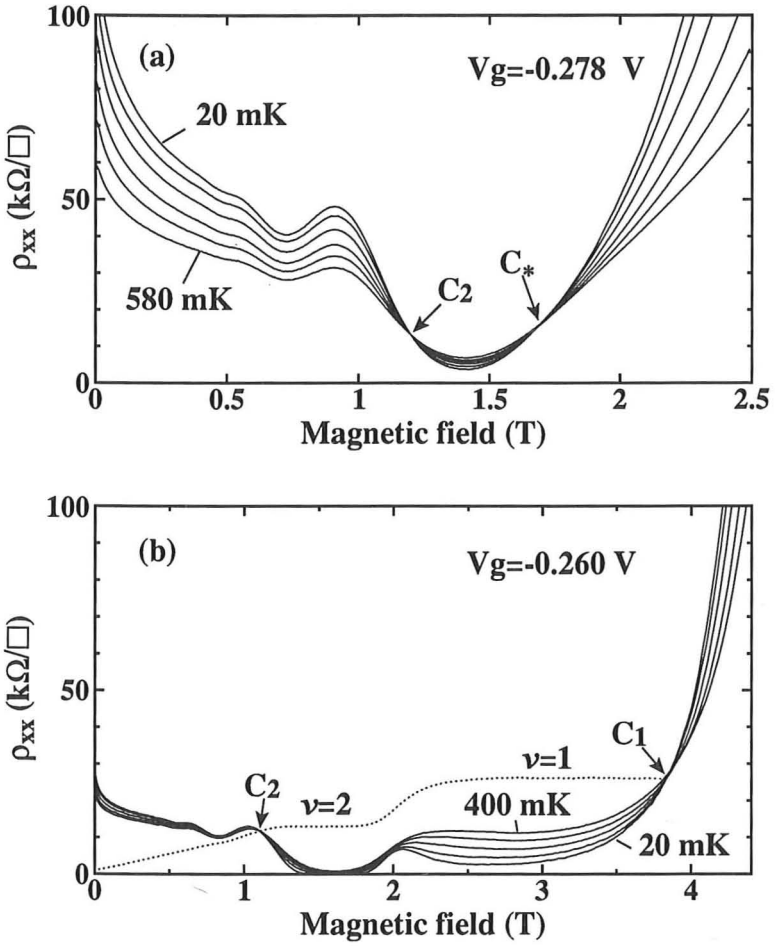

Figure 6.14: ρ_{xx} as a function of magnetic field at temperatures 20 mK $\leq T \leq$ 580 mK for sample C1335 (2.15 MLs InAs). The dotted line in (b) shows ρ_{xy} at $T = 297$ mK.

transitions between phases $0 \rightarrow 2 \rightarrow 1 \rightarrow 0$. Although one can see a weak resistance minimum at $\nu = 4$ ($B \approx 0.7$ T) the resistivity ρ_{xx} continually increases as $T \rightarrow 0$ for this filling factor and all points below C_2 and above C_1. For points between C_2 and C_1 the resistivity decreases as $T \rightarrow 0$, the signature of a quantum Hall liquid. Additionally, ρ_{xy} has wide, well defined plateaus at $\nu = 1$ and $\nu = 2$. The characteristics of the quantum Hall transitions are very similar to the results in section 5.5 for samples with inserted

InAs dashes.

6.4.2 Conduction maxima

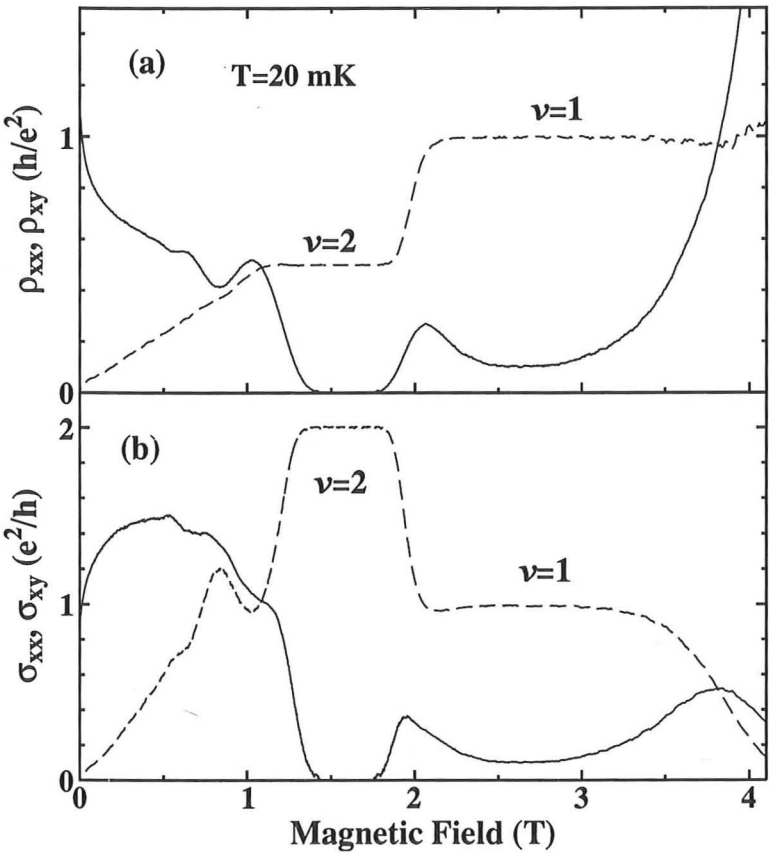

Figure 6.15: (a) ρ_{xx} (solid lines) and ρ_{xy} (dotted lines) as a function of magnetic field for $V_g = -0.260$ V (b) σ_{xx} (solid lines) and σ_{xy} (dotted lines) calculated from the data of (a) by matrix conversion.

In the following we consider the presence of delocalised states in the 2DEG for two extremes of applied magnetic field, low or very strong. For a strong magnetic field, such that ($\omega_c \tau \gg 1$), the Landau levels are well resolved. It is generally accepted that states between Landau levels are localised whilst states at the Landau level energies are delocalised. Through the renormalised conductivity σ_{xx} (resistivity ρ_{xx}) the peaks in σ_{xx} are associated with

the delocalised states. The renormalised Hall conductivity σ_{xy} consists of a descending series of steps of height e^2/h (spin resolved Landau levels), with the plateaus at each conductance minimum. The magnetic fields at which the 2DEG states change from localised to delocalised are therefore identified by the σ_{xx} maxima for which σ_{xy} is midway between plateaus on a downward step with increasing magnetic field.

In the low field regime ($\omega_c\tau < 1$) the Landau level structure is smeared by disorder broadening and the transport is expected to be classical. Weak oscillations will still be seen due to the remaining weak modulation of the density of states by the broadened Landau levels. The conductivities are given by:

$$\sigma_{xx} = \frac{n_s e^2 \tau}{m^*} \left(\frac{1}{1 + (\omega_c \tau)^2} \right) \tag{6.1}$$

$$\sigma_{xy} = \frac{n_s e^2 \tau}{m^*} \left(\frac{\omega_c \tau}{1 + (\omega_c \tau)^2} \right) \tag{6.2}$$

Additionally, in contrast to the high field limit, weak steps are now seen in σ_{xy} which increases with increasing magnetic field. This subject was first theoretically studied by Khmelnitskii [30] based upon measurements of delocalised states in the integer quantum Hall effect and was experimentally observed for the spin-degenerate state by Hughes *et al.* [31].

Figure 6.15(a) shows ρ_{xx} and ρ_{xy} obtained as a function of magnetic field at $V_g = -0.260$ V. This experimental data clearly illustrates predictions of Khmelnitskii [30] once converted to σ_{xx} and σ_{xy} [Figure 6.15(b)]. Ideally, with no disorder and at zero temperature, the Hall conductivity would show a sharp step from $\sigma_{xy} = 0$ at low magnetic fields to $\sigma_{xy} = 2e^2/h$ (at $\nu = 2$) before falling back to zero at high fields. With disorder and finite temperature the data clearly shows the low and strong field limits discussed previously. Prior to $\nu = 2$ the Hall conductance increases whilst σ_{xy} shows weak oscillations. At fields greater than $\nu = 2$ σ_{xy} decreases in steps with associated σ_{xx} maxima.

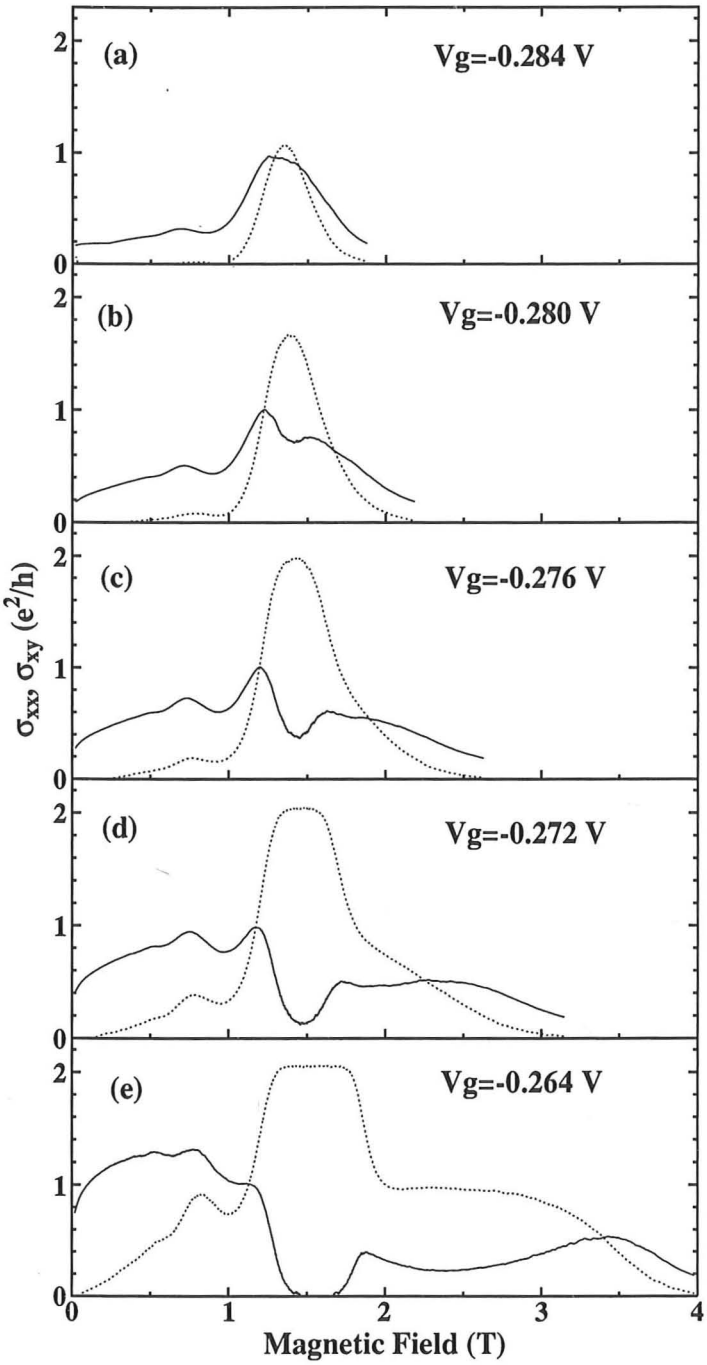

Figure 6.16: σ_{xx} (solid lines) and σ_{xy} (dotted lines) as function of magnetic field for various gate voltages at 20 mK. The conductivities σ_{xx} and σ_{xy} are calculated from the resistivity ρ_{xx} and ρ_{xy} via the matrix relation.

In figure 6.16 we plot the magnetic field dependence of σ_{xx} (solid lines) and σ_{xy} (dotted lines) for a range of negative gate bias at 20 mK. At the most negative bias, $V_g = -0.284$ V [figure 6.16(a)] the peaks in σ_{xx} have almost merged into a single feature. At $V_g = -0.280$ V [figure 6.16(b)] and $V_g = -0.276$ V [figure 6.16(c)], σ_{xx} has split into two peaks, the minimum between corresponding to the $\nu = 2$ spin-degenerate quantum Hall state. By $V_g = -0.272$ V [figure 6.16(d)] one begins to see the development in σ_{xx} at higher magnetic fields of the spin-polarised $\nu = 1$ state whilst σ_{xy} has a well quantised plateau $2e^2/h$ at $\nu = 2$. At a bias of $V_g = -0.264$ V [figure 6.16(e)] we observe the maxima (delocalised states) in σ_{xx} and strong quantised plateaus at $2e^2/h$ and e^2/h in σ_{xy}.

6.4.3 Experimental phase diagram

The results of the experimental observations described in sections 6.4.1 and 6.4.2 are used to determine the two phase diagrams in figure 6.17. Each phase diagram plots the gate voltage as a function of magnetic field for sample C1335c. Transition points on the phase boundaries in figure 6.17(a) were obtained from the temperature independent points in the ρ_{xx} data. As may be seen, all of the states are insulating at zero field. The second phase diagram utilises the fact that the peaks in σ_{xx} are a signature for the delocalised states [32, 33]. Figure 6.17(b) shows the phase diagram which derived from the conductance peaks in σ_{xx} at 20 mK. The exception being the closed triangle data points which were obtained at a temperature of 1.2 K.

Fogler and Shklovskii [34] have recently proposed that the collapse of spin splitting in the quantum Hall effect is due to the disorder induced broadening of Landau levels. This collapse is analogous to a ferromagnetic/paramagnetic transition. They have also suggested that disorder and the exchange energy [figure 6.18(a)] correspond to temperature and mag-

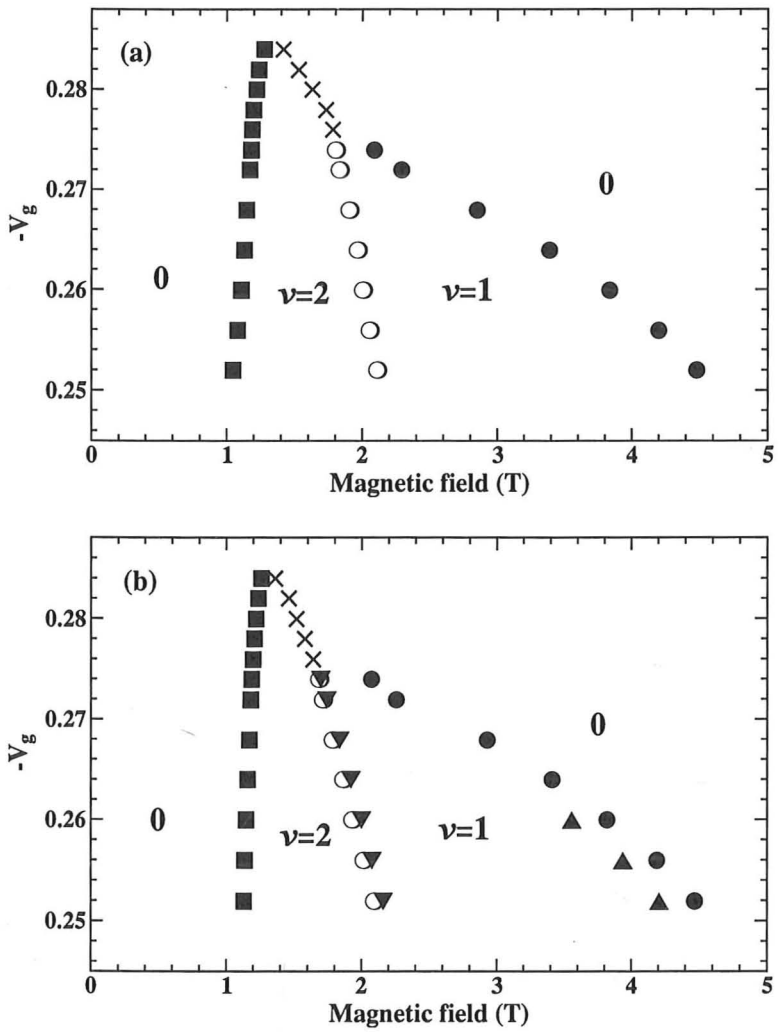

Figure 6.17: The phase diagram determined from (a) temperature independent points in ρ_{xx} traces and (b) peaks in σ_{xx}. Symbols indicate transitions from (i) $0-2$ (solid squares), (ii) $2-0$ (crosses), (iii) $2-1$ (open circles), (iv) $1-0$ (solid circles), and (v) peaks in σ_{xx} at 1.2 K (solid triangles).

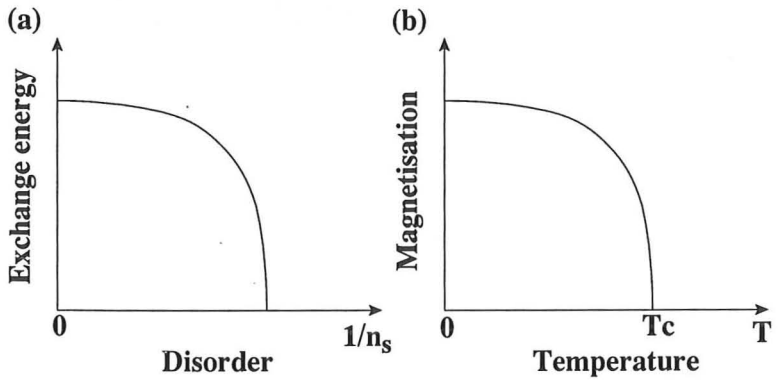

Figure 6.18: (a) Exchange energy as a function of disorder. (b) Ferromagnetic behaviour below critical temperature T_c.

netisation [figure 6.18(b)], respectively. Figure 6.17(b) shows the disorder induced collapse of spin splitting as well as temperature induced transition from ferromagnetic to paramagnetic state (solid triangles).

The similarity of figures 6.17(a) and (b) show that the phase boundary can be identified either by analysing the temperature independent points in ρ_{xx}, or from the peaks in σ_{xx} at low temperatures (< 300 mK).

6.5 Conclusions

In summary, we have studied the effect of sublimation on the size and density of inserted InAs dots. The dot distributions are strongly dependent upon the thickness of the GaAs capping layer grown on top the InAs dots. Due to variations in growth across the wafer the density of InAs dots in the central part of the wafer is approximately twice that at the wafer edge. We also observe that the mobility increases with the InAs dot density, and therefore the disorder, decreases. The disorder caused by the InAs dots resulted in different quantum life-times across the wafer surface and the life-time was found to be dependent upon the surface orientation. The preferential assembly of InAs dots along step edges in the $[01\bar{1}]$ direction is suggested as

the possible cause of the mobility anisotropy.

The effects of disorder for these self-assembled InAs quantum dots is similar to that observed in random InAs fluctuations, as observed in chapter 5. We mapped the experimental phase diagram using two methods, firstly the temperature independent ρ_{xx} points and secondly the maxima in σ_{xx}.

Bibliography

[1] J.-Y. Marzin, J.-M. Gérard, A. Izraël, and D. Barrier, Phys. Rev. Lett. **73**, 716 (1994).

[2] H. Drexler, D. Leonard, W. Hansen, J. P. Kotthaus, and P. M. Petroff, Phys. Rev. Lett. **73**, 2252 (1994).

[3] H. Sakaki, G. Yusa, T. Someya, Y. Ohno, T. Noda, H. Akiyama, Y. Kadoya, and H. Noge, Appl. Phys. Lett. **67**, 3444 (1995).

[4] K. Imamura, Y. Sugiyama, Y. Nakata, S. Muto, and N. Yokoyama, Jpn. J. Appl. Phys. **34**, L1445 (1995).

[5] S. Fafard, K. Hinzer, S. Raymond, M. Dion, J. McCaffrey, Y. Feng, and S. Charbonneau, Science, **274**, 1350 (1996).

[6] F. Heinrichsdor, M.-H. Mao, N. Kirstaedter, A. Krost, D. Bimberg, A. O. Kosogov, and P. Werner, Appl. Phys. Lett. **71**, 22 (1997).

[7] K. Yano, T. Ishii, T. Kobayashi, F. Murai, and K. Seki, IEEE Trans. El ectron Devices, **41**, 1628 (1994).

[8] P. M. Petroff, A. C. Gossard and W. Wiegmann, Appl. Phys. Lett. **45**, 620 (1984).

[9] M. Tanaka and H. Sakaki, Appl. Phys. Lett. **54**, 1326 (1989).

[10] R. Nötzel, J. Temmyo, and T. Tamamura, Appl. Phys. Lett. **64**, 3557 (1994).

[11] T. Noda, M. R. Fahy, T. Matsusue, B. A. Joyce, and H. Sakaki, Journal of Crystal Growth **127**, 783 (1993).

[12] D. Leonard, K. Pond, and P. M. Petroff, Phys. Rev. B **50**, 11687 (1994).

[13] M. Grundmann, O. Stier, and D. Bimberg, Phys. Rev. B **52**, 11969 (1995).

[14] D. Leonard, M. Krishnamurthy, C. M. Reaves, S. P. Den-Baars, and P. M. Petroff, Appl. Phys. Lett. **63**, 3203 (1993).

[15] H. Yamaguchi and Y. Horikoshi, Phys. Rev. B **51**, 9836 (1995).

[16] S. Guha, A. Maduhkar, and K. C. Rajkumar, Appl. Phys. Lett. **57**, 2110 (1990).

[17] D. Leonard, M. Krishnamurthy, S. Fafard, J. L. Merz, and P. M. Petroff, J. Vac. Sci. Technol. **B12**, 1063 (1994).

[18] N. P. Kobayashi, T. R. Ramachandran, P. Chen, and A. Madhukar, Appl. Phys. Lett. **68**, 3299 (1996).

[19] M. F. Ashby, and L. M. Brown, Phil. Mag. **8**, 1083 (1963).

[20] S. J. Brown, University of Cambridge, Ph.D. Thesis (1997).

[21] G. D. Lian. J. Yuan, L. M. Brown, G. H. Kim, and D. A. Ritchie, (unpublished)

[22] P. B. Hirsch, A. Howie, R. B. Nicholson, D. W. Pashley, and M. J. Whelan, *Electron Microscopy of Thin Crystals,* (p328 Krieger, Malabar, FL) (1977).

[23] G. R. Woolhouse and L. M. Brown, 4th Eur.Regional Conference on E. M., Rome 297 (1968).

[24] Q. Xie, P. Chen, and A. Madhukar, Appl. Phys. Lett. **65**, 2051 (1994).

[25] O. Brandt, K. Ploog, L. Tapfer, M. Hohenstein, R. Bierwolf, and F. Phillipp, Phys. Rev. B **45**, 8543 (1992).

[26] A. C. Churchill, G. H. Kim, A. Kurobe, M. Y. Simmons, D. A. Ritchie, M. Pepper, and G. A. C. Jones, J. Phys.: Condens. Matter **6**, 6131 (1994).

[27] F. F. Fang, A. B. Fowler, and A. Hartstein, Phys. Rev. B **16**, 4446 (1977).

[28] F. Stern and W. E. Howard, Phys. Rev. **163**, 816 (1967).

[29] T. Ando, A. B. Fowler, and F. Stern, Rev. Mod. Phys. **54**, 437 (1982).

[30] D. E. Khmelnitskii, Phys. Lett. **106A**, 182 (1984).

[31] R. J. F. Hughes, J. T. Nicholls, J. E. F. Frost, E. H. Linfield, M. Pepper, C. J. B. Ford, D. A. Ritchie, G. A. C. Jones, Eugene Kogan, and Moshe Kaveh, J. Phys.: Condens. Matt. **6**, 4763 (1994).

[32] I. Glozman, C. E. Johnson, H. W. Jiang, Phys. Rev. Lett. **74** 594 (1995).

[33] S. V. Kravchenko, W. Mason, J. E. Furneaux, and V. M. Pudalov, Phys. Rev. Lett. **75** 910 (1995).

[34] M. M. Fogler and B. I. Shklovskii, Phys. Rev. B **52**, 17366 (1995).

Chapter 7

Conclusions and Further Work

7.1 Conclusions

This thesis has described a number of experiments investigating the properties of n-type GaAs – $Al_xGa_{1-x}As$ heterojunctions grown on (311)B GaAs substrates and GaAs quantum wells with InAs self-assembled quantum dots or dashes. The former provides information upon the mobility anisotropy of the (311)B surface whilst the latter enables an investigation of the insulator-quantum Hall liquid transition with low temperatures and applied magnetic fields.

The characteristics of high mobility 2DEGs grown on (311)B GaAs substrates were detailed in chapter four using data from magnetoresistance experiments. The transport to quantum life-time ratio in this system was found to vary between 10 and 70, these values being typical of a high quality 2DEG with mobility limited by remote ionized impurity scattering. The observation of an anisotropic mobility in the $[\bar{2}33]$ and $[01\bar{1}]$ orientations is due to surface corrugation of (311)B substrate in the GaAs-AlGaAs heterojunction. Although an anisotropic scattering was found at zero magnetic field,

the effective mass was shown to be isotropic using focusing experiments. In addition, the electron ballistic length was found to be between 2.2 and 2.5 μm. This length is between the mean free path and the length scale derived from the quantum life-time.

In chapters five and six, samples with InAs monolayers inserted into a GaAs well were characterised by UHVSTM, AFM, TEM, and STEM. The density of InAs self-assembled quantum dots for samples with 2.15 MLs InAs was shown to be determined by a sublimation model. The InAs dots disappeared at growth temperatures above 580°C and their distribution was strongly dependent on the GaAs coverage over the InAs dots. For a GaAs coverage d_c = 10 Å, InAs dashes were formed rather than dots and some InAs interdiffused into the GaAs. The InAs self-assembled dot density for GaAs capping layers with d_c = 100 Å was about twice that with d_c = 50 Å. The average InAs dot size also changed with d_c and was $\sim$ 360 Å in width and 80 Å in height for GaAs capping layers of d_c = 100 Å and $\sim$ 280 Å in width and 40 Å in height for GaAs capping layers of d_c = 50 Å.

When a reference sample with no InAs inserted was studied, the ratio of the transport to quantum life-time was found to be $\sim$ 16. This value is typical for a remotely doped GaAs-AlGaAs hetrostructure with mobility limited by long-range remote ionised impurity scattering. However, for samples with InAs dots or dashes in the GaAs well, the ratio was found to be $\sim$ 5, typical of short-range scattering. The transport properties of those samples with InAs dots or dashes are between typical parameters for high mobility GaAs-AlGaAs heterostructures and Si MOSFETs.

We have investigated magnetically induced insulator-quantum Hall liquid transitions in devices with InAs monolayers inserted in the centre of the GaAs quantum well. Three different types of transitions were observed: (i) $0 \rightarrow 2 \rightarrow 0$, This transition was observed in the GaAs 2DEG system, see references [1, 2, 3, 4]. (ii) $0 \rightarrow 1 \rightarrow 0$, This transition was observed in a

high mobility GaAs 2DEG system in reference [5] and in Ge/SiGe quantum wells with two dimensional-hole gases [6]. (iii) $0 \rightarrow 2 \rightarrow 0 \rightarrow 1 \rightarrow 0$, Similar transitions, referred to as the camel back structure, were observed in high mobility Si MOSFETs [7]. We were also able to observe the transition $0 \rightarrow 2 \rightarrow 1 \rightarrow 0$ together with each of the three transitions listed above. The major result of this thesis is the determination of the experimental phase diagram, including the spin-polarised Landau filling factor $\nu = 1$, in which the collapse of spin splitting in the quantum Hall effect was observed. The collapse of the spin-splitting is a result of the collapse of the exchange energy gap through disorder [8]. This behaviour is similar to the ferromagnetic transition with temperatures.

7.2 Further work

It has been generally believed that the transition between localised and delocalised states in the integer quantum Hall effect should be observable as a decrease in the localisation length ξ determined from the longitudinal resistance ρ_{xx} as a function of temperature and applied magnetic field strength. These transitions have attracted considerable interest both experimentally [9, 10, 3] and theoretically [11, 12, 13, 14, 15]. The localisation length in a Landau level near to the Fermi energy should diverge like a power law in magnetic fields $\xi = \xi_0 \mid B - B^* \mid^{-\nu}$, where B^* is the singular point (from the temperature independent fields in the ρ_{xx} data) and ν is a localisation critical exponent. This exponent ν can be found directly from the magnetic field induced transitions from an insulating state to quantum Hall liquid state through the ρ_{xx} traces. The localisation length can also be considered as simple activation [16], Coulomb gap induced $T^{1/2}$ variable-range hopping [17, 18], or Mott's $T^{1/3}$ variable-range hopping [19, 15]. The value of ν can also be determined through scaling theory which shows that the maximum in $d\rho_{xy}/dB$ between two adjacent quantum Hall plateaus diverges as

a power law in temperature $(\partial\rho_{xy}/\partial B)_{max} \propto T^{-\mu}$ [9,10, 20], where μ is a single critical exponent. The μ is related to the localisation critical exponent ν through the relation $\mu = p/2\nu$, where p is the temperature exponent of the inelastic scattering rate (i.e. $1/\tau_i \sim T^p$) and is an unknown value. The samples containing InAs monolayers in the GaAs well would be suitable for investigating the localisation length scale and the inelastic scattering exponent p could then be calculated directly from both the localisation critical exponent ν and the single critical exponent μ.

Bibliography

[1] H. W. Jiang, C. E. Johnson, K. L. Wang, and S. T. Hannahs, Phys. Rev. Lett. **71**, 1439 (1993).

[2] T. Wang, K. P. Clark, G. F. Spencer, A. M. Mack, and W. P. Kirk, Phys. Rev. Lett. **72**, 709 (1994).

[3] R. J. F. Hughes, J. T. Nicholls, J. E. F. Frost, E. H. Linfield, M. Pepper, C. J. B. Ford, D. A. Ritchie, G. A. C. Jones, Eugene Kogan, and Moshe Kaveh, J. Phys.: Condens. Matt. **6**, 4763 (1994).

[4] I. Glozman, C. E. Johnson, H. W. Jiang, Phys. Rev. Lett. **74**, 594 (1995).

[5] D. Shahar, D. C. Tsui, and J. E. Cunningham, Phys. Rev. B **52**, R14372 (1995).

[6] H. Hilke, D. Shahar, S. H. Song, D. C. Tsui, Y. H. Xie, and D. Monroe, Phys. Rev. B **56**, 15545 (1997).

[7] S. V. Kravchenko, W. Mason, J. E. Furneaux, and V. M. Pudalov, Phys. Rev. Lett. **75**, 910 (1995).

[8] M. M. Fogler and B. I. Shklovskii, Phys. Rev. B **52**, 17366 (1995).

[9] H. P. Wei, D. C. Tsui, M. A. Paalanen, and A. M. M. Pruisken, Phys. Rev. Lett. **61**, 1294 (1988).

[10] S. Koch, R. J. Haug, K. v. Klitzing, and K. Ploog, Phys. Rev. Lett. **67**, 883 (1991).

[11] A. M. M. Pruisken, Phys. Rev. Lett. **61**, 1297 (1988).

[12] B. Huckestein and B. Kramer, Phys. Rev. Lett. **64**, 1437 (1990).

[13] T. Ando and H. Aoki, J. Phys. Soc. Jpn. **54**, 2238 (1985).

[14] H. L. Zhao and S. Feng, Phys. Rev. Lett. **70**, 4134 (1993).

[15] D. Lee, Z. Wang and S. Kivelson, Phys. Rev. Lett. **70**, 4130 (1993).

[16] M. Pepper, Phil. Mag. B **37**, 83 (1978).

[17] A. Briggs, Y. Guldner, J. P. Vieren, M. Voos, J. P. Hirtz, and M. Razeghi, Phys. Rev. B **27**, 6549 (1983).

[18] D. G. Polyakov and B. I. Shklovskii, Phys. Rev. Lett. **70**, 3796 (1993).

[19] D. C. Tsui, H. L. Stormer, and A. C. Gossard, Phys. Rev. B **25**, 1405 (1982).

[20] S. W. Hwang, H. P. Wei, L. W. Engel, and D. C. Tsui, Phys. Rev. B **48**, 11416 (1993).

Appendix A

Mathematical expressions used in the calculation of the mobility of a 2DEG on a (311) surface

The scattering processes considered in the following are remote ionised impurity and anisotropic interface roughness scattering. Fang-Howard wavefunctions are assumed at $T = 0$ K [1] and the relaxation time approximation is used. The mobility in the x-direction, for example, is given by

$$\mu_x = \frac{|e|}{m^*}\tau_x^{total}, \tag{A.1}$$

$$\frac{1}{\tau_x^{total}} = \frac{1}{\tau_{remote}} + \frac{1}{\tau_{IR,x}}, \tag{A.2}$$

where the first term in the right hand side of equation A.2 is the scattering rate due to the remote ionised impurities and the second is due to the

interface roughness scattering. The scattering times are calculated in the following.

A.1 Fang-Howard wavefunction

The Fang-Howard wavefunction is written as [2],

$$f(z) = \left(\frac{1}{2}b^3\right)^{1/2} z\left(-\frac{1}{2}bz\right), \tag{A.3}$$

$$b = \left(\frac{12m^*e^2}{\kappa_0\varepsilon_0\hbar^2}\right)^{1/3}\left(N_{depl} + \frac{11}{32}N_s\right)^{1/3}, \tag{A.4}$$

where the hetero-interface is taken as the origin of the z-axis (direction normal to 2DEG). Then the form factor can be calculated analytically,

$$F(q) = \int dz \int dz' \mid f(z) \mid^2 \mid f(z') \mid^2 \exp(-q \mid z - z' \mid) \tag{A.5}$$

$$= \frac{b(8b^2 + 9bq + 3q^2)}{8(b+q)^3} \tag{A.6}$$

If an impurity is located away from the wavefunction, such that there is no spatial overlap between the impurity and wavefunction, the impurity form factor is given analytically, using the Fang-Howard wavefunction as,

$$\int F(q, z_{imp}) = \int dz \mid f(z) \mid^2 \exp(-q \mid z_{imp} - z \mid) \tag{A.7}$$

$$= \int_0^\infty dz \mid f(z) \mid^2 \exp\left[-q(z - z_{imp})\right]$$

$$= \frac{b^3}{(b+q)^3}\exp(qz_{imp}) \tag{A.8}$$

A.2 Scattering due to remote ionised impurities

The life time due to remote ionized impurity scattering is given by,

$$\frac{1}{\tau_{remote}} = \frac{m^* e^4}{8\pi\hbar^3\kappa_0^2\varepsilon_0^2}\int_0^{2\pi} d\theta \int_{z_{min}}^{z_{max}} dz_{imp}\left[\frac{F(q,z_{imp})}{qS(q)}\right] N(z_{imp})(1-\cos\theta), \tag{A.9}$$

where
$$q = 2k_F\left|\sin\left(\frac{\theta}{2}\right)\right|, \tag{A.10}$$

$$S(q) = 1 + \frac{e^2}{2\kappa\varepsilon q}F(q)\Pi(q), \tag{A.11}$$

$$\Pi(q) = \frac{m^*}{\pi\hbar^2}. \tag{A.12}$$

Here q is the scattered wave-vector, $F(q)$ the form factor from equation A.5, $F(q, z_{imp})$ the impurity form factor from equation A.7, $N(z_{imp})$ the impurity distribution, $S(q)$ the screening function and $\Pi(q)$ the polarisation function.

When q, the scattered distribution, is uniform from z_{min} to z_{max}, and the origin of the z-axis is taken at the hetro-interface we can write that

$$\frac{1}{\tau_{remote}} = \frac{m^* e^4 N_{imp}}{8\pi\hbar^3\kappa_0^2\varepsilon_0^2}\times \int_0^{2\pi} d\theta\left(\frac{e^{2qz_{max}} - e^{2qz_{min}}}{2q}\right)\frac{b^6}{(b+q)^6}\frac{(1-\cos\theta)}{[qS(q)]^2}. \tag{A.13}$$

A.3 Scattering due to anisotropic interface roughness

We assume a Gaussian form of the correlations due to the anisotropic interface roughness such that

$$< \Delta(\vec{r})(\vec{r'}) >= \Delta^2 \exp\left[\frac{(x-x')^2}{\Lambda_x} - \frac{(y-y')^2}{\Lambda_y}\right], \tag{A.14}$$

where Δ is the average displacement from the interface and Λ_x and Λ_y are the typical sizes of the islands at the interface in the x- and y-directions respectively. The Fourier component of equation A.14 is

$$\begin{aligned}\langle|\Delta_{\vec{q}}|^2\rangle &= \int dq_x \exp\left(iq_x x - \frac{x^2}{\Lambda_x}\right) \int dq_y \exp\left(iq_y y - \frac{y^2}{\Lambda_y}\right) \\ &= \pi\Lambda_x\Lambda_y \exp\left(-\frac{q_x^2\Lambda_x^2}{4} - \frac{q_y^2\Lambda_y^2}{4}\right). \end{aligned} \tag{A.15}$$

Using equation A.15, the scattering rate, as given by Ando [2], is

$$W(\vec{q} = \vec{k} - \vec{k'}) = \frac{2\pi}{\hbar}\pi(\Delta^2\Lambda_x\Lambda_y)\left[\frac{F_{eff}}{S(q)}\right]^2 \exp\left(\frac{q_x^2\Lambda_x^2 + q_y^2\Lambda_y^2}{4}\right). \tag{A.16}$$

Here F_{eff} is the effective field,

$$F_{eff} = \int dz \mid f(z) \mid^2 \frac{\partial u(z)}{\partial z} = \frac{e^2}{\kappa_0\varepsilon_0}\left(\frac{N_s}{2} + N_{depl}\right). \tag{A.17}$$

The scattering time in the x-direction is then given by

$$\frac{1}{\tau_{IR,x}} = \frac{m^*}{2\pi\hbar^3}\times \int_0^{2\pi} d\theta_k \int_0^{2\pi} d\theta_{k'}(\Delta^2\Lambda_x\Lambda_y)\left[\frac{F_{eff}}{S(q)}\right] e^{-\frac{1}{4}(q_x^2\Lambda_x^2 + q_y^2\Lambda_y^2)}(\cos\theta_{\rm k} - \cos\theta_{\rm k'})\cos\theta_{\rm k}, \tag{A.18}$$

with

$$q_x = k(\cos\theta_{\rm k} - \cos\theta_{\rm k'}) \text{ and } q_y = k(\sin\theta_{\rm k} - \sin\theta_{\rm k'}), \tag{A.19}$$

where the angles θ_k and $\theta_{k'}$ are defined relative to the x-axis. Substituting equation A.17 into equation 18, gives

$$\frac{1}{\tau_{IR,x}} = \frac{m^* e^4}{2\pi\hbar^3\kappa_0\varepsilon_0}\left(\frac{N_s}{2} + N_{depl}\right)^2 \times \int_0^{2\pi} d\theta_k \int_0^{2\pi} d\theta_{k'} \frac{[\cos\theta_k - \cos\theta_{k'}]\cos\theta_k}{[S(q)]^2} \exp\left[-\frac{1}{4}(q_x^2\Lambda_x^2 + q_y^2\Lambda_y^2)\right]. \tag{A.20}$$

A.4 Scattering due to isotropic interface roughness

In the case of isotropic interface roughness scattering, equation A.20 simplifies to

$$\frac{1}{\tau_{IR,x}} = \frac{m^* e^4 (\Delta\Lambda)^2}{2\pi\hbar^3\kappa_0\varepsilon_0} \times \left(\frac{N_s}{2} + N_{depl}\right)^2 \pi \int_0^{2\pi} d\theta \frac{[1 - \cos\theta_{k'}]}{[S(q)]^2} \exp\left[-\frac{q^2\Lambda^2}{4}\right]. \tag{A.21}$$

A.5 Related quantities

The depletion charge (N_{depl}) on the channel side of a high electron mobility transistor (HEMT) structure is given by

$$N_{depl} = \sqrt{2\kappa_0\varepsilon_0 N_{AC} e\phi_d}, \tag{A.22}$$

where $e\phi_d$ is approximately the band gap of the channel material. The lowest subband in the heterojunction can be approximated by

$$E_0 = \left(\frac{3}{2}\right)^{5/3} \left(\frac{e^2\hbar}{\kappa_0\varepsilon_0\sqrt{m^*}}\right)^{2/3} \frac{N_{depl} + \frac{55}{96}N_s}{\left(N_{depl} + \frac{11}{32}N_s\right)^{1/3}}. \tag{A.23}$$

Some other quantities related to band bending in heterostructures were presented by Stern [3].

Bibliography

[1] B. R. Nag *Electron Transport in Compound Semiconductors,* (Springer Series in Solid State Sciences II) (Berlin: Springer), (1980).

[2] T. Ando, A. B. Fowler, and F. Stern, Rev. Mod. Phys. **54**, 437 (1982).

[3] F. Stern, Phys. Rev. Lett. **44**, 1469 (1980).

Appendix B

Interference effects at low magnetic fields

We have studied the anomalous negative magnetoresistance in both $[01\bar{1}]$ and $[\bar{2}33]$ directions as a function of temperature, and the results are summarized in figure B.1. We see that whilst the magnetoresistance in the $[01\bar{1}]$ direction persists up to 35 K, in the $[\bar{2}33]$ direction it is suppressed by 8 K. We also find the magnetoresistance has a B^2 dependence at fields below 0.1 T. A small negative magnetoresistance can be associated with the suppression of weak localization, however, at fields less than 50 mT, weak localization is normally observed in low mobility 2DEGs at low temperature where the elastic mean free path is large [1]. These conditions are not consistent with our observations as the 2DEG mobility is very high ($> 1 \times 10^6$ cm^2/Vs) and the negative magnetoresistance extends to fields above 0.1 T, and is observed at temperatures up to 35 K. The presence of a high field magnetoresistance has been seen in 2DEGs in the past and has been explained through electron-electron interactions [2, 3].

The latter cause, due to electron-electron interactions, may be investigated by considering the electron-electron interactions to give rise to a small perturbation on the conductivity tensor component σ_{xx}. This in turn gives

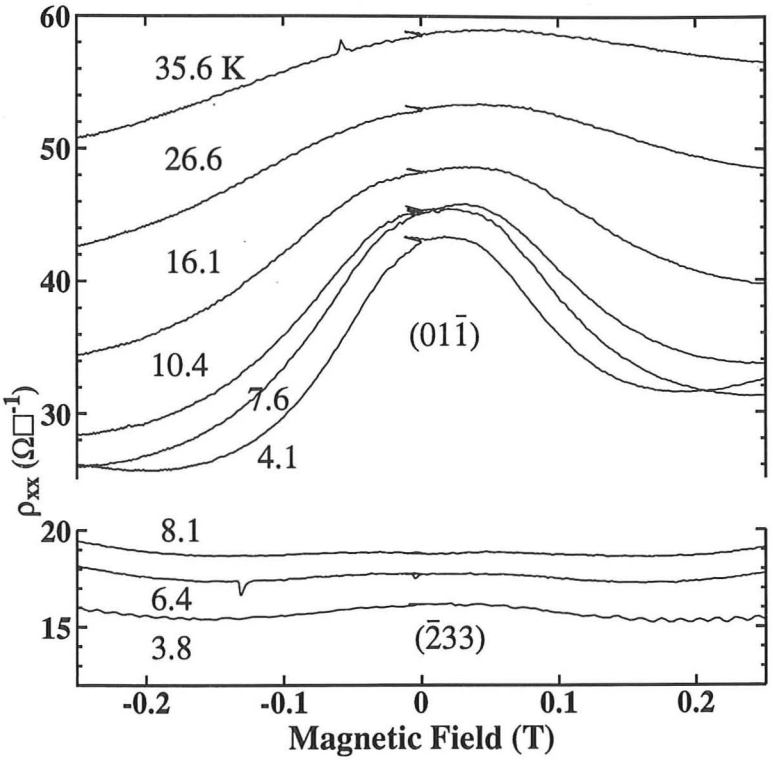

Figure B.1: The magnetoresistance observed as a function of temperature, between 4 and 35 K in both the [$\bar{2}$33] and [01$\bar{1}$] directions for sample T104.

rise to a parabolic perturbation in $\rho_{xx}(B)$. The exact form for small $\delta\sigma_{xx}$ with $\delta\sigma_{xx} = 0$ is given by:

$$\rho_{xx}(B) = \rho_{xx}(0) + \rho_{xx}(0)^2\delta\sigma_{xx} + \rho_{xx}(0)^2\mu^2B^2\delta\sigma_{xx} \tag{B.1}$$

Equation B.1 is derived from inverting the conductivity tensor with the perturbation to $\delta\sigma_{xx}$ included: We take $\mu B = \omega_c\tau_0$, where ω_c is the cyclotron frequency, τ_0 the transport scattering time and the relation $\rho_{xy} = \omega_c\tau_0\rho_{xx}$ is assumed. The B^2 dependence can be obtained as a function of temperature and direction by fitting a parabola to our results and applying equation B.1. Figure B.2 shows $\delta\sigma_{xx}$ as a function of temperature. It can be seen that for both directions $\delta\sigma_{xx}$ has a logarithmic dependence on temperature, $\delta\sigma_{xx} \propto \beta log(T)$. However, there is a difference in gradient, β

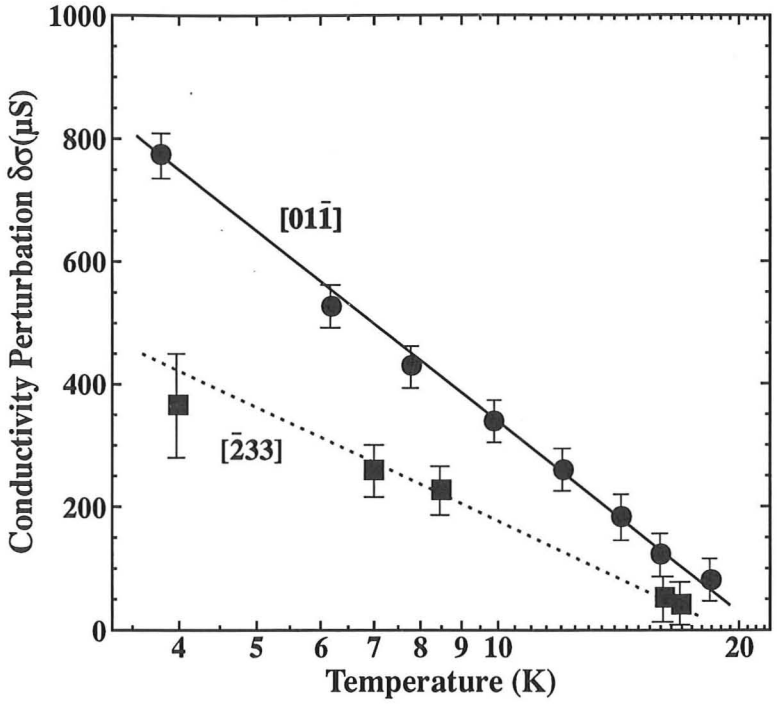

Figure B.2: The conductivity perturbation $\delta\sigma$ derived from the magnetoresistance as a function of temperature. Note that $\delta\sigma$ is proportional to $log(T)$ and that its magnitude depends on the direction of current flow.

depending on the direction. The magnitude of the electron-electron interaction is very small and it only causes a small perturbation on the resistivity. Our results show a very large magnetoresistance, which not only puts into question the validity of equation B.1 but suggests that it is unlikely that the observed magnetoresistance is due to electron-electron interactions. The magnetoresistance is more likely due to some kind of interference rather than an interaction effect. For example, Smith *et al.* [4] have reported a logarithmic dependence in conductivity perturbation for a one-dimensional superlattice imposed on a 2DEG. They explain this phenomenon as a form of localization caused by Bragg reflections within the superlattice, where electron half-wavelengths interfere to cause the magnetoresistance. It is possible that we observe a similar effect, and we might be seeing the manifestation

of a periodic interface roughness imposing a superlattice potential on the 2DEG.

Bibliography

[1] R. Gao, C. de Graaf, A. S. Shussler, S. Radelaar, and K. Heyers, Phys. Rev. B **46**, 9885 (1993).

[2] M. A. Paalanen, D. C. Tsui, and J. C. M. Hwang, Phys. Rev. Lett. **51**, 2226 (1983).

[3] B. L. Al'tshuler and G. Aronov, *Electron-electron Interactions in Disordered Systems,* Paalanen, ed A. L. Efros and M. Pollak (Amsterdam: North-Holland) (1985).

[4] C. G. Smith, M. Pepper, R. Newbury, H. Ahmed, D. G. Hasko, D. C. Peacock. J. E. F. Frost, D. A. Ritchie and G. A. C. Jones, J. Phy. Condens. Matter **2**, 3405 (1990).